ADVANCED MATERIALS AND CONCEPTS FOR ENERGY STORAGE DEVICES

by

Shiang Jen Teng

A dissertation submitted to the faculty of
The University of Utah
in partial fulfillment of the requirements for the degree of

Doctor of Philosophy

Department of Materials Science and Engineering

The University of Utah

December 2014

The University of Utah Graduate School

STATEMENT OF DISSERTATION APPROVAL

The dissertation of **Shiang Jen Teng**

has been approved by the following supervisory committee members:

Ashutosh Tiwari	, Chair	**09/17/2014** Date Approved
Reaz Chaudhuri	, Member	**09/17/2014** Date Approved
Ling Zang	, Member	**09/17/2014** Date Approved
Taylor Sparks	, Member	**09/17/2014** Date Approved
Berardi Sensale Rodriguez	, Member	**09/17/2014** Date Approved

and by **Feng Liu** , Chair/Dean of

the Department/College/School of **Materials Science and Engineering**

and by David B. Kieda, Dean of The Graduate School.

ABSTRACT

Over the last decade, technological progress and advances in the miniaturization of electronic devices have increased demands for light-weight, high-efficiency, and carbon-free energy storage devices. These energy storage devices are expected to play important roles in automobiles, the military, power plants, and consumer electronics. Two main types of electrical energy storage systems studied in this research are Li ion batteries and supercapacitors. Several promising solid state electrolytes and supercapacitor electrode materials are investigated in this research.

The first section of this dissertation is focused on the novel results on pulsed laser annealing of $Li_7La_3Zr_2O_{12}$ (LLZO). LLZO powders with a tetragonal structure were prepared by a sol-gel technique, then a pulsed laser annealing process was employed to convert the tetragonal powders to cubic LLZO without any loss of lithium.

The second section of the dissertation reports on how $Li_5La_3Nb_2O_{12}$ (LLNO) was successfully synthesized via a novel molten salt synthesis (MSS) method at the relatively low temperature of 900°C. The low sintering temperature prevented the loss of lithium that commonly occurs during synthesis using conventional solid state or wet chemical reactions.

The second type of energy storage device studied is supercapacitors. Currently, research on supercapacitors is focused on increasing their energy densities and lowering their overall production costs by finding suitable electrode materials. The third section

of this dissertation details how carbonized woods electrodes were used as supercapacitor electrode materials. A high energy density of 45.6 Wh/kg and a high power density of 2000 W/kg were obtained from the supercapacitor made from carbonized wood electrodes. The high performance of the supercapacitor was discovered to originate from the hierarchical porous structures of the carbonized wood.

Finally, the fourth section of this dissertation is on the electrochemical effects of embedding Cu nanoparticles into a carbonized wood supercapacitor. The nano-composites were fabricated using a solution method. The electrochemical measurements indicated that Cu nanoparticles did enhance the energy density of the supercapacitor by a factor of three. Both cyclic voltammetry and cyclic charge-discharge measurements showed that the electrode has typical reversible pseudocapacitive behavior, with two pairs of redox reaction peaks.

TABLE OF CONTENTS

LIST OF TABLES

LIST OF ABBREVIATIONS

LIBs	Lithium-ion batteries
LLZO	$Li_7La_3Zr_2O_{12}$
LLNO	$Li_7La_3Nb_2O_{12}$
PLD	Pulsed laser deposition
SEM	Scanning electron microscope
EDS	Energy dispersive x-ray spectroscopy
XRD	X-ray diffraction
XPS	X-ray photoelectron spectroscopy
EIS	Electrochemical impedance spectroscopy
SSE	Solid state electrolyte
ECs	Electrochemical capacitors
HVs	Hybrid vehicles
EVs	Electric vehicles

ACKNOWLEDGEMENTS

I would like to thank my advisor, Professor Ashutosh Tiwari, for guidance, support and the special opportunity to work with him in the Nanostructured Materials Research Laboratory. I would also like to thank my committee for their input and assistance.

I would like to especially thank my wife for supporting my study and life during the time of pursuing a degree.

CHAPTER 1

INTRODUCTION

1.1 Overview

The depletion of fossil fuels has shifted electricity production from burning fuels to sustainable energy sources. Most sustainable energy sources do not produce energy at a constant rate, but instead, the energy produced depends on the periodic characteristics of the energy source, such as sun, tide, and wind. It is common for these energy sources to be used together with electrochemical energy storage devices. The sustainable energy sources provide energy to the electrochemical energy storage devices when they are in operation. The electrochemical energy storage devices supply power when the sustainable energy sources are not in operation. Regardless of type of sustainable energy, electrochemical energy storage devices are always needed to provide power when the source of the sustainable energy is not in operation.

Electrochemical energy storage systems are used in many applications and are characterized by their specific energy and specific power, as seen in Figure 1.1. In general, batteries rely on chemical reactions with valence band electron transfer, which gives batteries high specific energy. On the other hand, electrochemical capacitors (ECs) have ion adsorption on the surface with electron transfer in the conduction band. The process is relative easy and gives ECs high specific power. This fundamental

difference between ECs and batteries has determined their many applications.

One of the most important applications for electrochemical energy storage devices are hybrid vehicles (HVs) and electric vehicles (EVs). Table 1.1 lists the specific operation conditions for HVs and EVs [1]. The HVs contain both a combustion engine and an electrical motor. At higher speeds, the combustion engine provides the driving force of the car. During slow speed driving, the car is powered by a stack of batteries. The batteries are charged when a driver taps on brakes, as the car's mechanical energy is converted to electrical energy and then feeds back to its batteries. For hybrid vehicles, low energy density Ni metal hydride (Ni-MH) batteries can be used whose main advantages are a long cycle life and excellent safety features [1]. However, much more energy is required to power EVs. Li ion batteries with high energy and low self-discharge are the best candidates for EVs. ECs also play an important role in HVs and EVs. The ECs are charged during braking through the electric motor. Once the driver steps on the acceleration peddle, ECs suddenly deliver their energy and propel the car forward.

1.2 Li ion batteries

Batteries have been used as the primary electricity storage source for over a century. Nickel-based batteries were the only battery for electronics for many years until the commercialization of the Li ion battery. Introduced in 1991 by Sony, the first Li ion battery was fabricated with a $LiCoO_2$ cathode. $LiCoO_2$ has good electrical properties, good safety properties, and is easy to prepare. More recently, lower cost, higher performance materials such as $LiMn_2O_4$ and $LiNiCoO_2$ have been used to improve performance [2]. A schematic illustration of a Li ion battery cell is shown in Figure 1.2.

Graphite is the most commonly used anode material for Li ion batteries because of its laminate structure which is ideal for storing Li ions. The general operational principle of Li ion batteries during charging is: the Li ions in electrolyte are reduced and intercalated into anode while the Li stored in cathode is oxidized and released into electrolyte. The following equations correspond to the reactions for anode and cathode upon charging.

Anode reduction reaction

$$xLi^+ + 6C + xe^- \leftrightarrow Li_xC_6$$

Cathode oxidation reaction

$$LiCo_2O_2 \leftrightarrow xe^- + Li_{(1-x)}Co_2O_2 + xLi^+$$

The major advantages and disadvantages of Li ion batteries compared to other types of batteries are summarized in Table 1.2. The high single cell voltage of 2.5V~4.2V, which is about three times higher than that of NiCd and Ni-MH cells, enables Li ion batteries to store more energy. The high specific energy density and high power density of Li ion batteries make them suitable for light-weight and high-efficiency applications. One of the disadvantages of Li ion batteries is that they usually require a management circuit to protect the cells from overcharging and overheating. Another disadvantage of Li ion batteries is that they lose capacity at elevated temperature around 65^{o}C [3]. Many researches have been focused on finding new materials for anode, cathode, and electrolyte to overcome these problems.

1.2.1 Anode materials

Although Li ion batteries have a relatively high energy density, there is interest in further increasing their energy density by using new anode materials with high operational potentials. The highest voltage of 4 V is obtained when elemental Li anode

is used. In principle, the ideal anode material is elemental Li; however in practice, it has been reported that elemental Li anode has high reactivity with an organic electrolyte solvent, and thus forms dendrites on the anode surface [4]. The dendrite growth on the Li anode can result in short circuit and ignition. Many efforts have been made to find an alternative anode material with good chemical stability. The main requirements for good anode materials are summarized as follows:

- High specific capacitance (mAh/g or mAh/cm^3)
- Long cycle life with no irreversible structure changes
- Chemical and thermal stability with the electrolyte
- None toxic

Two major categories of anode materials have attracted much attention; one is lithiated carbons and the other is Li alloy systems. The first type of attractive anode material for Li ion battery is lithiated carbons. Carbons are good candidates for anode materials due to their diverse structures and properties. Many types of carbon-based materials, from crystalline to highly disordered, have been researched as the anode materials for Li ion batteries [5, 6]. Currently, graphite is the most common anode material used because of its good cycle ability. Graphite is a stack of carbon sheet that is formed by hexagonally bonded carbons through van der Waal forces, as seen in Figure 1.3. The process of Li ion inserted in between the graphite is known as intercalation. The specific capacitance of the graphite anode is 372 mAh/g [7]. However, the rapid growing demand for higher capacity and higher power Li ion batteries have motivated research on new materials other than graphene for Li ion battery anode.

The second type of attractive anode material for the Li ion battery is Li alloys. The advantages of using Li alloys as anode material are their high specific capacitance and safety characteristics. Table 1.3 compares the electrical properties of Li alloy anodes. The alloy anodes have 2-20 times higher theoretical specific capacitance than that of graphene [8]. The Li storage mechanism for graphene and alloy anodes is different. The graphene stores the Li through intercalation while the Li alloys can store far more Li by forming alloys. However, one of the disadvantages of using Li alloy anode is the reduction of the specific capacitance [4]. The additional species in the compound do not undergo any electrochemical reaction and bring additional weight to the anode. The extra weight in the anode reduces the specific energy density significantly compared to the pure Li anode. In addition, many studies found that many alloy anodes have high initial capacitance loss and rapid capacity dissipation [9, 10]. The cause of large capacity loss for alloyed anodes is due to the large volume change and loss of active material during the charge-discharge process [10].

1.2.2 Cathode materials

One of the most important characters of high power Li ion batteries is high charge-discharge rate. The charge-discharge rate depends on the ease of the Li ion diffusion through the cathode. The higher the diffusivity of the material, the faster the charge-discharge rate of the battery can be. The crystal structure of cathode material has a direct impact on the Li ion diffusion, as seen in Table 1.4 [4]. The 2D layered structure $LiCoO_2$ exhibits the highest Li ion diffusivity and the 1D unidirectional $LiFePO_4$ tunnel has the lowest diffusivity [4]. In the case of $LiCoO_2$, the Co atoms reside within O octahedra and Li atoms reside in the space between the oxygen layers. The Li

intercalation is much more facile in the $LiCoO_2$ layered structure than trying to diffuse into interstitial sites in $LiFePO_4$.

The most common ways to manipulate the diffusivity of cathode are through doping and reducing the particle size. The dopant in the cathode materials changes the lattice parameters of the crystal to either increase or decrease the ease of Li ion diffusion. Some doped cathode materials and their properties are listed in Table 1.5 [3, 12]. The effect of dopant on the cathode materials is not significant and the process is difficult to control.

The most effective way to increase the ion diffusivity is to reduce the particle size to the nano scale region, in order to significantly reduce the Li ion diffusion length [13, 14]. However, the surface energy of nanoparticles increases dramatically when the particle size is reduced. The high surface energy allows cathode materials to form a solid electrolyte interface (SEI) layer that serves as a barrier for Li ion diffusion [14]. Unfortunately, none of the methods mentioned above has led to a breakthrough in cathode material selection. More research and experiment are needed to validate these methods.

1.2.3 Electrolyte materials

The principle limitation of Li ion batteries is the voltage limitation of the cell. Traditional batteries use aqueous electrolytes such as H_2SO_4 and KOH and have a potential window of V_{oc}=1.23V [3]. However in Li ion batteries, Li has a higher electropositive than hydrogen which allows the battery to operate at higher voltage. In order to reach the highest voltage possible in a Li ion battery, a nonaqueous electrolyte (such as organic liquid) with a larger V_{oc} window is required. A wide variety of non-

aqueous electrolytes including organic solvents and solid state electrolytes have been examined for Li ion batteries.

1.2.3.1 Organic liquid electrolytes

Many organic solvents that can dissolve Li salts have been examined as electrolyte materials for Li ion batteries. The material selection criteria for organic electrolyte in Li ion batteries are listed below:

- The solvent should be aprotic at fairly negative potential (i.e., does not react with Li metal)
- The solvent should have high polarity in order to dissolve Li salts
- The solvent should have low melting temperature and high boiling temperature
- The solvent should have high relative permittivity and low viscosity

It is very difficult to satisfy all the above conditions, since most of the requirements are contradictory to one another in principle. However, organic electrolytes with high mobility and a high degree of dissociation are preferred. Some examples of the non-aqueous electrolytes for Li ion batteries are listed in Table 1.6 [4]. In general, the ionic conductivity of organic electrolytes is in a range of $2x10^{-1}$ S/cm.

Many organic electrolytes have been used in Li ion batteries. No practical electrolyte is chemically stable with Li during charge-discharge cycling. Many electrolytes form a passive SEI layer to separate the electrolyte from the electrode. When a SEI is form, Li is incorporated in the passivation film. This process is irreversible and is observed as a loss of capacity [12]. In addition to the SEI formation, most of the organic electrolytes have been proved to be unsafe when the cell is

overcharged or overheated. These safety concerns have motivated the research on solid state electrolyte.

1.2.3.2 Sold state electrolytes

Solid state Li ion conductors have garnered interests as substitutes for the liquid electrolytes. Solid state Li ion electrolytes are expected to offer several advantages over the currently commercialized liquid electrolytes such as higher thermal stability, absence of leakage and pollution, and a large electrochemical stability window [4]. In addition, the high elastic modulus in ceramics makes them suitable for the rigid thin film micro-batteries. Current solid state Li ionic conductors can be divided into four groups – NASICON type, perovskite type, LiPON type, and garnet type. The following sections contain a brief introduction of each category.

1.2.3.2.1 NASICON structured electrolytes

The NASICON (Na super ionic conductor)-type solid electrolytes are of increasing interest because of their potential to replace hybrid electrolytes in LIBs. The general formula of a NASICON-type electrolyte is $LiM_2(PO_4)_3$, where M=Ti, Ge, or Hf. NASICON consists of a covalent skeleton $M_2(PO_4)_3^-$ containing MO_6 octehedra and PO_4 tetrahedra, as shown in Figure 1.4 [15]. The Li sites sit in the interstitials between the MO_6 octehedra and PO_4 tetrahedra [16]. The main factors that limit the use of NASICON-type electrolytes are grain boundary effects, which behave as the scattering sites for ion transportation, thereby reducing the bulk ionic conductivity to 10^{-5} S/cm^2[17].

It has been reported that in $Li_{1+x}Ti_{2-x}R_x(PO_4)_3$, the lithium ion conductivity can be increased through the substitution of Ti^{4+} by other elements [18-22] (see Table 1.7). The substitution of the more stable Al^{3+} for the less stable Ti^{4+} increases the M-O bond strength and decreases the Li-O bond strength which results in the higher ionic conductivity [18, 23-29]. Among the various doped NASICON electrolytes, an optimal ionic conductivity of $1.3x10^{-3}$ S/cm has been reported for the simultaneous doping of B and Al in $LiTi_2(PO_4)_3$ [30]. Despite this, the highest reported Li ion conductivity in NASICON-based microbatteries utilizing $Li_{1.3}Al_{0.3}Ti_{1.7}(PO_4)_3$ thin film electrolyte is $2.7x10^{-6}$ S/cm only (see Figure 1.5) with a 0.2% capacitance loss per charging cycle [31-33]. Even though substitution provides an enhancement to the ionic conductivity, NASICON still possess many drawbacks, including the fact that they are not stable when in contact with lithium metal because of the rapid Ti^{4+} reduction [34-36], which greatly hinders their potential in LIBs.

1.2.3.2.2 Perovskite structured electrolytes

Another classification of promising Li ion conductors are the perovskite (ABO_3) type oxides (see Figure1.6). The ionic conductivity of these oxides is very sensitive to both the lithium content and the concentration of A-site vacancies [37-42]. A-site vacancies allow the lithium ions to hop by a vacancy mechanism through a planar bottle neck formed by four neighboring oxygen. The optimal lithium vacancy concentration has been found to be in the range of 0.44-0.45 [43]. The highest Li ion conductivity of a perovskite structured $Li_{3x}La_{2/3-x}TiO_3$ (LLTO) thin film electrolyte was reported to be $5.25x10^{-5}$ S/cm; see Figure 1.7 [44].

The main factors that limit the perovskite electrolytes in Li ion batteries are: the large amount of Li intercalation that occurs when in contact with the Li electrode and the coexistence of Ti^{4+} and Ti^{3+} that leads to an increased electronic conductivity [34]. This facile Ti^{4+} reduction makes perovskite solid electrolytes unstable with Li metal. In addition, lithium deficiencies have been observed during the high temperature sintering process, which makes it difficult to control the lithium content and therefore the ionic conductivity [45, 46].

1.2.3.2.3 LIPON structured electrolytes

Lithium phosphorous oxy-nitride (LiPON) electrolytes with the composition $Li_xPO_yN_z$, where $x=2y+3z-5$, have a moderate Li ion conductivity (~10^{-6} S/cm) and are stable in contact with metallic lithium up to a potential of 5.5 volts [47-50]. Figure 1.8 shows a typical Nyquist plot of LiPON thin film [51]. It consists of a high frequency semicircle caused by the bulk LiPON film and a low frequency line caused by the interfaces between the film and electrodes. LiPON is widely used as an amorphous thin film electrolyte for the lithium microbatteries with the highest reported ionic conductivity of $3.1x10^{-6}$ S/cm [51]. In order to address some of the shortcomings of LiPON-based electrolytes, many strategies have been explored to synthesize LiPON with improved ionic conductivity and proper crystallinity [52-54]. However, most of the synthesis strategies do not produce crystalline LiPON. Recently, Senevirathne et al. have reported successful synthesis of a new crystalline LiPON with similar conductivity by using the solid state method [55]. An important advantage of LiPON over other solid state electrolytes is its good stability and excellent cyclability [51, 56]. While

LiPON-based LIBs do show improvement over other battery classes, mainly due to their compatibility with lithium, their overall ionic conductivities have been limited.

1.2.3.2.4 Garnet structured electrolytes

Recently, oxides with garnet related structures have gained a lot of attention as the potential solid state electrolyte for LIBs. The typical structure of garnets is $A_3B_2C_3O_{12}$ with CO_4 tetrahedra and BO_6 octahedra that are connected via edge sharing [57]. Although this is the general formula, it has been reported that increasing the number of lithium per formula unit to five, such as in $Li_5Ln_3B'_2O_{12}$ (B'=Bi, Sb, Na, Ta), results in a three orders of magnitude increase in ionic conductivity [58]. In this formula, Ln can be substituted by group II elements in order to possess more Li, in which case it has an ionic conductivity of $4x10^{-5}$ S/cm [34]. A further increase on the Li contained per formula unit to 7, in $Li_7La_3B''_2O_{12}$ (B'' =Zr, Hf, Sn), has likewise attracted attention recently. The highest ionic conductivity in garnet-related structures has been reported to be $4x10^{-4}$ S/cm^2 at room temperature for the cubic $Li_7La_3Zr_2O_{12}$ (LLZO) [59]. In addition, LLZO shows good thermal stability against lithium metal, air, and moisture, further showcasing its potential as a SSE material for future LIBs. Because of this, much of the current research in solid state electrolytes has been on garnet-type materials. In order to accurately explain and delineate the novel research to be presented, the next sections are strictly devoted to the mechanism behind, and the behavior of, garnet electrolytes.

LLZO can exhibit two crystal structures, cubic or tetragonal [60, 61], the Li sub-lattices for which are shown in Figure 1.9 and Figure 1.10, respectively. In the LLZO structure, Li positions are generally referred to as Li(1) if they are tetrahedrally

coordinated to oxygen, and as Li(2) if they are octahedrally coordinated. For the cubic structure, Li(1) and Li(2) sites are shown in Figure 1.9 (b) and (c), respectively. In the tetragonal structure, the Li ions occupy one tetrahedral site, and two distorted octahedral sites, Li(2) and Li(2'), as shown in Figure 1.10 (b) and (c). However, in order for Li ion conduction to occur, there must exist adequate lithium vacancies in the sub-lattice to facilitate lithium migration. It has been reported that, in the cubic phase, the Li sub-lattice is always disordered, such that there does not exist any long range lithium ion-vacancy ordered arrangement [62]. For the tetragonal phase, the Li sub-lattice is always ordered, exhibiting a regularly ordered lithium ion-vacancy structure. [62, 63]. The resulting structure, whether it is cubic or tetragonal, can be directly controlled through alterations in the synthesis parameters.

Table 1.8 lists some reports on synthesis methods and characterization of LLZO using solid state and sol-gel techniques [57, 59, 61, 64, 65]. It can be seen that high sintering temperatures (1453 K or above) and long sintering time (above 36 hours) are required to fabricate cubic LLZO by both solid state as well as sol-gel processes. The high sintering temperature and long sintering time cause lithium deficiencies in the structure, so extra lithium is usually required to compensate for lithium losses during high temperature sintering.

1.2.4 Diffusion, defects, and ionic conduction

1.2.4.1 Theories of diffusion

The Li diffusivity determines the key performances of Li ion batteries, including charge-discharge rates, energy capacity, and cycle stability. The ionic diffusive motion in ceramic electrolyte can be well described by Fick’s law

$$J = -D\,\nabla \cdot C \tag{1.1}$$

where J is the ionic flux (mol/m^2s), D is the diffusivity (m^2/s), C is the concentration of a species (mol/m^3).

In general, D diffusivity can be expressed as

$$D = \gamma\,\lambda^2\Gamma \tag{1.2}$$

where Γ is the atom jump frequency (atoms/s), γ is the possibility of atoms jump, and λ is the jump distance (m).

The atom jump frequency Γ can be further modified as

$$\Gamma = \nu \exp\left(-\frac{\Delta G^a}{kT}\right) \tag{1.3}$$

where ν is the vibration frequency (1/s), ΔG^a is the activation energy (J/mol) for diffusion, and k is the Boltzmann constant (J/mol K). From thermodynamics, the ΔG^a has an expression of

$$\Delta G^a = \Delta H^M - T\Delta S^M \tag{1.4}$$

where ΔH^M is the enthalpy of atom migration (J/mol), and ΔS^M is the entropy change (J/mol K). Then the D is

$$D = \gamma\,\lambda^2\nu \exp\left(\frac{\Delta S^M}{kT}\right)\exp\left(-\frac{\Delta H^M}{kT}\right) = D_o \exp\left(-\frac{\Delta H^M}{kT}\right) \quad (1.5)$$

with a pre-exponential factor $D_o = \gamma\,\lambda^2\nu \exp\left(\frac{\Delta S^M}{kT}\right)$

Equation 1.5 provides an Arrhenius relation of the diffusivity and thermal activation nature of atoms.

1.2.4.2 Models of defects

From the atomic perspective, ionic diffusion is a migration process of atoms from a lattice site to a vacancy. Two conditions must exist in order to have atoms migration: (1) there must be a vacancy adjacent site, and (2) the atoms must have sufficient energy to beak bonds with its neighbor atoms, as described in Equation 1.5. The mechanism of atoms migrating from a normal lattice site to a vacancy is called vacancy diffusion. Because the atoms exist as charged ions, charge neutrality must be maintained if a vacancy is in the structure. One type of defect in MX materials involves a paired cation vacancy and anion vacancy which is called Schottky defect, as seen in Figure 1.11a. This defect can be imaged by removing one cation and one anion from the structure. Since the cation has the same charge as the anion, the charge neutrality of the crystal is maintained. Another type of defect is called Frenkel defect which involves a cation vacancy and a cation interstitial, as seen in Figure 1.11 b. The cation leaves its normal position and moves to an interstitial site.

The ratio of cations and anions keeps constant in the formation of either a Frenkel defect or Schottky defect. The constant ratio is called stoichiometry. For example, NaCl

is stoichiometric if the Na^+ and Cl^- ions have a ratio of 1:1. Nonstoichiomety happens when one of the ion types has two ionic states that co-exist in the structure [66]. For example, iron oxide, FeO, can have both Fe^{2+} and Fe^{3+} states. The formation of a Fe^{3+} causes an extra +1 charge compared to a Fe^{2+} ion. This may lead to the formation of a Fe^{2+} vacancy for every two Fe^{3+} ions. The crystal is no longer stoichiometric because there is one more O ion than Fe ion, but the crystal is electrically neutral, as seen in Figure 1.12.

The ion movement in crystalline materials via vacancy mechanism is described in Figure 1.13 a. The ion has to squeeze through its neighbor ions to move from one lattice site to another lattice site. The energy for this transition ΔH^M determines the ease of the ion migration.

Another type of impurity that can be found in solid electrolyte is interstitial impurity. If a crystalline material contains an interstitial impurity and the ionic radius of the interstitial impurity is relatively larger than the host ion, an expansion stress will distort the lattice. The transition energy ΔH^M and the movement of interstitial ions are relatively small and easy in the lattice expansion, as seen in Figure 1.13 b.

1.2.4.3 Theories of ionic conduction

Ionic conduction in solid electrolyte is the motion of the ion migration under an external field. In a steady state without any external field, as seen in Figure 1.14 a, the probability of ion propagating to its right is

$$p = \frac{1}{2}\,\alpha\,\nu \exp\left(-\frac{E^a}{kT}\right) \tag{1.6}$$

where α is the irreversibility of the ion jump, ν is the vibration frequency of the ion, and E^a is the activation energy of an ion. When an electric field (E) is applied on an ion of z charges with an angle of 45^o, as seen in Figure 1.14 b, the work done by the electric field between two ionic sites (d) is ½ zeEd [67].

Then the probability of ion moving to its right is

$$\overrightarrow{p} = \frac{1}{2}\,\alpha\,\nu \exp\left(-\frac{E^a - zeEd}{kT}\right) = p \exp\left(-\frac{zeEd}{2kT}\right) \tag{1.7}$$

the probability of ion moving to its left is

$$\overleftarrow{p} = \frac{1}{2}\,\alpha\,\nu \exp\left(-\frac{E^a + zeEd}{kT}\right) = p \exp\left(\frac{zeEd}{2kT}\right) \tag{1.8}$$

The average drift velocity v_{drift} is

$$v_{drift} = d\,(\overrightarrow{p} - \overleftarrow{p}) = \frac{1}{2} d \cdot p\left[\exp\left(\frac{zeEd}{2kT}\right) - \exp\left(\frac{-zeEd}{2kT}\right)\right] \tag{1.9}$$

Since the

$$\sinh(x) = \frac{1}{2}\,[\exp(x) - \exp(-x)] \tag{1.10}$$

The average drift velocity v_{drift} can be further reduced to

$$v_{drift} = d \cdot p \cdot \sinh(\frac{zeEd}{2kT}) \tag{1.11}$$

In general, the applied electric field is much smaller than the thermal energy, i.e., 1/2zeEd<< kT, the average drift velocity v_{drift} can be expressed as

$$v \sim \frac{zeEd^2p}{2kT} \tag{1.12}$$

Then the current density J is

$$J = nezv = \frac{nz^2e^2Ed^2p}{2kT} \tag{1.13}$$

From Equation 1.6,

$$J = \frac{n\alpha vz^2e^2Ed^2}{2kT}\exp\left(-\frac{E^a}{kT}\right) \tag{1.14}$$

Finally, J=σE, the ionic conductivity can be expressed as

$$\sigma = \frac{n\alpha vz^2e^2d^2}{2kT}\exp\left(-\frac{E^a}{kT}\right) \tag{1.15}$$

This ionic conductivity expression provides the insights for material scientists to engineer solid state electrolytes with enhanced ionic conductivity. Several approaches

have been made to enhance the ionic conductivity in the polycrystalline electrolyte including:

- Optimization of the preparative parameters
- Substitution of conducting cations
- Opening lattice structure by introducing large cations
- Trapping of high temperature highly conducting phases at room temperature

These approaches have been very important for electrolyte development and provided valuable understanding on ion transportation in solid electrolytes.

1.3 Electrochemical supercapacitors

The second type of energy storage devices is electrochemical capacitors (ECs) which store the electric energy through the electrical static force. The differences between the ECs and Li ion batteries are their energy density and power density, as seen in Figure 1.14. In general, electrochemical capacitors have higher power density and lower energy density than the Li ion batteries.

Through appropriate cell design, the energy density and power density of ECs can be varied by several orders of magnitude which make them extremely versatile for various applications. When an electrochemical capacitor is combined with a battery to form a hybrid system, the system can exhibit high power capacity and good specific energy. The ability to fast charge and discharge ECs is due to the fact that no slow chemical reactions or phase changes occur during charge and discharge process. ECs have several advantages over batteries including (1) high power density (discharge at high current density), (2) short time needed for fully charging, (3) long cycle life, and (4) environmental friendly (no heavy metal used) [2, 66].

1.3.1 Electrical double layer supercapacitors

The conventional EDL capacitors consist of two parallel electrodes immersed in an electrolyte, as seen in Figure 1.15a. Once the bias potential is applied across the electrodes, the double layer at the electrode and electrolyte interface is formed. The Stern model of EDL states two regions of ion distribution, as seen in Figure 1.15 b. In the inner Helmholtz plane (IHP), ions are strongly absorbed by the electrode. The outer Helmholtz plane (OHP) is usually formed by the counter anions and is the ion diffuse layer driven by the thermal motion [67]. The capacitance of the system C_{dl} is the combination of the compact double layer C_H and the diffusion region capacitance C_{diff}, as shown by the following equation

$$\frac{1}{C_{dl}} = \frac{1}{C_H} + \frac{1}{C_{diff}} \tag{1.16}$$

The capacitance of a parallel plate capacitor is

$$C = \frac{\varepsilon_r \varepsilon_0 A}{d} \tag{1.17}$$

where ε_r is the electrolyte dielectric constant, ε_0 is the permittivity of a vacuum, A is the effective area, and d is the effective thickness of electric double layer. However, most of the electrodes used in supercapacitors have porous structure and the pore curvature should be taken into consideration during the capacitance calculation. Assuming the cylindrical pore, ions enter pores and migrate toward the pore wall to form the double layer, as seen in Figure 1.16a. The capacitance is

$$C = \frac{2\pi\varepsilon_r\varepsilon_0 L}{\ln(\frac{b}{a})} \tag{1.18}$$

where L is the depth of the pore, b and a are the outer and inner radius of the pore. For nano pores, the pore size is so small that no double layer can be formed on the wall. The ions are accumulated on the center of the pore to form an electric wire, as seen in Figure 1.16b.

The energy stored between the two parallel plates can be calculated by

$$E = \frac{1}{2}\, C\, V^2 = \frac{1}{2}\, q\, V \tag{1.19}$$

where q is the amount of charges accumulated on one plate over a given voltage V.

The EDL supercapacitors are widely used as backup sources for memories and microcomputers which require high recharge rate and long cycle life [67]. In hybrid electric vehicles (HEVs), the EDL supercapacitors can store energy from regenerative braking and provide power for frequent stop and go. Table 1.9 lists some electrode materials for ECs and their properties. The highest specific energy reported in literatures for carbon-based supercapacitors is 200 F/g from porous activated carbon electrodes with high surface area, as seen in Figure 1.17. A typical activated carbon has a Brunauer-Emmett-Teller (BET) specific surface area in a range of 1000-2000 m^2/g and a pore size distribution between 2-5 nm [68]. However, EDL capacitors have disadvantages of having lower energy density which limit their applications. Research

has been focused on increasing energy density without sacrificing cycle life or high power density.

1.3.2 Pseudo supercapacitors

One of the ways to improve the energy density of supercapacitors is to have a rapid redox reaction during the polarization process. Many materials have been investigated as the electrode materials, including high surface area carbon materials, metal oxides, and conducting polymers, as seen in Figure 1.18. It is clear that conducting polymer electrodes give the highest specific capacitance among all the carbon-based and oxides-based electrodes. The high specific capacitance of pseudo-capacitors has made them become the best candidate to fill in the gap between the batteries and ECs.

The most common metal oxides used in the supercapacitor electrodes are RuO_2, MnO_2, CuO, and NiO [72-74]. These materials were chosen because of their relatively rapid redox reactions. Among these oxide materials, RuO_2 exhibits the highest specific capacitance of 730 F/g. However, its applications are limited due to the toxicity and high cost. Both the NiO and MnO_2 have also been reported to have pseudocapacitive behaviors with limited improvement in specific capacitance. The efficiency of gained specific capacitance is low due to the high resistance between the electrode materials and the current collectors.

The conducting polymers used in supercapacitors are polyanilines (PANIs), polypyrroles (PPYs), and polythiophene (PTs) [75-77]. The conducting polymer electrodes generate much higher specific capacitance than the metal oxides, as seen in Figure 1.18. These materials, despite their large specific capacitance values, have been limited in applications due to their poor stabilities. It has been reported that specific

capacitance of the conducting polymers decays rapidly within 20 cycles due to the electrode degradation [76].

1.3.3 Theories of impedance spectroscopy

Electrochemical impedance spectroscopy (EIS) has become one of the most popular analytical tools in materials research. EIS is an extraordinarily versatile and informative technique to study electrochemical kinetics and conduction mechanism for various materials [78]. The fundamental concept of EIS comes from Ohm's Law which defines resistance in terms of the ratio between input voltage and output current

$$R = \frac{V}{I} \tag{1.20}$$

An ideal resistor follows Ohm's Law at all current, voltage, and AC frequency levels. A non-ideal resistance is called impedance which takes phase differences between input voltage and output current into account [78]. A sinusoidal current responses to a sinusoidal input voltage with a phase shift, as seen in Figure 1.19.

The voltage signal V(t) is a function of time t and radial frequency ω

$$V(t) = V_A \sin(\omega t) \tag{1.21}$$

The current I(t) is shift in phase ϕ

$$I(t) = I_A \sin(\omega t + \phi) \tag{1.22}$$

Using Euler's relationship, it is also possible to express the potential and current as complex functions

$$V(t) = V_A e^{i\omega t} \tag{1.23}$$

$$I(t) = I_A e^{i\omega t - i\phi} \tag{1.24}$$

The impedance is then expressed as

$$Z^* = \frac{V}{I} = Z_A e^{i\phi} = Z_A(cos\phi + isin\phi) = Z_{REAl} + iZ_{IM} \tag{1.25}$$

The phase angle ϕ at a frequency ω is a ratio of the imaginary and real impedance components

$$tan\phi = \frac{Z_{IM}}{Z_{Real}} \quad or \quad \phi = \arctan\left(\frac{Z_{IM}}{Z_{REAL}}\right) \tag{1.26}$$

1.3.3.1 Basic RC circuit

A basic R|C circuit (Figure 1.20) is characterized by a capacitance C that only allows high AC frequency current to pass through with an impedance Z=1/ωC and a finite resistor which only passes through low frequency current. At the low frequency (ω~0) the capacitance impedance Z=1/ωC becomes very large and rejects the current flow, the entire current passes through the resistor as I=V/R.

$$Z(\omega) = \frac{R}{(1+(\omega RC)^2)} - i\,\frac{\omega R^2 C}{(1+(\omega RC)^2)} = Z_{REAL} + iZ_{IM} \quad (1.27)$$

$$Z_{TOTAL} = \frac{R}{\sqrt{1+(\omega RC)^2}} \quad (1.28)$$

Interesting, although R is frequency independent, Z_{REAL} is frequency dependent. At high frequency $Z_{REAL} = 0$ and low frequency $Z_{REAL} = R$. On the other hand, $Z_{IM} = -1/\omega C$ at high frequency and $Z_{IM} = 0$ at low frequency.

1.3.3.2 Randles circuit

A Randles circuit is used for many aqueous and ionic systems. It includes a solution resistance R_{SOL}, and a R|C circuit of a double layer capacitor C_{DL} with a charge transfer resistor R_{CT}, as seen in Figure 1.21.

$$Z(\omega) = R_{SOL} + \frac{R_{CT}}{(1+(\omega R_{CT} C_{DL})^2)} - i\,\frac{\omega {R_{CT}}^2 C_{DL}}{(1+(\omega R_{CT} C_{DL})^2)} = Z_{REAL} + iZ_{IM} \quad (1.29)$$

The solution resistance RSOL can be determined as the intercept of the X-axis at very high frequency. The x-axis intercept at low frequency is $Z_{REAL} = R_{SOL} + R_{CT}$. The charge transfer resistor R_{CT} is controlled by Faradaic reaction between the electro-active materials and the solution ions. The charge transfer resistor R_{CT} takes into account of all the resistors of electron transferring in the electrode [78].

1.3.3.3 Mixed charge transfer and diffusion controlled applications

Diffusion and charge transfer are usually coupled. A typical electrochemical reaction is a combination of mass transfer of charged species to the electrode surface and their redox discharge at the electrode surface [78]. Figure 1.22 shows an equivalent circuit for a typical electrochemical cell.

The charge transfer resistor R_{CT} is defined as

$$R_{CT} = \frac{RT}{zFi_0} \tag{1.30}$$

where R is gas constant, T is temperature, z is number of electrons, F is Faraday constant, and i_0 is the exchange current density.

The Warburg diffusion component can be derived as

$$Z_W(\omega) = \frac{\sigma_D(1-i)}{\sqrt{\omega}} \tag{1.31}$$

where σ_D is the Warburg diffusion coefficient.

The overall impedance is

$$Z(\omega) = R_{SOL} + \frac{R_{CT}+Z_W}{1+i\omega C_{DL}(R_{CT}+Z_W)} \tag{1.32}$$

$$Z(\omega) = R_{SOL} + \frac{\frac{RT}{zFi_0}+\frac{\sigma_D(1-i)}{\sqrt{\omega}}}{1+ i\omega C_{DL}(\frac{RT}{zFi_0}+\frac{\sigma_D(1-i)}{\sqrt{\omega}})} \tag{1.33}$$

$$Z(\omega) = R_{SOL} + \frac{R_{CT}+\frac{\sigma_D}{\sqrt{\omega}}}{\left(\frac{\sigma_D}{\sqrt{\omega}}C_{DL}+1\right)^2+\omega^2 C_{DL}^2\left(R_{CT}+\frac{\sigma_D}{\sqrt{\omega}}\right)^2} - i\frac{\left[\omega C_{DL}\left(R_{CT}+\frac{\sigma_D}{\sqrt{\omega}}\right)^2+\left(\frac{\sigma_D}{\sqrt{\omega}}C_{DL}+1\right)\right]}{\left(\frac{\sigma_D}{\sqrt{\omega}}C_{DL}+1\right)^2+\omega^2 C_{DL}^2\left(R_{CT}+\frac{\sigma_D}{\sqrt{\omega}}\right)^2}$$

(1.34)

This complex EIS model provides an operational principle to analyze the mechanisms and kinetics of electrochemical devices including Li ion batteries and supercapacitors.

1.4 References

[1] Etacheri V., Marom R., Elazari R., Salitra G., Aurbach D., Challenges in the development of advanced Li-ion batteries: a review, Energy & Environmental Science 2011;4:3243-3262.

[2] Hugins R. A., *Energy Storage*. Springer, New York, 2010.

[3] Claus Daniel, O. J., Besenhard, *Handbook of Battery Materials*. John Wiley & Sons, 1999.

[4] David Linden, Reddy T. B., *Handbook of Batteries*. R. R. Donnelley & Sons, New York, 2002.

[5] de las Casas C., Li W., A review of application of carbon nanotubes for lithium ion battery anode material, Journal of Power Sources 2012;208:74-85.

[6] Roberts A. D., Li X., Zhang H., Porous carbon spheres and monoliths: morphology control, pore size tuning and their applications as Li-ion battery anode materials, Chemical Society reviews 2014.

[7] Zhou Y.-N., Xue M.-Z., Fu Z.-W., Nanostructured thin film electrodes for lithium storage and all solid state thin-film lithium batteries, Journal of Power Sources 2013;234:310-332.

[8] Park M. S., Wang G. X., Liu H. K., Dou S. X., Electrochemical properties of Si thin film prepared by pulsed laser deposition for lithium ion micro-batteries, Electrochimica Acta 2006;51:5246-5249.

[9] Weydanz W. J., Wohlfahrt-Mehrens M., Huggins R. A., A room temperature study of the binary lithium-silicon and the ternary lithium-chromium-silicon system for use in rechargeable lithium batteries, Journal of Power Sources 1999;81-82:237-242.

[10] Yang J., Wachtler M., Winter M., Besenhard J. O., Sub-Microcrystalline Sn and Sn-SnSb Powders as Lithium Storage Materials for Lithium-Ion Batteries, Electrochemical and Solid State Letters 1999;2:161-163.

[11] Zhang W.-J., A review of the electrochemical performance of alloy anodes for lithium-ion batteries, Journal of Power Sources 2011;196:13-24.

[12] M. Wakihara, Yamamoto O., Wiley - VCH, Tokyo, 1998.

[13] Choi D., Wang D., Bae I.-T., Xiao J., Nie Z., Wang W., Viswanathan V. V., Lee Y. J., Zhang J.-G., Graff G. L., LiMnPO4 nanoplate grown via solid state reaction in molten hydrocarbon for Li-ion battery cathode, Nano letters 2010;10:2799-2805.

[14] Yuan L.-X., Wang Z.-H., Zhang W.-X., Hu X.-L., Chen J.-T., Huang Y.-H., Goodenough J. B., Development and challenges of LiFePO4 cathode material for lithium-ion batteries, Energy & Environmental Science 2011;4:269-284.

[15] Knauth P., Inorganic solid Li ion conductors: An overview, Solid State Ionics 2009;180:911-916.

[16] Key B., Schroeder D. J., Ingram B. J., Vaughey J. T., Solution-based synthesis and characterization of lithium-ion conducting phosphate ceramics for lithium metal batteries, Chem. Mater. 2011;24:287-293.

[17] Gellert M., Gries K. I., Yada C., Rosciano F., Volz K., Roling B., Grain boundaries in a lithium aluminum titanium phosphate-type fast lithium ion conducting glass ceramic: microstructure and nonlinear ion transport properties, J. Phys. Chem. C 2012;116:22675-22678.

[18] Nagata K., Nanno T., All solid battery with phosphate compounds made through sintering process, J. Power Sources 2007;174:832-837.

[19] Peng H., Xie H., Goodenough J. B., Use of B_2O_3 to improve Li+-ion transport in $LiTi_2(PO_4)_3$-based ceramics, J. Power Sources 2012;197:310-313.

[20] Bounar N., Benabbas A., Bouremmad F., Ropa P., Carru J.-C., Structure, microstructure and ionic conductivity of the solid solution $LiTi_{2-x}Sn_x(PO_4)_3$, Physica B 2012;407:403-407.

[21] Johnson P., Sammes N., Imanishi N., Takeda Y., Yamamoto O., Effect of microstructure on the conductivity of a NASICON-type lithium ion conductor, Solid State Ionics 2011;192:326-329.

[22] Jadhav H. S., Cho M.-S., Kalubarme R. S., Lee J.-S., Jung K.-N., Shin K.-H., Park C.-J., Influences of B_2O_3 addition on the ionic conductivity of $Li_{1.5}Al_{0.5}Ge_{1.5}(PO_4)_3$ glass ceramics, J. Power Sources 2013.

[23] Arbi K., Lazarraga M. G., Ben Hassen Chehimi D., Ayadi-Trabelsi M., Rojo J. M., Sanz J., Lithium mobility in $Li_{1.2}Ti_{1.8}R_{0.2}(PO_4)_3$ compounds (R = Al, Ga, Sc, In) as followed by NMR and impedance spectroscopy, Chem. Mater. 2003;16:255-262.

[24] Arbi K., Mandal S., Rojo J. M., Sanz J., Dependence of ionic conductivity on composition of fast ionic conductors $Li_{1+x}Ti_{2-x}Al_x(PO_4)_3$, $0 \leq x \leq 0.7$. A parallel NMR and electric impedance study, Chem. Mater. 2002;14:1091-1097.

[25] Huang L., Wen Z., Wu M., Wu X., Liu Y., Wang X., Electrochemical properties of $Li_{1.4}Al_{0.4}Ti_{1.6}(PO_4)_3$ synthesized by a co-precipitation method, J. Power Sources 2011;196:6943-6946.

[26] Takada K., Tansho M., Yanase I., Inada T., Kajiyama A., Kouguchi M., Kondo S., Watanabe M., Lithium ion conduction in $LiTi_2(PO_4)_3$, Solid State Ionics 2001;139:241-247.

[27] Duluard S., Paillassa A., Puech L., Vinatier P., Turq V., Rozier P., Lenormand P., Taberna P.-L., Simon P., Ansart F., Lithium conducting solid electrolyte

$Li_{1.3}Al_{0.3}Ti_{1.7}(PO_4)_3$ obtained via solution chemistry, J. Eur. Ceram. Soc. 2013;33:1145-1153.

[28] Kotobuki M., Koishi M., Preparation of $Li_{1.5}Al_{0.5}Ti_{1.5}(PO_4)_3$ solid electrolyte via a sol–gel route using various Al sources, Ceram. Int. 2013;39:4645-4649.

[29] Xiao Z.-b., Chen S., Guo M.-m., Influence of Li_3PO_4 addition on properties of lithium ion-conductive electrolyte $Li_{1.3}Al_{0.3}Ti_{1.7}(PO_4)_3$, T. Nonferr. Metal. Soc. 2011;21:2454-2458.

[30] Chen H., Tao H., Wu Q., Zhao X., Crystallization kinetics of superionic conductive Al(B, La)- incorporated $LiTi_2(PO_4)_3$ glass-ceramics, J. Am. Ceram. Soc. 2013;96:801-805.

[31] Wu X., Chen S., Mai F., Zhao J., He Z., Influence of the annealing technique on the properties of Li ion-conductive $Li_{1.3}Al_{0.3}Ti_{1.7}(PO_4)_3$ films, Ionics 2013;19:589-593.

[32] Wu X., Liu J., Li R., Chen S., Ma M., Preparation and characterization of $LiMn_2O_4/Li_{1.3}Al_{0.3}Ti_{1.7}(PO_4)_3/LiMn_2O_4$ thin-film battery by spray technique, Russ. J. Electrochem. 2011;47:917-922.

[33] Popovici D., Nagai H., Fujishima S., Akedo J., Preparation of lithium aluminum titanium phosphate electrolytes thick films by aerosol deposition method, J. Am. Ceram. Soc. 2011;94:3847-3850.

[34] Ohta S., Kobayashi T., Asaoka T., High lithium ionic conductivity in the garnet-type oxide Li_{7-X} $La_3(Zr_{2-X}, Nb_X)O_{12}$, J. Power Sources 2011;196:3342-3345.

[35] Kotobuki M., Kanamura K., Sato Y., Yoshida T., Fabrication of all solid state lithium battery with lithium metal anode using Al_2O_3-added $Li_7La_3Zr_2O_{12}$ solid electrolyte, J. Power Sources 2011;196:7750-7754.

[36] Kotobuki M., Kanamura K., Sato Y., Yamamoto K., Yoshida T., Electrochemical properties of $Li_7La_3Zr_2O_{12}$ solid electrolyte prepared in argon atmosphere, J. Power Sources 2012;199:346-349.

[37] Emery J., Buzare J. Y., Bohnke O., Fourquet J. L., Lithium-7 NMR and ionic conductivity studies of lanthanum lithium titanate electrolytes, Solid State Ionics 1997;99:41-51.

[38] Chen K., Huang M., Shen Y., Lin Y., Nan C. W., Improving ionic conductivity of $Li_{0.35}La_{0.55}TiO_3$ ceramics by introducing $Li_7La_3Zr_2O_{12}$ sol into the precursor powder, Solid State Ionics 2013;235:8-13.

[39] Suthirakun S., Ammal S. C., Xiao G., Chen F., Huang K., zur Loye H.-C., Heyden A., Obtaining mixed ionic/electronic conductivity in perovskite oxides in a reducing environment: A computational prediction for doped $SrTiO_3$, Solid State Ionics 2012;228:37-45.

[40] Bucheli W., Durán T., Jimenez R., Sanz J., Varez A., On the influence of the vacancy distribution on the structure and ionic conductivity of A-site-deficient $Li_xSr_xLa_{2/3-x}TiO_3$ perovskites, Inorg. Chem. 2012;51:5831-5838.

[41] Li X., Zhao H., Luo D., Huang K., Electrical conductivity and stability of A-site deficient (La, Sc) co-doped $SrTiO_3$ mixed ionic-electronic conductor, Mater. Lett. 2011;65:2624-2627.

[42] Mather G. C., García-Martín S., Benne D., Ritter C., Amador U., A-site-cation deficiency in the $SrCe_{0.9}Yb_{0.1O3-\delta}$ perovskite: effects of charge-compensation mechanism on structure and proton conductivity, J. Mater. Chem. 2011;21:5764-5773.

[43] Šalkus T., Kazakevičius E., Kežionis A., Orliukas A. F., Badot J. C., Bohnke O., Determination of the non-Arrhenius behaviour of the bulk conductivity of fast ionic conductors LLTO at high temperature, Solid State Ionics 2011;188:69-72.

[44] Xiong Y., Tao H., Zhao J., Cheng H., Zhao X., Effects of annealing temperature on structure and opt-electric properties of ion-conducting LLTO thin films prepared by RF magnetron sputtering, J. Alloys Compd. 2011;509:1910-1914.

[45] Kumatani A., Ohsawa T., Shimizu R., Takagi Y., Shiraki S., Hitosugi T., Growth processes of lithium titanate thin films deposited by using pulsed laser deposition, Appl. Phys. Lett. 2012;101:123103-4.

[46] Yuan T., Cai R., Wang K., Ran R., Liu S., Shao Z., Combustion synthesis of high-performance $Li_4Ti_5O_{12}$ for secondary Li-ion battery, Ceram. Int. 2009;35:1757-1768.

[47] Bates J. B., Dudney N. J., Neudecker B., Ueda A., Evans C. D., Thin-film lithium and lithium-ion batteries, Solid State Ionics 2000;135:33-45.

[48] Nimisha C. S., Rao K. Y., Venkatesh G., Rao G. M., Munichandraiah N., Sputter deposited LiPON thin films from powder target as electrolyte for thin film battery applications, Thin Solid Films 2011;519:3401-3406.

[49] Xu F., Dudney N. J., Veith G. M., Kim Y., Erdonmez C., Lai W., Chiang Y.-M., Properties of lithium phosphorus oxynitride (Lipon) for 3D solid state lithium batteries, J. Mater. Res. 2010;25:1507-1515.

[50] Meda L., Maxie E. E., Lipon thin films grown by plasma-enhanced metalorganic chemical vapor deposition in a N_2–H_2–Ar gas mixture, Thin Solid Films 2012;520:1799-1803.

[51] Suzuki N., Shirai S., Takahashi N., Inaba T., Shiga T., A lithium phosphorous oxynitride (LiPON) film sputtered from unsintered Li_3PO_4 powder target, Solid State Ionics 2011;191:49-54.

[52] Mascaraque N., Fierro J. L. G., Durán A., Muñoz F., An interpretation for the increase of ionic conductivity by nitrogen incorporation in LiPON oxynitride glasses, Solid State Ionics 2013;233:73-79.

[53] Kim Y. G., Wadley H. N. G., The influence of the nitrogen-ion flux on structure and ionic conductivity of vapor deposited lithium phosphorus oxynitride films, J. Power Sources 2011;196:1371-1377.

[54] Fleutot B., Pecquenard B., Martinez H., Letellier M., Levasseur A., Investigation of the local structure of LiPON thin films to better understand the role of nitrogen on their performance, Solid State Ionics 2011;186:29-36.

[55] Senevirathne K., Day C. S., Gross M. D., Lachgar A., Holzwarth N. A. W., A new crystalline LiPON electrolyte: Synthesis, properties, and electronic structure, Solid State Ionics 2013;233:95-101.

[56] Ribeiro J. F., Sousa R., Carmo J. P., Gonçalves L. M., Silva M. F., Silva M. M., Correia J. H., Enhanced solid-state electrolytes made of lithium phosphorous oxynitride films, Thin Solid Films 2012;522:85-89.

[57] Masashi K., Hirokazu M., Kiyoshi K., Yosuke S., Toshihiro Y., Compatibility of $Li_7La_3Zr_2O_{12}$ solid electrolyte to all solid state battery using Li metal anode, J. Electrochem. Soc. 2010;157:A1076-A1079.

[58] Murugan R., Weppner W., Schmid-Beurmann P., Thangadurai V., Structure and lithium ion conductivity of bismuth containing lithium garnets $Li_5La_3Bi_2O_{12}$ and $Li_6SrLa_2Bi_2O_{12}$, Mater. Sci. Eng., B 2007;143:14-20.

[59] Murugan R., Thangadurai V., Weppner W., Fast lithium ion conduction in garnet-type $Li_7La_3Zr_2O_{12}$, Angew. Chem. Int. Ed. 2007;46:7778-7781.

[60] Jin Y., McGinn P. J., Al-doped $Li_7La_3Zr_2O_{12}$ synthesized by a polymerized complex method, J. Power Sources 2011;196:8683-8687.

[61] Shimonishi Y., Toda A., Zhang T., Hirano A., Imanishi N., Yamamoto O., Takeda Y., Synthesis of garnet-type $Li_{7-x}La_3Zr_2O_{12-x}$ and its stability in aqueous solutions, Solid State Ionics 2011;183:48-53.

[62] Bernstein N., Johannes M. D., Hoang K., Origin of the structural phase transition in $Li_7La_3Zr_2O_{12}$, Phys. Rev. Lett. 2012;109:205702.

[63] Xie H., Alonso J. A., Li Y., Fernández-Díaz M. T., Goodenough J. B., Lithium distribution in aluminum-free cubic $Li_7La_3Zr_2O_{12}$, Chem. Mater. 2011;23:3587-3589.

[64] Kokal I., Somer M., Notten P. H. L., Hintzen H. T., Sol–gel synthesis and lithium ion conductivity of $Li_7La_3Zr_2O_{12}$ with garnet-related type structure, Solid State Ionics 2011;185:42-46.

[65] Awaka J., Kijima N., Hayakawa H., Akimoto J., Synthesis and structure analysis of tetragonal $Li_7La_3Zr_2O_{12}$ with the garnet-related type structure, J. Solid State Chem. 2009;182:2046-2052.

[66] Inagaki M., Konno H., Tanaike O., Carbon materials for electrochemical capacitors, Journal of Power Sources 2010;195:7880-7903.

[67] Crow D. R., *Principles And Applications Of Electrochemistry*. Chapman & Hall, New York, 1994.

[68] Burke A., R&D considerations for the performance and application of electrochemical capacitors, Electrochimica Acta 2007;53:1083-1091.

[69] Raymundo-Piñero E., Leroux F., Béguin F., A high-performance carbon for supercapacitors obtained by carbonization of a seaweed biopolymer, Advanced Materials 2006;18:1877-1882.

[70] Kim Y. J., Abe Y., Yanagiura T., Park K. C., Shimizu M., Iwazaki T., Nakagawa S., Endo M., Dresselhaus M. S., Easy preparation of nitrogen-enriched carbon materials from peptides of silk fibroins and their use to produce a high volumetric energy density in supercapacitors, Carbon 2007;45:2116-2125.

[71] Xing W., Qiao S., Ding R., Li F., Lu G., Yan Z., Cheng H., Superior electric double layer capacitors using ordered mesoporous carbons, Carbon 2006;44:216-224.

[72] Krishnamoorthy K., Kim S.-J., Growth, characterization and electrochemical properties of hierarchical CuO nanostructures for supercapacitor applications, Materials Research Bulletin 2013;48:3136-3139.

[73] Xia H., Meng Y. S., Yuan G., Cui C., Lu L., A symmetric RuO2/RuO2 supercapacitor operating at 1.6 V by using a neutral aqueous electrolyte, Electrochemical and Solid State Letters 2012;15:A60-A63.

[74] Yu G., Hu L., Liu N., Wang H., Vosgueritchian M., Yang Y., Cui Y., Bao Z., Enhancing the supercapacitor performance of graphene/MnO2 nanostructured electrodes by conductive wrapping, Nano Letters 2011;11:4438-4442.

[75] Zhang D., Zhang X., Chen Y., Yu P., Wang C., Ma Y., Enhanced capacitance and rate capability of graphene/polypyrrole composite as electrode material for supercapacitors, Journal of Power Sources 2011;196:5990-5996.

[76] Zhang K., Zhang L. L., Zhao X., Wu J., Graphene/polyaniline nanofiber composites as supercapacitor electrodes, Chemistry of Materials 2010;22:1392-1401.

[77] Alvi F., Basnayaka P. A., Ram M. K., Gomez H., Stefanako E., Goswami Y., Kumar A., Graphene-polythiophene nanocomposite as novel supercapacitor electrode material, 2011.

[78] Lvovich, Vadim F, Impedance Spectroscopy: Applications to Electrochemical and Dielectric Phenomena, John Wileys and Sons, 368, July 2012.

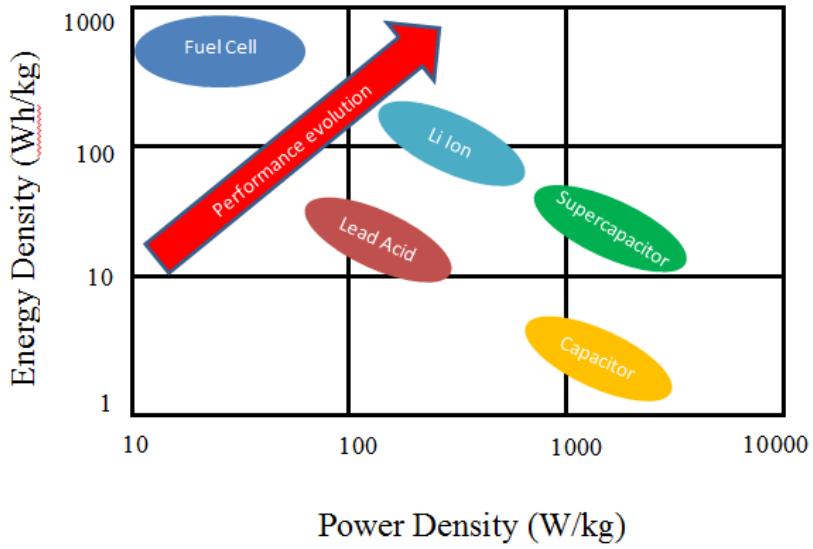

Figure 1.1. Ragone plots for various energy storage devices.

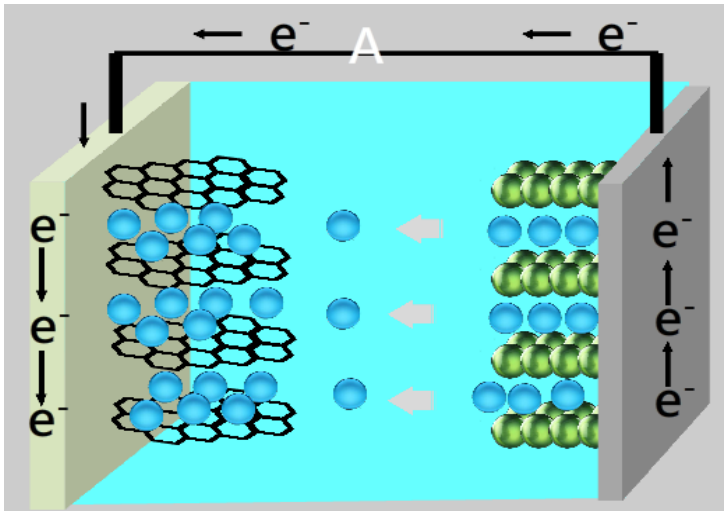

Figure 1.2. Schematic of a graphite/Li^+ electrolyte/$LiCo_2O_2$ battery. Current flow represents charge process.

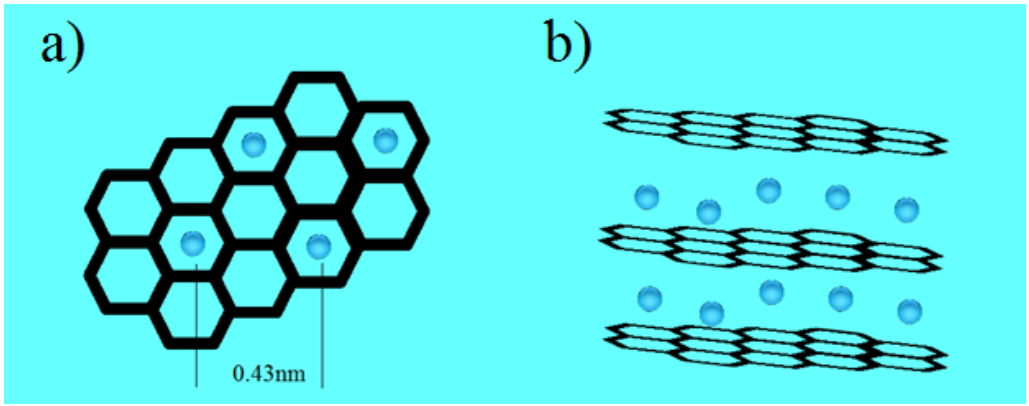

Figure 1.3. Schematic of a) in plane Li intercalation b) interlayer ordering of intercalated Li.

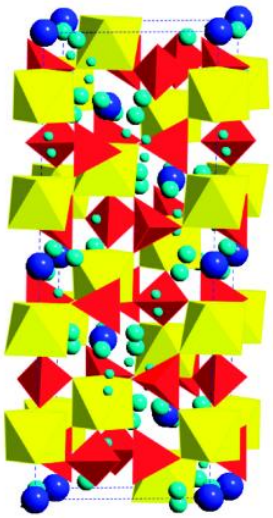

Figure 1.4. $LiTi_2(PO_4)_3$ crystal structure with blue spheres represent Li atoms, yellow octahedra represent TiO_6, and red tetrahedral represent PO_4. Reprinted with permission from [16].

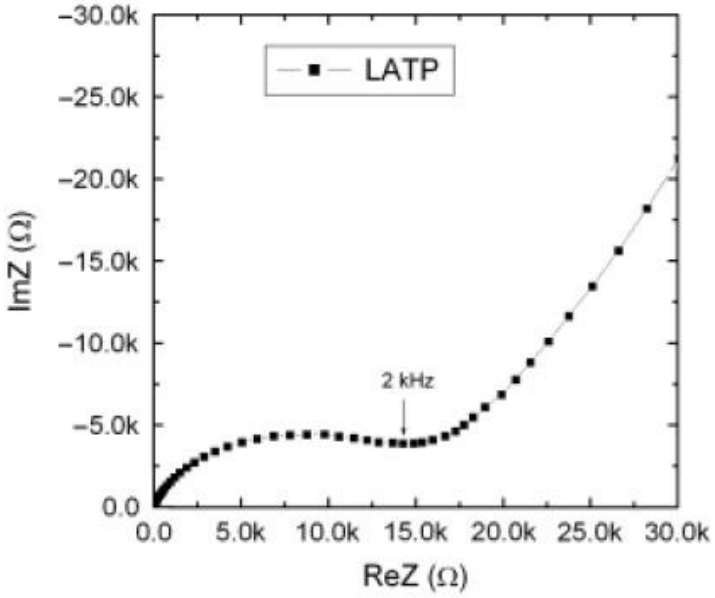

Figure 1.5 Nyquist plot for $Li_{1.3}Al_{0.3}Ti_{1.7}(PO_4)_3$ thin film at room temperature. Reprinted with permission from [33].

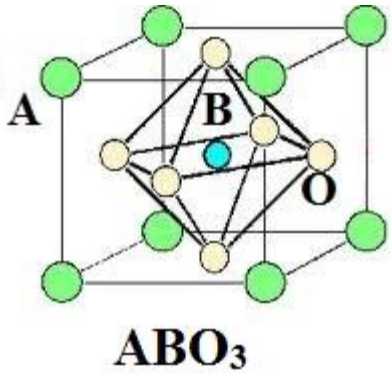

Figure 1.6. Crystal structure of perovskite (ABO_3) type oxides.

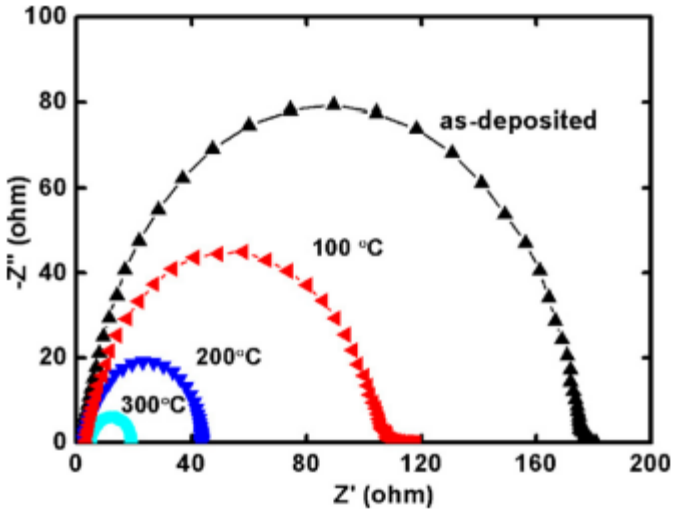

Figure 1.7. Nyquist plots for LLTO thin film with various postannealing temperatures. Reprinted with permission from [44].

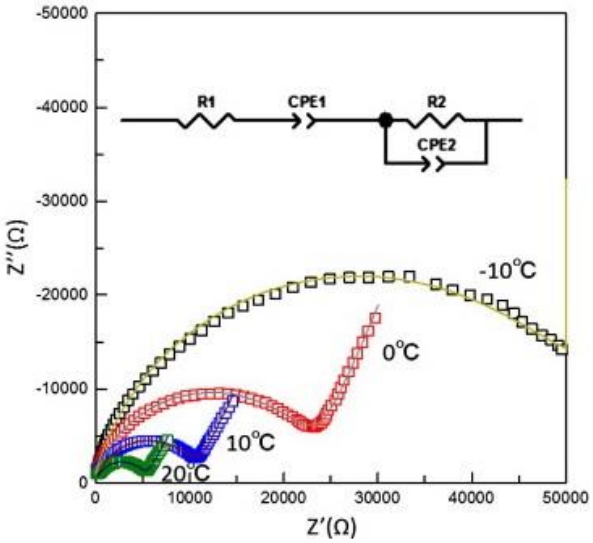

Figure 1.8. Nyquist plots for LiPON thin film measured at various temperatures. Reprinted with permission from [51].

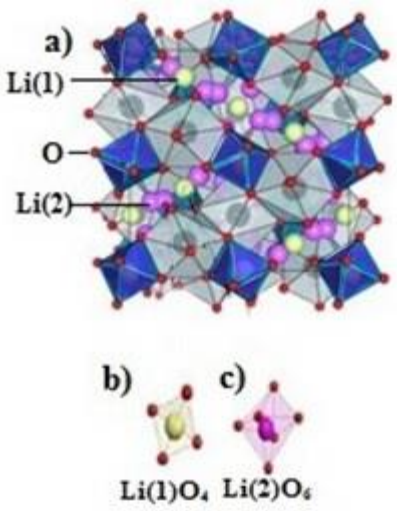

Figure 1.9. Crystal structure of a) cubic LLZO, b) tetrahedral LiO_4 site, c) octahedral LiO_6 site in cubic $Li_7La_3Zr_2O_{12}$.

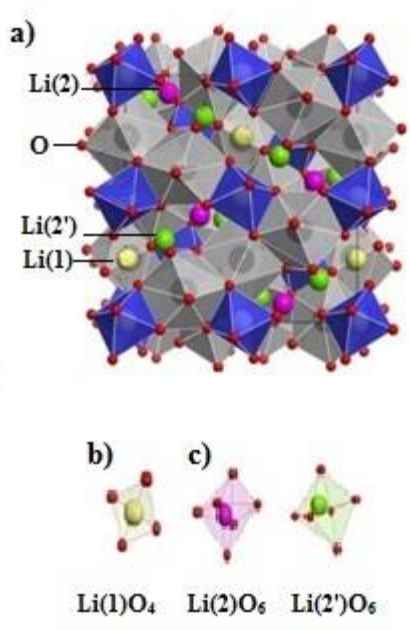

Figure 1.10. Crystal structure of a) tetragonal LLZO, b) tetrahedral LiO_4 site, c) two octahedral LiO_6 sites in tetragonal $Li_7La_3Zr_2O_{12}$. Reprinted with permission from [59].

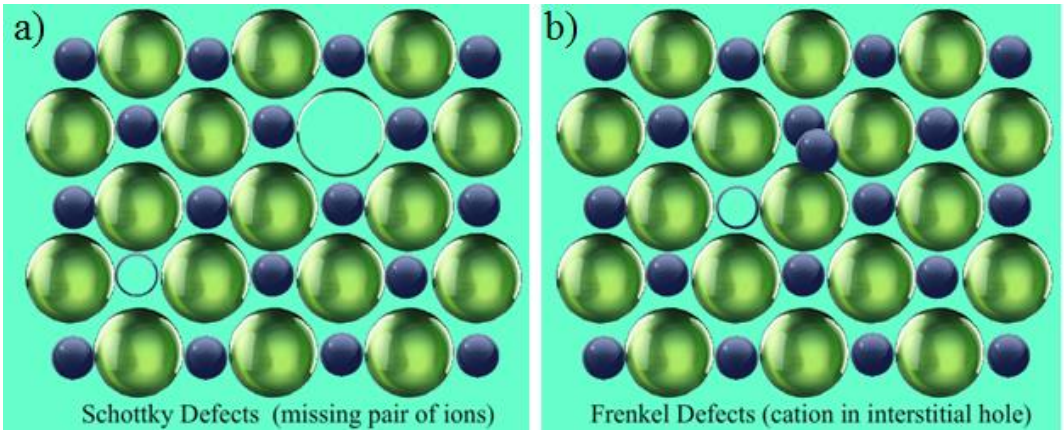

Figure 1.11. Schematic of a) Schottky defect and b) Frenkel defect.

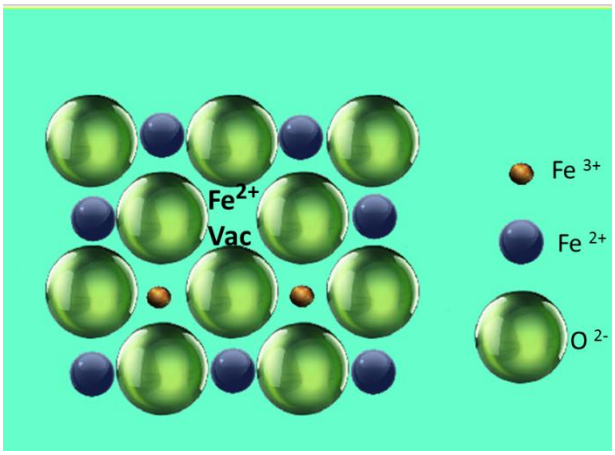

Figure 1.12. Schematic representation of a Fe^{2+} vacancy in FeO that results from the formation of two Fe^{3+} .

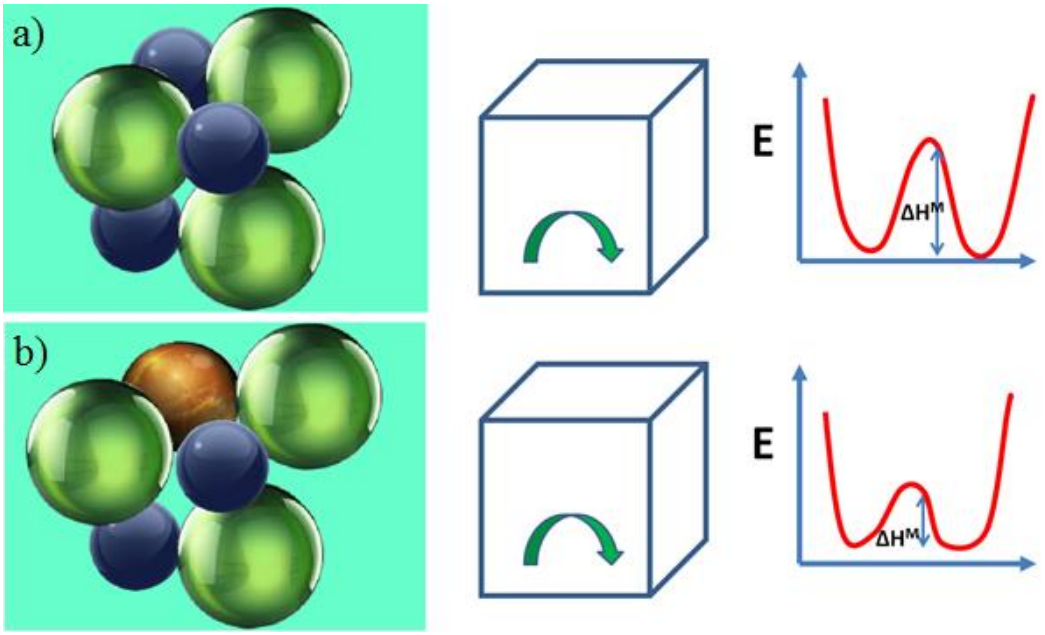

Figure 1.13. Schematic of ion diffusion in a) regular crystal structure, b) enlarged lattice when a large ion is substituted.

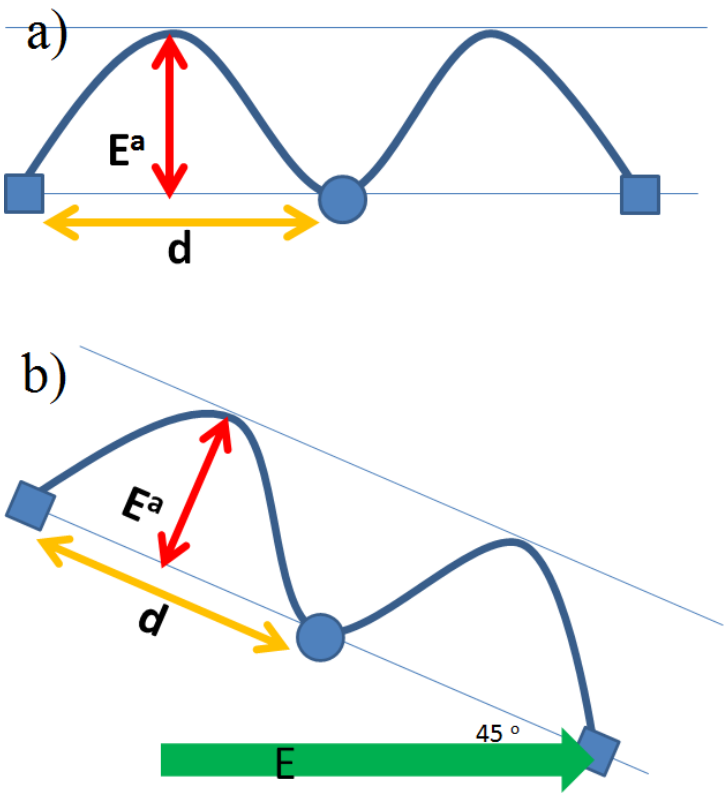

Figure 1.14. Schematic of activation energy for ion migration a) without external field, b) with 45^{o} electric field.

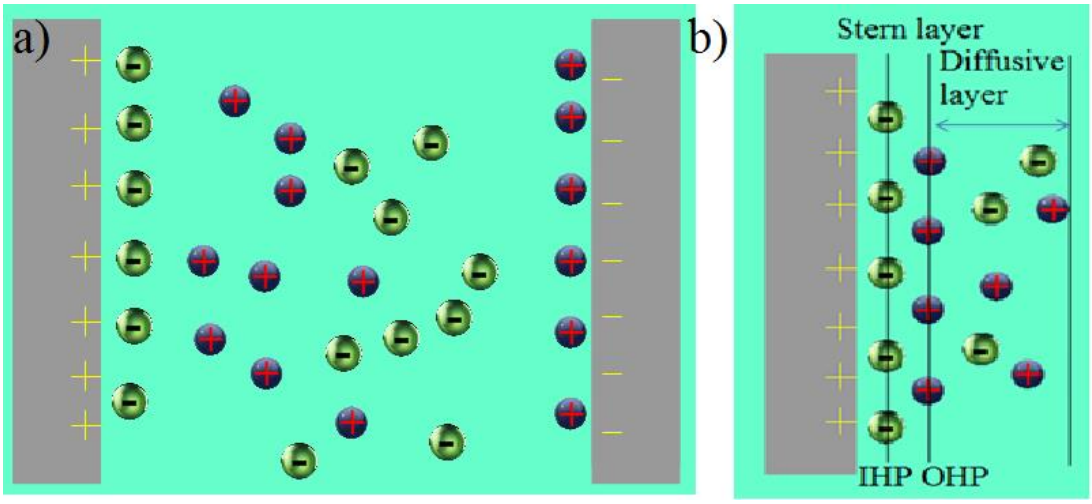

Figure 1.15. Schematics of a) EDL formation between two parallel electrodes, b) Stern's EDL model.

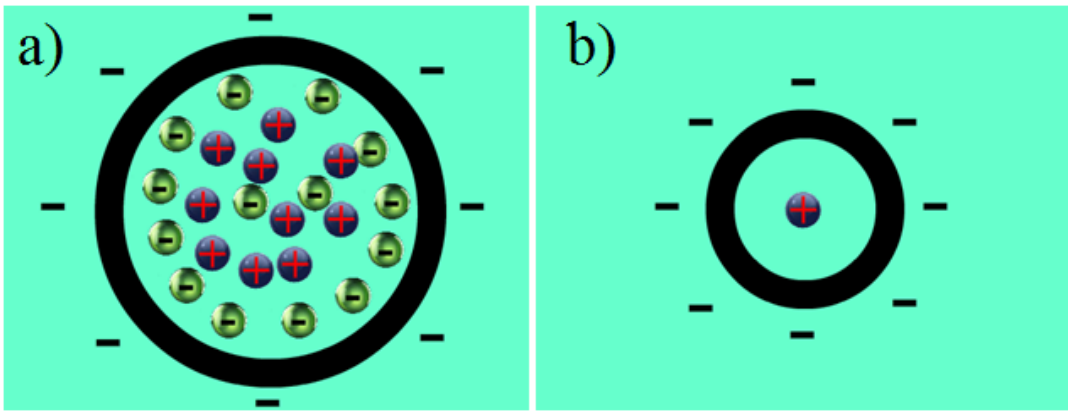

Figure 1.16. Schematics of a) EDL formation in a cylindrical pore, b) an electric wire.

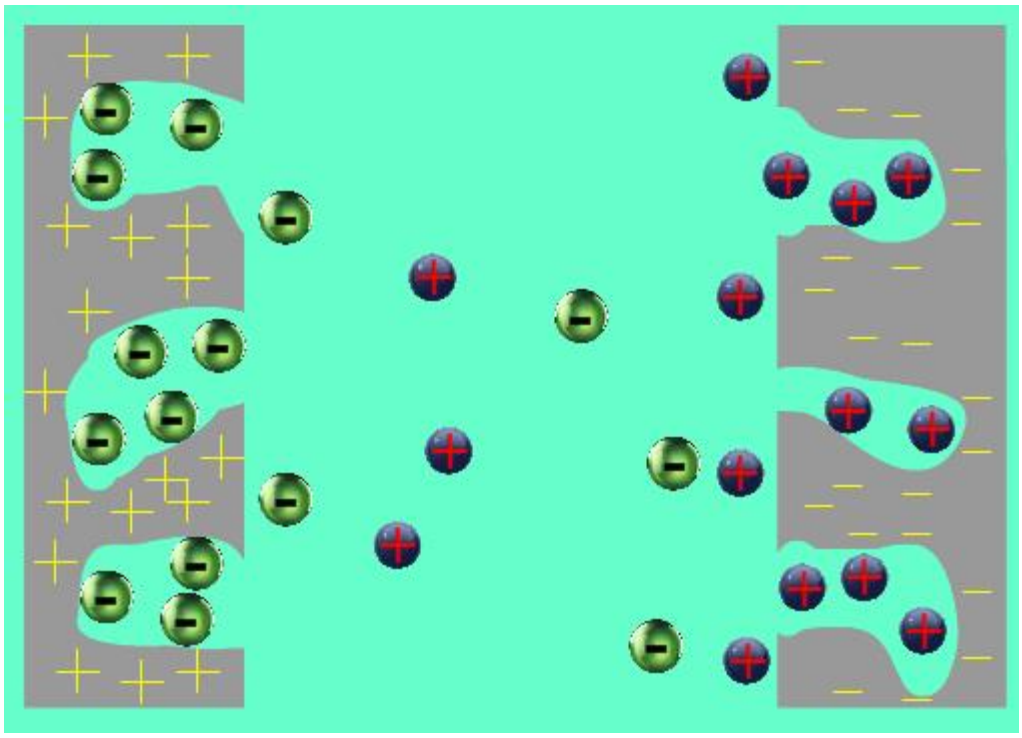

Figure 1.17. Schematic of charge storage in the activated carbon electrodes with high surface area.

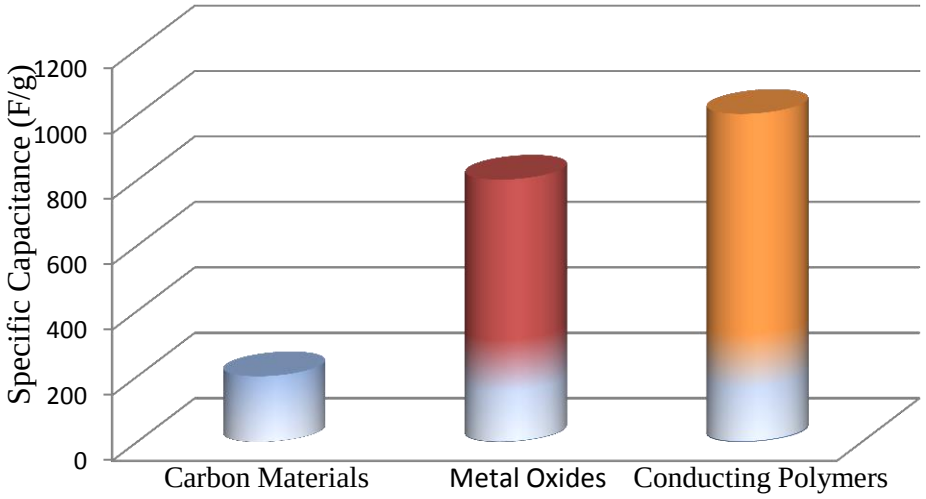

Figure 1.18. Specific capacitance profiles for various electrode materials in pseudo-supercapacitors.

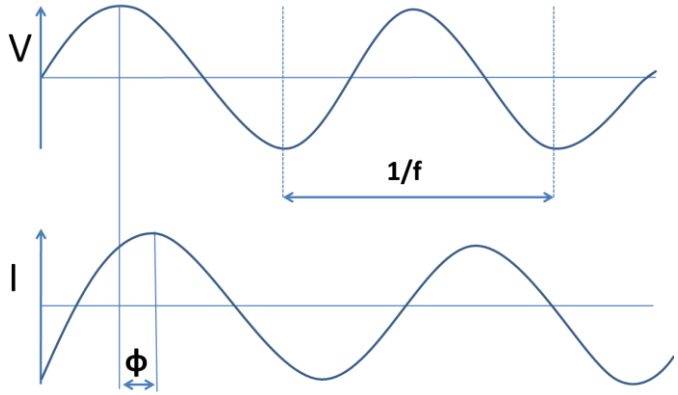

Figure 1.19. Sinusoidal voltage input at a frequency f and current response I.

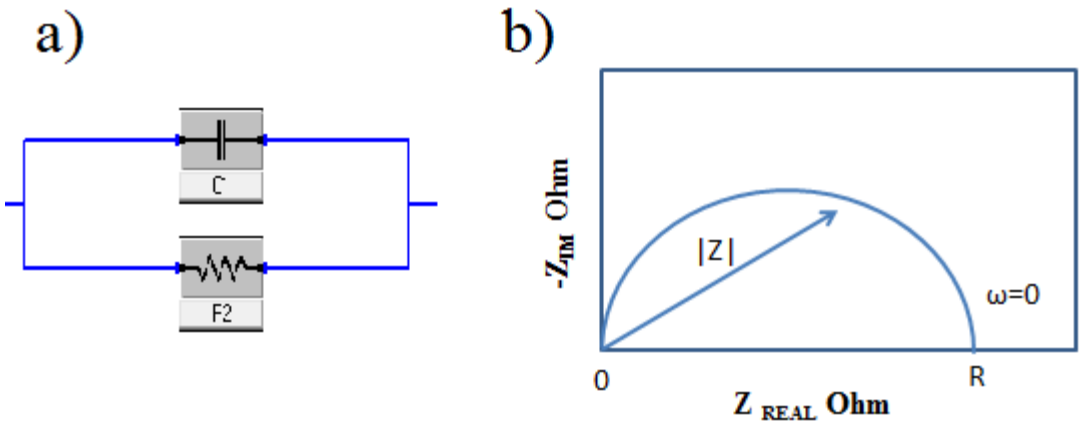

Figure 1.20. Schematics of a) R|C circuit diagram, b) Nyquist plot.

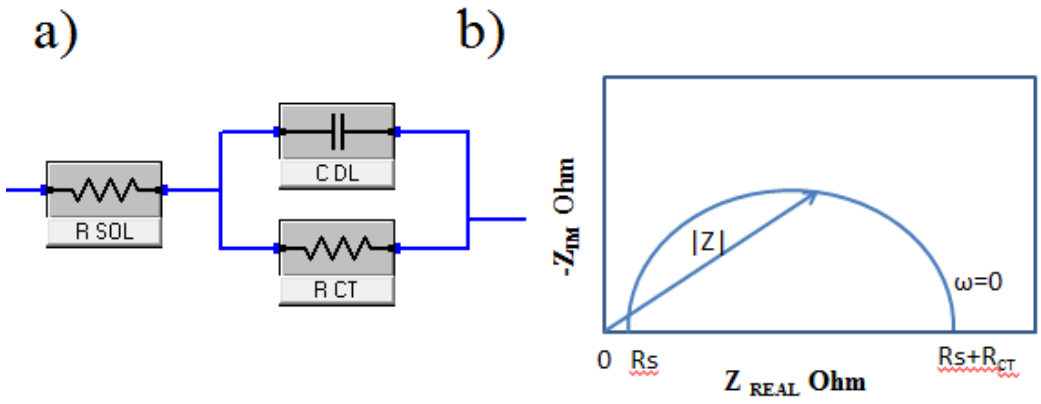

Figure 1.21. Schematics of a) Randles circuit diagram, b) Nyquist plot.

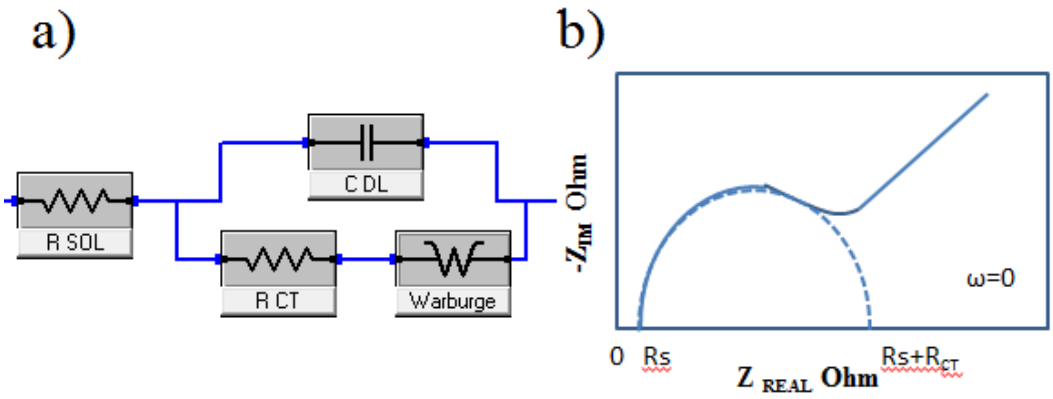

Figure 1.22. Schematics of a) circuit diagram for a mixed charge transfer and diffusion model, b) Nyquist plot for such a model.

Table 1.1 Requirements of batteries for hybrid vehicle and EV

	Energy density (Wh/kg)	Weight of the battery (Kg)	Distance on one charge (Km)
Hybrid Vehicle	40-50	60	15
Electrical Vehicle	90-100	450	150-200

Table 1.2 Advantages and disadvantages of Li ion batteries

Advantages	Disadvantages
No maintenance required	Degrade at high temperature
Long cycle life	High cost
Low self-discharge rate	Large capacity loss when over charged
High power discharge capacity	Need for protective circuit
No memory effect	Thermal runaway when crushed

Table 1.3 List of Li ion battery anode materials and their properties

Materials	Theoretical specific capacitance (mAh/g)	Potential vs Li (V)
LiAl [6]	993	0.18
Li_9Al_4[6]	2234	0.6
$Li_{22}Sn_5$[6]	994	0.9
Li_3Sb[6]	536	0.3
$Li_4Ti_5O_{12}$ [7]	175	1.6

Table 1.4 List of Li ion battery cathode materials and their properties

Cathode	Diffusivity (cm2/s)	Crystal structure
$LiCoO_2$	$8x10^{-8}$	Layered structure
$LiMn_2O_4$	$3.4x10^{-8}$	Spinel structure
$LiFePO_4$	$1.6x10^{-9}$	Olivine structure

Table 1.5 List of Li ion battery doped cathode materials and their properties

Compound	Diffusivity (cm^2/s)
$LiNi_{1-x}Co_xO_2$	$2x10^{-8}$
$LiCo_{1-x}Al_xO_2$	$3x10^{-15}$
$LiAl_xMn_{2-x}O_4$	$8x10^{-8}$
$LiB_xMn_{2-x}O_4$	$8x10^{-9}$
$LiFe_{1-x}Mn_xPO_4$	$1x10^{-8}$
$LiZn_xFe_{1-x}PO_4$	$1x10^{-11}$

Table 1.6 List of Li ion battery organic electrolytes and their properties

	Melting point (oC)	Viscosity (mPa*s)	Conductivity (S/cm)
$LiBF_4$	-82	233	0.0173
$LiPF_6$	-61	312	0.0146
$LiCF_3SO_3$	16	90	0.037
$LiCF_3CO_2$	-50	73	0.032
$LiNTf_2$	-4	52	0.039

Table 1.7 List of properties for trivalent ion doped $Li_{1+x}Ti_{2-x}R_x(PO_4)_3$ compound

R	Li ionic conductivity at room	Activation Energy (eV)
Al[18]	$6x10^{-4}$	0.28
Sn [20]	$1x10^{-4}$	0.32
B [19]	$2x10^{-4}$	0.48
Al, Si [21]	$3.8x10^{-4}$	N/A
Ge, B [22]	$6x10^{-4}$	0.33

Table 1.8 List of synthesis methods for LLZO

Synthesis Method	Excess of Li added	Processing Temperature (K)	Phase formed	Ionic Conductivity (S/cm) at Room Temperature	Activation Energy (eV)
Solid State [65]	10 %	1253 K for 5 hours	Tetragonal	$1.6x10^{-6}$	0.54
Solid State [57]	10 %	1503 K for 36 hours	Cubic	$1.8x10^{-4}$	N/A
Sol Gel [61]	10 %	1453 K for 36hours	Cubic	$5.6x10^{-4}$	0.80

Table 1.9 Published data on the capacitive performance of carbon materials

Electrode materials	Specific capacitance (F/g)
Activated carbon [69]	198
Carbon fiber [70]	50
Porous Carbon[71]	200
Carbon Aerogel [66]	108

CHAPTER 2

LASER ANNEALING OF $Li_7La_3Zr_2O_{12}$ [1]

2.1 Abstract

We are presenting our novel results on pulsed laser processing of garnet based SSEs, specifically $Li_7La_3Zr_2O_{12}$ (LLZO). LLZO powders with a tetragonal structure were prepared by a sol-gel technique, then a pulsed laser annealing process was employed to covert the powders to cubic LLZO without any loss of lithium. The tetragonal LLZO exhibited a Li ion conductivity of $1.8x10^{-7}$ S/cm, whereas the laser annealed cubic LLZO showed a Li ion conductivity of $1.0x10^{-4}$ S/cm at room temperature. A systematic study of the effect of pulsed laser annealing (PLA) on the crystal structure, morphology, composition, and ionic conductivity of LLZO was performed via X-ray diffraction (XRD), scanning electron microscopy (SEM), energy dispersive X-ray spectroscopy (EDS), and electrochemical impedance spectroscopy (EIS) measurements. These results demonstrate that PLA is a powerful processing technique for synthesizing the high ionic conductivity cubic phase of LLZO at relatively low temperatures, as compared to conventional methods.

[1] This chapter is based on the paper entitled "Recent developments in garnet based solid state electrolytes for thin film batteries," published in the Current Opinion in Solid State and Materials Science 18, p 29-38 (2014). Reprint with permission.

2.2 Introduction

Lithium ion batteries (LIB) are important for a wide variety of applications, spanning from portable electronics and hybrid automobiles to large-scale electrical power storage systems [1, 2]. These batteries offer a number of advantages over other families of batteries, such as: high energy density, long cycle lifetime, no memory effect, and a wide range of operating temperatures. Currently, the Li ion electrolytes used in LIBs are referred to as "hybrid electrolytes" because they couple a polymer with an organic solvent to induce a very high ionic conductivity in the range of 10^{-1} S/cm. However, these liquid electrolytes suffer from very serious drawbacks such as flammability, leakages, and the formation of dendrites in the electrodes.

In this respect, solid state Li ion conductors have garnered interests as substitutes for the liquid electrolytes. Recently, cubic garnet structure $Li_7La_3Zr_2O_{12}$ (LLZO) has been reported to have a high Li ion conductivity of $4x10^{-4}$ S/cm at 298 K [1], which is comparable to, or even greater than, other well-known fast Li ion conductors such as Li_3N, Li-β-Al_2O_3, or lithium phosphorous oxynitride (LIPON) [2-5]. However, the detailed crystal chemistry of Li-oxide garnets is not well understood, nor is the relationship between the crystal chemistry and the conduction behavior. LLZO has two phases: cubic and tetragonal [6-9]. The cubic phase has an ionic conductivity of 4×10^{-4}S/cm [1,6], whereas the tetragonal phase conductivity is only 3.12×10^{-7} S/cm [7].

$Li_7La_3Zr_2O_{12}$ compounds with garnet structure were first reported by Murugan et al. and were synthesized by solid state reaction at an ultra-high temperature of 1503K [3]. Due to these incredibly high temperatures, others have sought alternative routes including sol-gel synthesis to circumvent these constraints. Several reports describe the synthesis and characterization of LLZO using solid state and sol-gel techniques [3-7].

From Table 2-1, it can be seen that high sintering temperatures (1453 K or above) are required to fabricate cubic LLZO by both solid state as well as sol-gel processes. The high sintering temperature also results in a coarsening of the microstructure and an increase in the grain boundary conductivity. However, the high processing temperature causes lithium deficiencies in the structure; so extra lithium is required to compensate for lithium losses during high temperature sintering.

Several reports have suggested that introducing extrinsic impurities into LLZO during processing would increase the ionic conductivity. One type of impurity introduced in LLZO is aluminum. Some results of the Al doped LLZO are listed in Table 2-2 [8-11]. The 1wt% Al doped LLZO has a conductivity of 4.0×10^{-4} S/cm, which is close to the highest reported ionic conductivity for nondoped cubic LLZO [9]. It is observed that a critical concentration of Al can be used to stabilize the cubic LLZO at lower temperatures, thereby preventing lithium losses that occur as a result of high temperature sintering. The Al dopant provides two main improvements in the formation of the cubic LLZO. First, the Al atom acts as a sintering aid to lower the processing temperature [12]. Second, Al atoms substitute in both the tetrahedral and octahedral Li sites, which increases the Li vacancy concentration, facilitating Li transport [13].

In order to further elucidate the phase stability and conductivity behaviors of LLZO, the effects of other dopant cations such as Ga have been investigated by several groups. The reported ionic conductivities for Ga doped LLZO are in the range of 10^{-4} S/cm [14, 15]. The highest ionic conductivity of 5.4×10^{-4} S/cm was reported for 1 mole Ga doped LLZO [14]. The Ga doped LLZO has a higher ionic conductivity than the Al doped LLZO that can be explained by the relative size of Ga^{3+} compared to Al^{3+}. Doping with the larger Ga ions results in a larger lattice opening, thereby enhancing Li ion transport.

The site preference of Ga was not examined, but it can be assumed that Ga behaves in a similar manner as Al, occupying both the tetrahedral and octahedral sites.

The mechanisms of how dopants enter and influence the LLZO material are still unknown and the stability of doped LLZO has not been thoroughly investigated yet. There is possibility that secondary phases introduced by the dopant could severely affect the stability and performance of the electrolyte. In addition, these experimental studies indeed indicate that the formation of the cubic LLZO is generally associated with a significant amount of Li loss during the high temperature sintering process [9, 15-17]. Therefore, it is important to develop an alternative method to fabricate LLZO that is not reliant on the use of dopant.

Lasers provide a noncontact method of energy transfer, which can be easily controlled and localized [18]. Pulsed laser annealing is very different from conventional annealing in that the effective heating time in pulsed laser annealing is on the order of nanoseconds as opposed to furnace annealing (>10000 s). The rapid heating and cooling does not provide sufficient time for Li atoms to evaporate from the sample via diffusion. Thus the lithium cannot escape from the LLZO during laser annealing, despite its large diffusion coefficient. Very high local temperatures as well as incredibly fast heating and quenching rates are the characteristics of pulsed laser annealing; this makes lasers ideal for annealing LLZO.

2.3 Experimental procedure

A sol-gel synthesis method was used to fabricate the LLZO powder. For this, Li_2CO_3 (99%), La_2O_3 (99%), and $Zr(NO_3)_2.6H_2O$ (99%) were dissolved in nitric acid to prepare a precursor solution. The molar ratio between Li, La, and Zr was maintained at

7:3:2. Citric acid (99.5%) and ethylene glycol (in the molar ratio of 60:40) were added to the precursor solution to serve as a chelating agent. The pH of the precursor solution was adjusted to a value of 2. The resulting precursor solution was then heated at 200°C until it turned to a solidified white powder. The powder was then crushed and calcined at 1000°C for 10 hours (at 1°C/minute ramp rate) in a box furnace. After calcination, the powder was pressed into a 1" diameter pellet using a cold iso-static press by applying a load of 350MPa for 7 minutes.

For laser annealing, a KrF Compex Pro pulsed laser from Lambda Physik Inc. was used. The pulse duration was 25 ns and a pulse repetition rate of 1 Hz was utilized. In order to achieve a uniform illumination, a beam homogenizer was placed between the laser and the sample. The energy fluence was varied between 125 and 700 mJ/cm^2. The size of the laser beam was kept slightly larger than the sample size so that the entire sample area was irradiated under the same conditions. After each laser irradiation, the top surface of the pellet (which changes its color from white to light brown) was carefully scratched off using a razor blade. The collected laser annealed powder was pressed into a half inch diameter pellet.

2.4 Results and discussion

2.4.1 Crystal structure and morphology

The X-ray diffraction (XRD) patterns for the various LLZO samples are shown in Figure 2.1 The observed peaks were indexed using reported crystallographic data for LLZO garnets [19]. The XRD pattern of the as-prepared LLZO showed a tetragonal phase [4, 6, 13, 14, 20]. Upon pulsed laser annealing, the diffraction patterns changed gradually as a function of incident laser shots (each with an energy fluence of 125

mJ/cm^2) to a phase of cubic symmetry [9, 17]. The (211) peak splitting at $2\theta=16.7^o$ and the (420) peak doublet at $2\theta=30.5^o$ are the characteristics of LLZO with a tetragonal structure as shown in Figure 2.1 [9]. As can be seen in Figure 2.2a, with increased number of laser shots, the (211) peak splitting disappears and peak intensity increases. Similarly, with increased laser shots, the peak doublet and peak splitting centered at $2\theta=30.5^o$ merge into one well-defined peak and the intensity of the (420) peak increases dramatically and becomes the peak of 100% intensity (see Figure 2.2 b). All these results show that laser annealing is a very efficient technique for transforming the tetragonal LLZO to cubic phase.

A representative cross-sectional micrograph of a laser annealed LLZO sample (15 laser shots at fluence of 125mJ/cm^2) is shown in Figure 2.3. The laser penetration depth, as determined by measuring the height difference between the laser annealed brown surface and the white surface beneath it, was ~ 40 μm. SEM analysis showed that there was no significant grain size change before and after laser irradiation. This implied that the 25 ns heating time (i.e., the width of laser pulses) did not provide enough time to induce serious atomic-scale interdiffusion among the grain. At the same time, the energy supplied to material is sufficient to transform the LLZO from the tetragonal to cubic phase without melting the grains on the surface.

Figure 2.4 shows elemental mapping in LLZO after laser annealing. Lithium in the LLZO cannot be detected by EDS technique; however, the composition of the other elements can be revealed. Our EDS results showed that La, Zr, and O elements are evenly distributed throughout the cross-section with no phase separation or non-stoichiometric area. For comparison, elemental mapping was performed on the un-irradiated bulk section of the sample too; see Figure 2.5. The atomic ratios of

lanthanum-to-zirconium-to-oxygen were found to be quite similar on the surface as well as in the bulk of the pellet and very close to the values expected in stoichiometric material (see Table 2-3). This indicates that even though the laser-annealing turns tetragonal LLZO to cubic phase, the composition of the material does not change.

2.4.2 Electrical properties

The room temperature AC conductivity results for the tetragonal and the laser-annealed cubic LLZO are shown in the complex impedance Nyquist plots in Figure 2.6. The solid lines in Figure 2.6 represent fitted data based on an equivalent circuit model of $(R_{total}Q_{total})R_{el}$, where R_{total} is the total resistance, Q_{total} is the total constant phase element, and R_{el} is the resistance of the electrolyte, respectively [6, 19]. Both of the impedance spectra show a semicircle in the high frequency range which gives the total ionic resistance. The total ionic conductivity of the tetragonal LLZO is $1.8x10^{-7}$ S/cm which is comparable to the reported total ionic conductivity for the pure tetragonal LLZO[21]. The total ionic conductivity of the laser annealed cubic LLZO is $1.6x10^{-5}$ S/cm which is about two orders of magnitude higher than that for the tetragonal LLZO. However, still the total ionic conductivity of the laser annealed cubic LLZO is lower than the values reported by Shimonishi et al. and Murugan et al. [3, 7]. The low ionic conductivity for the laser annealed cubic LLZO was attributed to the fine grain structure of the material which results in a low density of 4.55 g/cm^3 compared to the theoretical value of 5.098 g/cm^3 [4].

In general, the solid state ionic conductivity has a close relationship with grain size; the material with large grains and fewer grain boundaries usually has higher conductivity. To improve the ionic conductivity of the laser annealed LLZO, a follow-

up experiment was conducted with higher laser pulse energies. It was observed that when laser energy is increased, grain starts to grow (see Figure 2.7). The average grain size was found to increase from 4μm for 125mJ/cm^2 to 8μm for 600mJ/cm^2. On further increasing the laser pulse energy to 700mJ/cm^2, slight melting at the grain boundaries occurred which enhanced the connectivity between the grains. Figure 2.8 shows EIS data for high energy annealed LLZO sample. The total ionic conductivity of this sample was determined as 1.0×10^{-4} S/cm which is comparable to the highest ionic conductivity for the pure cubic LLZO reported by Murugan et al. [3].

2.5 Conclusion

Rechargable lithium ion batteries have emerged as the most prevalent medium for electricity storage in portable electronic devices due to their light weight, flexibility, and high energy density. These batteries are also considered very useful for their potential application in next-generation hybrid electric vehicles. However, a major drawback that plagues the application of these batteries is their flamability, specifically that of liquid electrolytes. To overcome the aforementioned shortcoming, an extensive amount of research has been performed to develop high ionic-conductivity solid state electrolytes. A wide spectrum of electrolyte materials reviewed here demonstrates that LLZO garnets are the most favorable electrolyte materials for designing solid state lithium ion batteries, both due to their high ionic conductivities and overall compatibilities with current LIBs, specifically Li metal. LLZO exists in two crystallographic phases, cubic as well as tetragonal. The cubic phase of LLZO exhibits higher ionic conductivity compared to tetragonal phase. However, the synthesis of cubic LLZO requires sinterring at very high temperatures which results in lithium deficiencies

and also limits its application. A way to overcome this problem is by doping LLZO with extrinsic dopants such as Al or Ga which lower the sintering temperature required to achieve cubic phase. However, the reduction in sinterring temperature comes with a new problem of secondary phase precipitation which can hinder the ion transport in the material. In the present study, we are reporting a pulsed laser annealing process of converting tetragonal LLZO to cubic LLZO at room temperature without any extrinsic dopants. The room temperature ionic conductivity for the laser annealed cubic LLZO yields a three orders of magnitude improvement over the tetragonal LLZO.

2.6 References

[1] J. B. Goodenough, K.-S. Park, The Li-ion rechargeable battery: A perspective,J. Am. Chem. Soc. 2013;135:1167-1176.

[2] C. de las Casas, W. Li, A review of application of carbon nanotubes for lithium ion battery anode material,Journal of Power Sources 2012;208:74-85.

[3] R. Murugan, V. Thangadurai, W. Weppner, Fast lithium ion conduction in garnet-type $Li_7La_3Zr_2O_{12}$,Angew. Chem. Int. Ed. 2007;46:7778-7781.

[4] J. Awaka, N. Kijima, H. Hayakawa, J. Akimoto, Synthesis and structure analysis of tetragonal $Li_7La_3Zr_2O_{12}$ with the garnet-related type structure,J. Solid State Chem. 2009;182:2046-2052.

[5] K. Masashi, M. Hirokazu, K. Kiyoshi, S. Yosuke, Y. Toshihiro, Compatibility of $Li_7La_3Zr_2O_{12}$ solid electrolyte to all solid state battery using Li metal anode,J. Electrochem. Soc. 2010;157:A1076-A1079.

[6] I. Kokal, M. Somer, P. H. L. Notten, H. T. Hintzen, Sol–gel synthesis and lithium ion conductivity of $Li_7La_3Zr_2O_{12}$ with garnet-related type structure,Solid State Ionics 2011;185:42-46.

[7] Y. Shimonishi, A. Toda, T. Zhang, A. Hirano, N. Imanishi, O. Yamamoto, Y. Takeda, Synthesis of garnet-type $Li_{7-x}La_3Zr_2O_{12-x}$ and its stability in aqueous solutions,Solid State Ionics 2011;183:48-53.

[8] H. Buschmann, J. Dolle, S. Berendts, A. Kuhn, P. Bottke, M. Wilkening, P. Heitjans, A. Senyshyn, H. Ehrenberg, A. Lotnyk, Structure and dynamics of the fast lithium ion conductor" $Li_7La_3Zr_2O_{12}$",PCCP 2011;13:19378-19392.

[9] E. Rangasamy, J. Wolfenstine, J. Sakamoto, The role of Al and Li concentration on the formation of cubic garnet solid electrolyte of nominal composition $Li_7La_3Zr_2O_{12}$,Solid State Ionics 2012;206:28-32.

[10] Y. Jin, P. J. McGinn, Al-doped $Li_7La_3Zr_2O_{12}$ synthesized by a polymerized complex method,J. Power Sources 2011;196:8683-8687.

[11] A. Düvel, A. Kuhn, L. Robben, M. Wilkening, P. Heitjans, Mechanosynthesis of solid electrolytes: preparation, characterization, and Li ion transport properties of garnet-type Al-doped $Li_7La_3Zr_2O_{12}$ crystallizing with cubic symmetry,J. Phys. Chem. C 2012;116:15192-15202.

[12] J. Wolfenstine, J. Sakamoto, J. Allen, Electron microscopy characterization of hot-pressed Al substituted $Li_7La_3Zr_2O_{12}$,J. Mater. Sci. 2012;47:4428-4431.

[13] C. A. Geiger, E. Alekseev, B. Lazic, M. Fisch, T. Armbruster, R. Langner, M. Fechtelkord, N. Kim, T. Pettke, W. Weppner, Crystal chemistry and stability of "$Li_7La_3Zr_2O_{12}$" garnet: a fast lithium-ion conductor,Inorg. Chem. 2010;50:1089-1097.

[14] H. El Shinawi, J. Janek, Stabilization of cubic lithium-stuffed garnets of the type "$Li_7La_3Zr_2O_{12}$" by addition of gallium,J. Power Sources 2013;225:13-19.

[15] J. Wolfenstine, J. Ratchford, E. Rangasamy, J. Sakamoto, J. L. Allen, Synthesis and high Li-ion conductivity of Ga-stabilized cubic $Li_7La_3Zr_2O_{12}$,Mater. Chem. Phys. 2012;134:571-575.

[16] H. Buschmann, S. Berendts, B. Mogwitz, J. Janek, Lithium metal electrode kinetics and ionic conductivity of the solid lithium ion conductors "$Li_7La_3Zr_2O_{12}$" and $Li_{[7-x]}La_{[3]}Zr_{[2-x]}Ta_{[x]}O_{[12]}$ with garnet-type structure,J. Power Sources 2012;206:236-244.

[17] J. L. Allen, J. Wolfenstine, E. Rangasamy, J. Sakamoto, Effect of substitution (Ta, Al, Ga) on the conductivity of $Li_7La_3Zr_2O_{12}$,J. Power Sources 2012;206:315-319.

[18] J. Narayan, J. Fletcher, C. W. White, W. H. Christie, Melting phenomena and pulsed laser annealing in semiconductors,J. Appl. Phys. 1981;52:7121-7128.

[19] T. Jiajia, T. Ashutosh, Synthesis of cubic phase $Li_7La_3Zr_2O_{12}$ electrolyte for solid state lithium ion batteries,Electrochem. Solid State Lett. 2012;15:A37-A39.

[20] J. Wolfenstine, E. Rangasamy, J. L. Allen, J. Sakamoto, High conductivity of dense tetragonal $Li_7La_3Zr_2O_{12}$,J. Power Sources 2012;208:193-196.

[21] Y. Shimonishi, A. Toda, T. Zhang, A. Hirano, N. Imanishi, O. Yamamoto, Y. Takeda, Synthesis of garnet-type $Li_{7-x}La_3Zr_2O_{12-1/2x}$ and its stability in aqueous solutions,Solid State Ionics 2011;183:48-53.

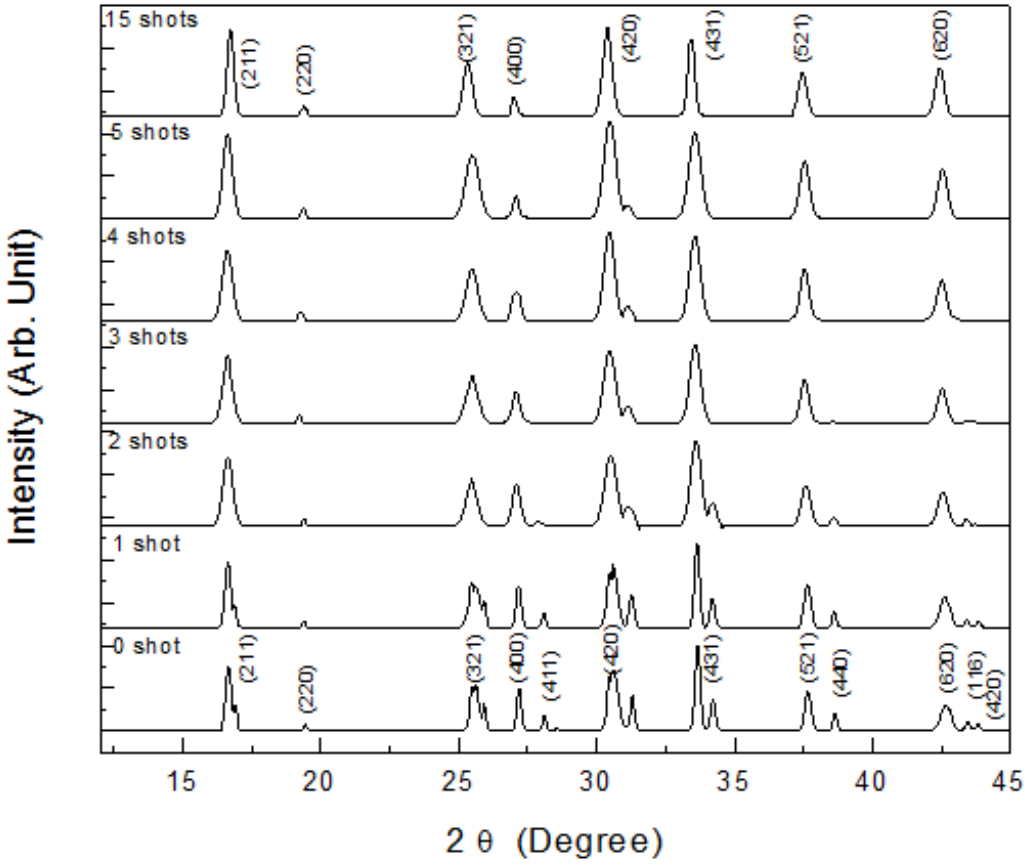

Figure 2.1. XRD patterns of LLZO as a function of number of laser shots with annealing fluence of 125 mJ/cm^2 per shot.

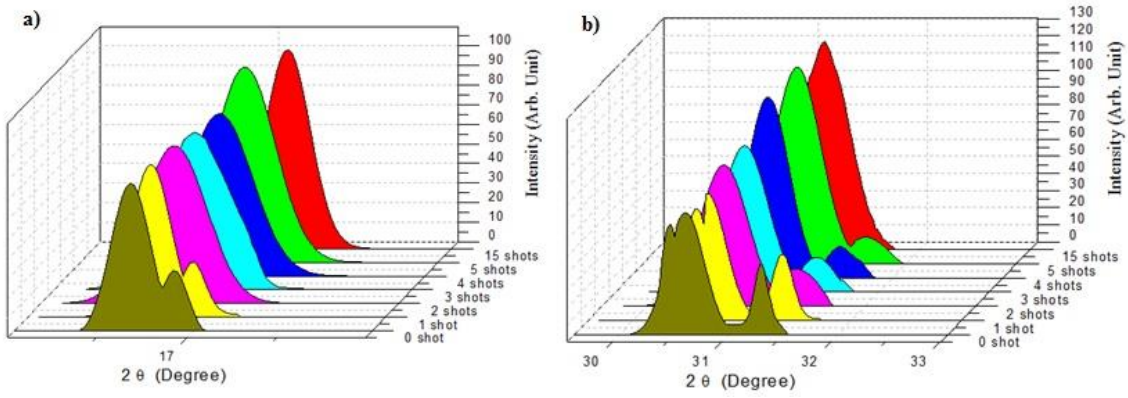

Figure 2.2. XRD patterns of LLZO as the function of number laser shots for: a) (211) peaks at $2\theta=16.7^{o}$, b) (420) peaks at $2\theta=30.5^{o}$.

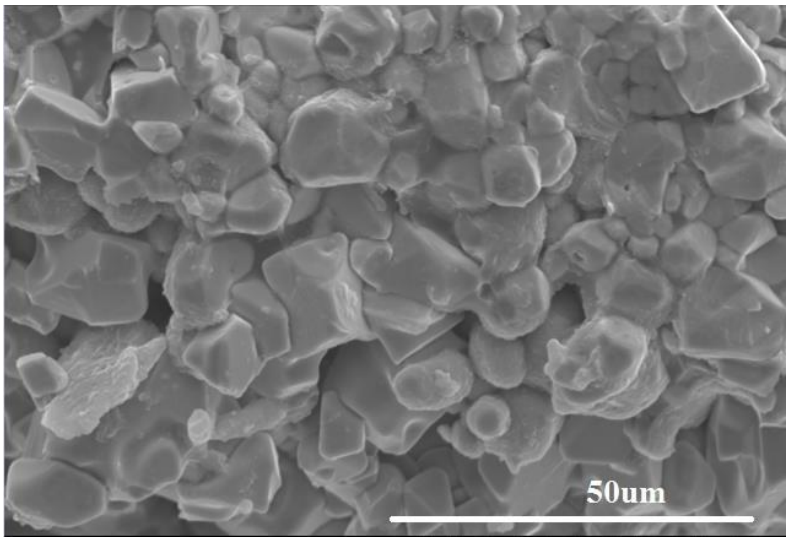

Figure 2.3. A cross-sectional SEM image of the 15 laser shots at 125mJ/cm^2 laser annealed LLZO sample (annealed surface at bottom).

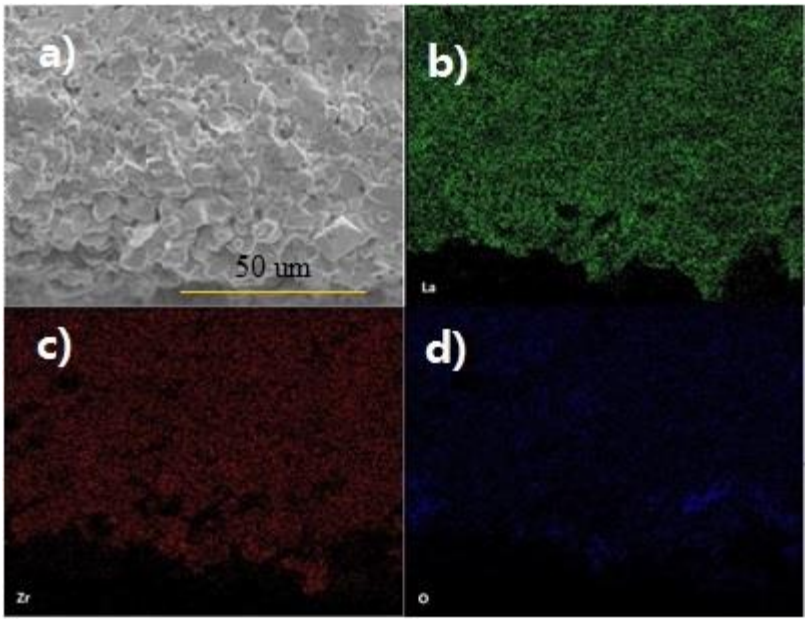

Figure 2.4. Elemental mapping of lanthanum, zirconium, and oxygen on the laser annealed LLZO pellet.

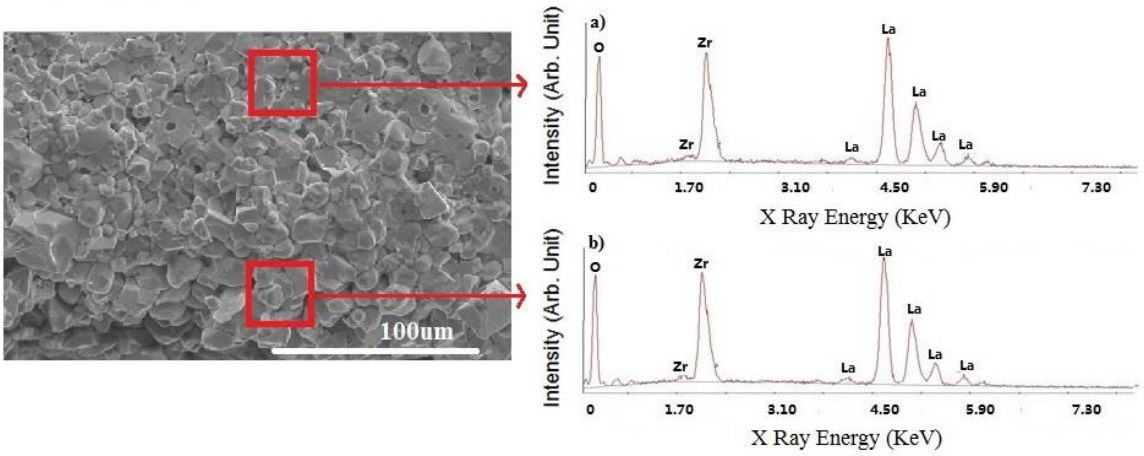

Figure 2.5. EDS spectrums of laser annealed LLZO at: a) bulk, b) laser annealed surface.

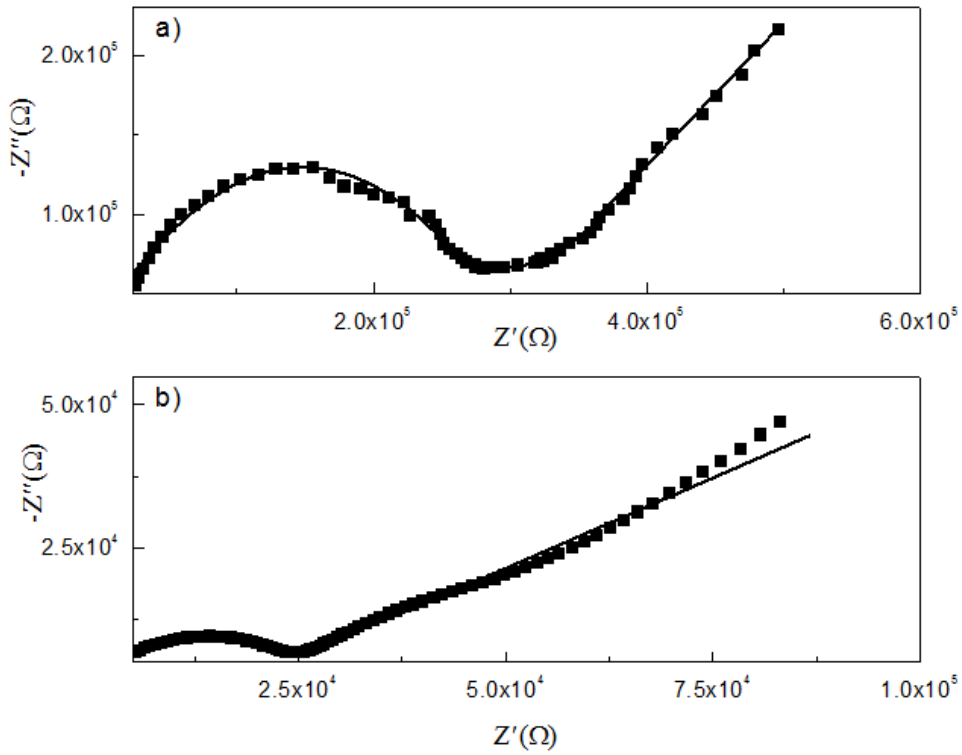

Figure 2.6. Nyquist plots of the AC impedance spectra for: a) the tetragonal LLZO, b) the laser annealed cubic LLZO.

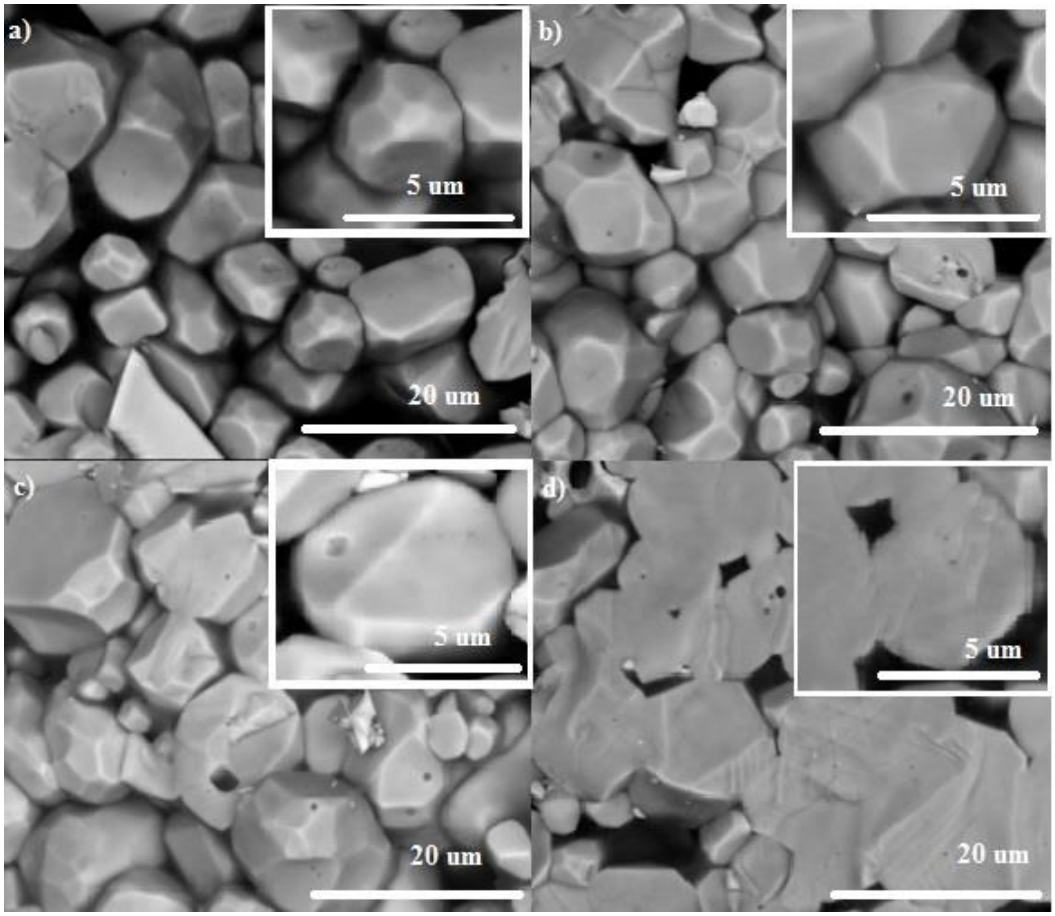

Figure 2.7. The cross-sectional SEM images of the one laser shot at: a) 125mJ/cm^2, b) 500mJ/cm^2 , c) 600mJ/cm^2, d) 700mJ/cm^2 laser annealed LLZO sample.

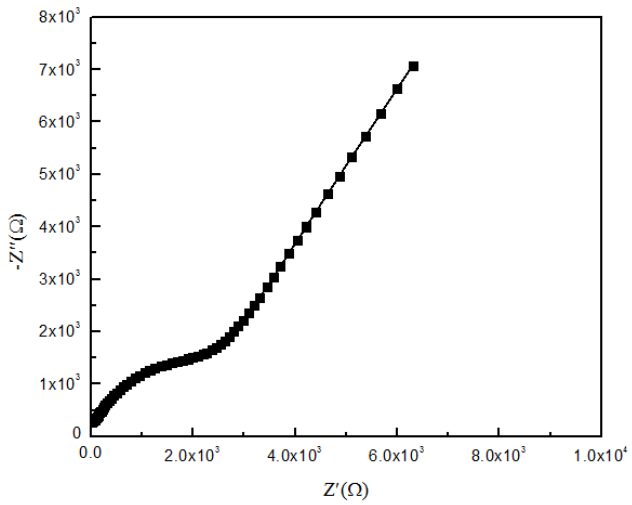

Figure 2.8. Nyquist plots of the AC impedance spectra for the laser annealed cubic LLZO with large grain.

Table 2.1 Methods for synthesizing LLZO

Synthesis Method	Excess of Li added	Processing Temperature (K)	Phase formed	Ionic Conductivity (S/cm) at Room Temperature	Activation Energy (eV)
Solid State [3]	N/A	1503K for 36 hours	Cubic	$3x10^{-4}$	0.3
Solid State [4]	10 %	1253 K for 5 hours	Tetragonal	$1.6x10^{-6}$	0.54
Solid State [5]	10 %	1503 K for 36 hours	Cubic	$1.8x10^{-4}$	N/A
Sol Gel [6]	N/A	1346K for 5hours	Tetragonal	$3.1x10^{-7}$	0.67
Sol Gel [7]	10 %	1453 K for 36hours	Cubic	$5.6x10^{-4}$	0.80
Sol Gel [7]	10 %	1273 K for 20 hours	Tetragonal	$4.4x10^{-7}$	0.54

Table 2.2 A list of experimental results for Al doped LLZO

Amount of Al Doped in Process	Processing Temperature (K)	Phase formed	Ionic Conductivity (S/cm) at Room Temperature	Activation Energy (eV)
0.9% [8]	1403 K for 12 hours	Cubic	$3x10^{-4}$	0.34
1% [9]	1273K for 4hours	Cubic	$4x10^{-4}$	0.26
1.2% [10]	1373K for 6 hours	Cubic	$2x10^{-4}$	N/A
1.78 % [11]	1500K for 15 hours	Cubic	$1x10^{-4}$	0.33

Table 2.3 Elemental ratio for the laser annealed surface and bulk of the LLZO sample

	Annealed Surface (I)			Bulk (II)		
	La	Zr	O	La	Zr	O
Atomic %	16.0%	12.51%	71.49%	17.71%	11.12%	71.17%
Integration Error	1.84	1.24	1.91	1.06	3.77	1.59
Peak/Background	11.55	11.97	3.21	16.32	3.78	16.32

CHAPTER 3

LOW TEMPERATURE SYNTHESIS OF $Li_5La_3Nb_2O_{12}$ [2]

3.1 Abstract

The lithium solid state electrolyte (SSE) of $Li_5La_3Nb_2O_{12}$ (LLNO) was synthesized via a novel molten salt synthesis (MSS) method at the relatively low temperature of 900°C. The low sintering temperature prevented the loss of lithium which commonly occurs during synthesis of the SSE using conventional solid state or wet chemical reactions. Recent publications have demonstrated that preserving the Li content is critical in improving the ionic conductivity of SSEs. The LLNO in this experiment showed a high Li-ion conductivity which is comparable to the values reported for LLNO. X-ray diffraction (XRD) measurements confirmed the formation of the cubic garnet Ia-3d crystal structure. In addition, the morphology was examined by scanning electron microscope (SEM), which showed a uniform grain size and crack free microstructure. These results demonstrate that the MSS is a powerful synthesis method to fabricate LLNO at a relatively low temperature while still achieving a high quality material.

[2] This chapter is based on the paper entitled "Novel low temperature molten salt synthesis of a $Li_5La_3Nb_2O_{12}$ solid state electrolyte and its properties," submitted to the Materials Research Society conference proceeding (2014).

3.2 Introduction

Today's huge demand for high-efficiency and carbon-free energy storage has motivated research on Li ion secondary batteries with high energy density and power density. Current Li ion batteries employ organic liquid polymers as the electrolyte materials, but these have some disadvantages, i.e., fire hazard and limited environmental compatibility. It is expected that all solid state lithium batteries, consisting of solid electrodes and solid electrolytes, will be able to overcome the safety problems of current lithium ion batteries [1]. Among all of the solid state electrolytes, garnet structured compounds such as $Li_7La_2Zr_3O_{12}$ (LLZO) and $Li_5La_2Nb_3O_{12}$ (LLNO) have attracted much attention because of their cubic structure (space group Ia-3d) and high Li ion conductivity (above 10^{-6} S/cm) [1-4]. However, it has been reported that LLZO has stability issues when exposed to moisture; this has made LLNO the best candidate for a stable and high performance Li ion battery solid state electrolyte [5].

The good chemical stability and high ionic conductivity of LLNO are attributed to its garnet cubic structure. In the garnet cubic LLNO solid electrolyte, 1/3 of the Li cations occupy octahedral sites and the remaining 2/3 of the Li cations reside in tetrahedral sites [6, 7]. It has been suggested that the Li mobility is dominated by the Li ions in octahedral sites, and it has been shown that an increased number of Li octahedra leads to increase in the ionic conductivity [6, 8, 9]. Several studies have also reported that introducing large extrinsic impurities, such as In and K, into LLNO during processing can open the ion transport pathways and further increase the ionic conductivity [10, 11].

However, the general process to fabricate LLNO is usually either via a solid state reaction or sol-gel process [10-13]. These processes require the LLNO to be sintered at

high temperatures (above 1100^{o}C) for long periods of time (above 24 hours) in order to achieve high Li ion conductivity [3, 8, 10, 11]. The high sintering temperature and long sintering time can cause the Li to evaporate during the process. A Li deficiency in LLNO can significantly reduce its ionic conductivity. In this paper, we demonstrate the use of a novel, molten salt synthesis (MSS) method to fabricate garnet cubic LLNO with high Li ion conductivity.

3.3 Experimental procedure

$Li_5La_3Nb_2O_{12}$ was prepared by mixing stoichiometric amounts of Li_2O (Alfa-Aeser 99.5%), La_2O_3 (Alfa-Aeser 99.9%), and Nb_2O_5 (Alfa-Aeser 99.9%) to obtain a total precursor powder weight of 5g. In order to melt the mixture at the eutectic temperature, 20g of Li_2CO_3 (Alfa Aeser 99.9%) was added to act as the molten salt. Since the eutectic temperature of Li_2O and Li_2CO_3 is 705^{o}C [14], as seen in Figure 3.1, the mixed powders were heat-treated at 700^{o}C, 800^{o}C, and 900^{o}C for 6 hours to result in crystal formation. Next, the samples were placed into a 1M HCl aqueous solution to dissolve the Li_2CO_3. The solution was then filtered and dried at room temperature. X-ray diffraction experiments were carried out to characterize the phase formation of the samples with a Philips X'PERT X-ray Diffractometer using Cu Kα radiation. The measurements were performed from $2\theta=10^{o}$ to 90^{o} with a step size of 0.02^{o}. Analysis of powder diffraction patterns was carried out using the Rietveld analysis technique**.**

The resultant powders were ground and pressed into ½" pellets using a uniaxial press. Subsequently, the pellets were sintered at 1000^{o}C, 1100^{o}C, and 1200^{o}C for 3 hours, in order to have the grain growth necessary to achieve high ionic conductivity. The grain growth of the samples was examined on the cross-section surfaces using

scanning electron microscopy (SEM) (Hitachi S-3000N). Au was sputter coated on the top and bottom surfaces of the pellet to serve as Li ion blocking electrodes for ionic conductivity measurements which were performed by using a Gamry Reference 600^{TM} Instrument over the frequency range of 10^6 to 0.1 Hz.

3.4 Results and discussion

3.4.1 Crystal structure

The XRD patterns after sintering the precursor powder at 700^{o}C, 800^{o}C, and 900^{o}C for 6 hours are shown in Figure 3.2. The patterns were then indexed according to the LLNO garnet cubic structure (JCPDS 00-045-0109). The diffraction pattern of the precursor powder sintered at 700^{o}C contained a mixture of LLNO, $La_2Zr_2O_7$ (JCPDS 00-017-0450), Li_2O (JCPDS 01-074-6256), La_2O_3 (JCPDS 00-022-0641), and Nb_2O_5 (JCPDS 00-005-0352). It is clear that 700^{o}C could only transform part of the precursory powder into LLNO. The diffraction pattern of the powder sintered at 800^{o}C has characteristic peaks for garnet cubic structure with a peak shouldering at $2\theta = 31.5^o$ indicating that a nonperfect structure was formed. On the other hand, the XRD of the precursor powder sintered at 900^{o}C matches very well with the garnet cubic structure of LLNO. This result suggested that the lowest MSS temperature to form the proper garnet structure is at 900^{o}C.

3.4.2 Morphology

The crystallized LLNO powders (sintered at 900^{o}C) were pressed into ½" pellets and heat-treated at different temperatures to have grain growth. The SEM images for the pellets sintered are shown in Figure 3.3. Attempts to have grain growth by increasing

the sintering temperature were successful. Increasing the sintering temperature from 1000^{o}C to 1200^{o}C led to the average grain size growing from 20 μm to 60 μm. This result suggested that although the MSS was able to synthesize LLNO at lower temperature, higher temperature annealing is still required to have a proper grain growth. However, the overall sintering time for the proper grain growth is only 3 hours which is much shorter than the reported 24 hours.

3.4.3 Electrochemical properties

The impedance plots for the Au plated LLNO pellets are shown in Figure 3.4. All impedance spectra have a distorted semicircle in the high frequency regime and a tail in the low frequency regime. The distorted semicircle revealed the effects of the total ionic conductivity (bulk + grain boundary) and the tail was contributed by the diffusion of the mobile Li ion.

The overall behavior of the impedance spectra was fit with an equivalence circuit of $(R_{total}Q_{total})R_{el}$, where R_{total} is the total resistance, Q_{total} is the total constant phase element, and R_{el} is the resistance of the electrolyte, respectively. The determined ionic conductivities for the annealed pellets are presented on top of the impedance spectra. It is observed that the ionic conductivity increased one order of magnitude from $1.3x10^{-6}$ to $1.5x10^{-5}$ S/cm when the sintering temperature increased from 1000^{o}C to 1100^{o}C. While the sintering temperature was further increased to 1200^{o}C, the ionic conductivity has a smaller increment to $2.5x10^{-5}$ S/cm which is higher than the highest ionic conductivity ($1.0x10^{-5}$ S/cm) reported in literature for LLNO [12].

3.5 Conclusion

We have shown that it is possible to fabricate LLNO solid state electrolyte by using MSS at relatively low temperatures. The XRD data showed the garnet cubic LLNO was formed at 900^{o}C. However, in order for the garnet cubic LLNO to obtain high ionic conductivity, further sintering to have grain growth is necessary. The Li ion conductivity was found to be increased with increasing sintering temperature and the grain growth was evidenced by SEM images. Among the investigated sintering temperature, both the LLNO sintered at 1100^{o}C and 1200^{o}C have high ionic conductivity of $1.5x10^{-5}$ and $2.5x10^{-5}$ S/cm, respectively, which are better than the highest value previously reported for LLNO electrolytes.

3.6 References

[1] Teng S., Tan J., Tiwari A., Recent developments in garnet based solid state electrolytes for thin film batteries, Curr. Opin. Solid State Mater. Sci. 2014;18:29-38.

[2] Kokal I., Somer M., Notten P., Hintzen H., Sol–gel synthesis and lithium ion conductivity of Li7La3Zr2O12 with garnet-related type structure, Solid State Ionics 2011;185:42-46.

[3] Koch B., Vogel M., Lithium ionic jump motion in the fast solid ion conductor Li5La3Nb2O12, Solid State Nucl. Magn. Reson. 2008;34:37-43.

[4] Thangadurai V., Kaack H., Weppner W. J., Novel Fast Lithium Ion Conduction in Garnet-Type Li5La3M2O12 (M= Nb, Ta), J. Am. Ceram. Soc. 2003;86:437-440.

[5] Jin Y., McGinn P. J., Li7La3Zr2O12 electrolyte stability in air and fabrication of a Li/Li7La3Zr2O12Cu0.1V2O5solid state battery, J. Power Sources 2013;239:326-331.

[6] van Wüllen L., Echelmeyer T., Meyer H. W., Wilmer D., The mechanism of Li-ion transport in the garnet Li5La3Nb2O12, PCCP 2007;9:3298-3303.

[7] Thangadurai V., Adams S., Weppner W., Crystal structure revision and identification of Li+-ion migration pathways in the garnet-like Li5La3M2O12 (M= Nb, Ta) oxides, Chem. Mater. 2004;16:2998-3006.

[8] Nyman M., Alam T. M., McIntyre S. K., Bleier G. C., Ingersoll D., Alternative Approach to Increasing Li Mobility in Li-La-Nb/Ta Garnet Electrolytes, Chem. Mater. 2010;22:5401-5410.

[9] Narayanan S., Thangadurai V., Fast Lithium-Ion Conducting Garnet-Like Electrolytes for Potential Application in Lithium Ion Batteries, ECS Transactions 2011;35:125-131.

[10] Narayanan S., Ramezanipour F., Thangadurai V., Enhancing Li Ion Conductivity of Garnet-Type Li5La3Nb2O12 by Y-and Li-Codoping: Synthesis, Structure, Chemical Stability, and Transport Properties, J. Phys. Chem. C 2012;116:20154-20162.

[11] Thangadurai V., Weppner W., Effect of sintering on the ionic conductivity of garnet-related structure Li5La3Nb2O12 and In-and K-doped Li5La3Nb2O12, J. Solid State Chem. 2006;179:974-984.

[12] Peng H., Wu Q., Xiao L., Low temperature synthesis of Li5La3Nb2O12 with cubic garnet-type structure by sol–gel process, J. Sol-Gel Sci. Technol. 2013;66:175-179.

[13] WANG W.G., FANG Q.-f., GAO Y.-x., HAO G.-l., MA W.-q., LI W.-d., The Investigation of Lithium Ion Diffusion in Li_5La_3Nb_2O_ (12) under Different Sintering Conditions, Science Technology and Engineering 2011;21:017.

[14] Huang W. D., Hsu L. C., Wang J., Ativanichayaphong T., Deb S., Chiao M., Chiao J., Investigation of repeatability of sol-gel iridium oxide pH sensor on flexible substrate, Smart Materials 2008:726916-726916-9.

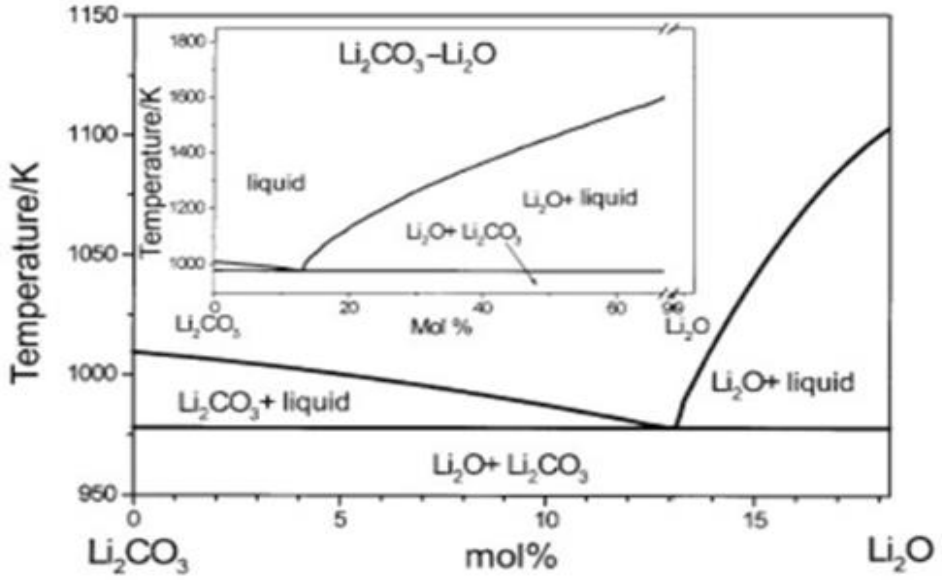

Figure 3.1. Li_2O and Li_2CO_3 phase diagram. Reprint with permission from [14].

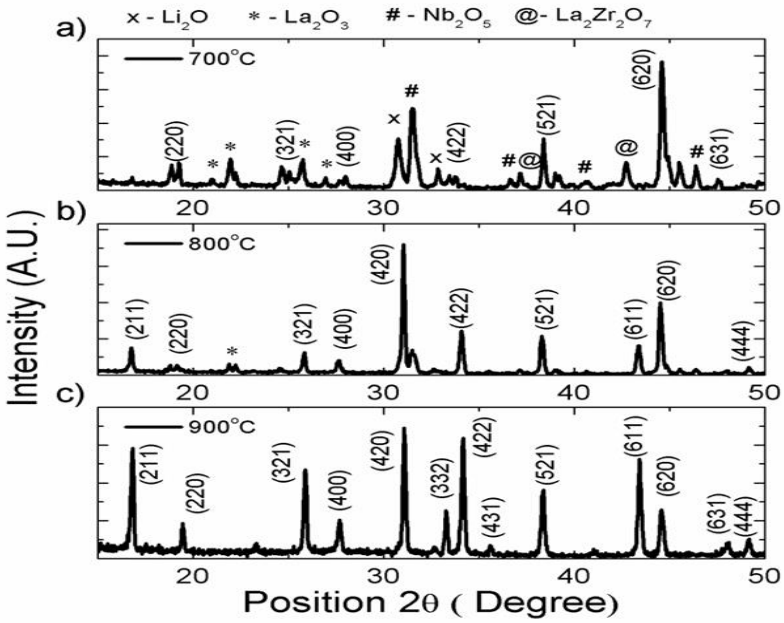

Figure 3.2 The XRD results for powder sintered at a) 700°C, b) 800°C, and c) 900°C for 6 hours.

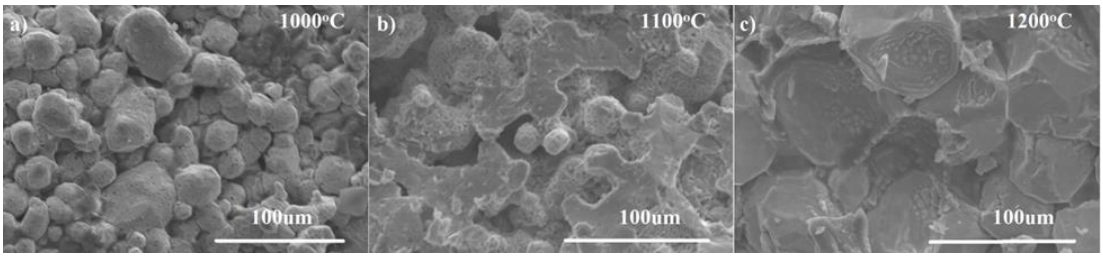

Figure 3.3. SEM images for pellets sintered at a) 1000^{o}C, b) 1100^{o}C, and c) 1200^{o}C.

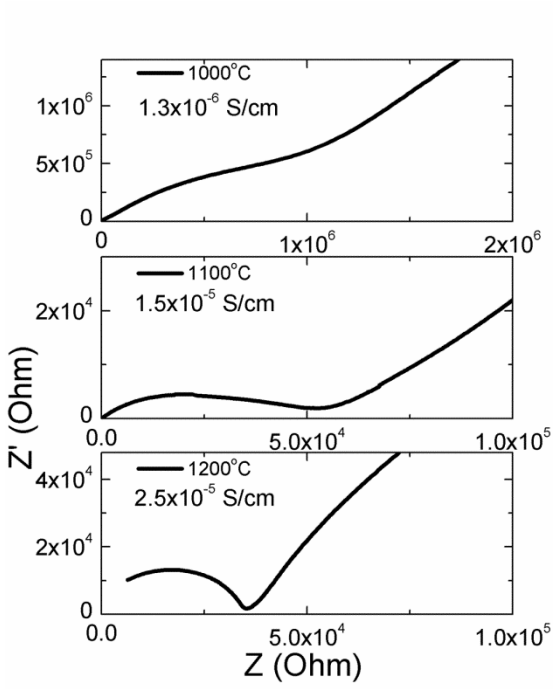

Figure 3.4. EIS spectra and ionic conductivities for pellets sintered at a) 1000^{o}C, b) 1100^{o}C, and c) 1200^{o}C.

CHAPTER 4

WOOD ELECTRODES FOR SUPERCAPACITORS [3]

4.1 Abstract

Three-dimensional network structures with interconnected microchannels were formed through the carbonization of three different varieties of wood. Retention of the original wood's structure was confirmed using SEM. Performance of these carbonized wood structures was tested for their application as supercapacitor electrodes. From charge-discharge cycling in a KOH electrolyte solution, a maximum energy density of ~45.6 Wh/kg (discharge current of 200 mA/g) and a maximum power density of ~2000 W/kg (discharge current of 4000 mA/g) were obtained. At the highest charge-discharge current density (4000 mA/g), the sandalwood retained the highest energy density with a value of 14.5 Wh/kg. The carbonized wood electrodes exhibited excellent cyclability, with 99.7% of the specific capacitance being retained after 2000 cycles. These remarkable results demonstrate the exciting commercial potential for carbonized wood-based materials as inexpensive, high performance supercapacitor electrodes.

[3] This chapter is based on the paper entitled "Carbonized Wood for Supercapacitor Electrodes," published in Solid State Letters 3 (5), p. M25-M28 (2014). Reprint with permission.

4.2 Introduction

Research on novel energy storage devices such as high capacitance batteries and supercapacitors has attracted significant attention in recent years [1, 2]. Traditional batteries have a low power density (i.e., slow charge-discharge rates) and a high energy density, whereas conventional dielectric capacitors possess a high power density but lack a large energy density. It is necessary to develop systems which can simultaneously provide high energy density as well as high power density [1]. The electrochemical supercapacitor is considered a potential candidate for such a system due to its high power density and reasonably good energy densities [3, 4]. Currently, research in supercapacitors is focused on increasing their energy densities further and lowering their overall production costs by finding suitable electrode materials [5, 6].

Among various supercapacitor systems investigated so far, carbon-based supercapacitors have been shown to have many advantages over other commonly used materials. This is due to their environmental friendliness, low cost, large capacitance, and large cycle stability [4, 5]. Porous carbon-based materials were the first to be explored for their application in supercapacitors. However, in spite of its large surface area which results in high specific capacitance, porous carbon's low electrical conductivity has limited its use in supercapacitors [3, 7]. Carbon nanotubes (CNTs)-based electrodes were proposed to overcome the above limitation because of CNT's large electrical conductivity [8]. Despite this advantage, the use of CNTs in supercapacitors has been limited due to the presence of a high contact resistance between the supercapacitor electrode and current collector [3]. Activated carbon has also been explored for making supercapacitor electrodes due to its interconnected, microporous structure which yields a large surface area. However, even though

activated carbon possesses a large surface area, a large portion of the pores are nanopores (diameter < 2nm) and as such are not fully accessible to electrolyte ions [5, 9].

Graphene-based supercapacitors have also attracted significant attention recently because of their high reported specific capacitance of 205 F/g in aqueous KOH [10]. However, their use in superconductors is limited due to the lack of process control during synthesis which can result in graphene layers aggregating together and even stacking on top of one another due to van der Waals interactions [11-14].

Wood is an abundant, environmentally friendly material which can be carbonized at high temperatures under a nitrogen atmosphere to preserve its interconnected, multichannel porous structure. This interconnected, multichannel structure supplies a large surface area for ion contact. Wood's microporous channels have diameters ranging from tens of nanometers to hundreds of micrometers [15, 16]. The larger pores are large enough that electrolyte ions can easily commute in the channels, facilitating the formation of the electrical double layer (EDL) [17]. For nanopores, however, pore curvature must be accounted for, resulting in charge accumulation in the center of the pore [17]. However, it is expected that nanopores have little contribution to specific capacitance at high current densities because the pores are not fully accessible to the electrolyte ions [5, 9]. In order to fully understand the effect of pore size on capacitance, we have carbonized three different types of wood, each with different ratios of various sized pores, and fabricated supercapacitor devices using these pieces of carbonized wood as electrode materials. A thorough investigation of their performance is detailed in the following sections.

4.3 Experimental procedure

The carbonized wood electrodes were synthesized from three different types of wood, namely beech wood, pine wood, and sandalwood. These woods were selected as they provide a wide variety of multichannel microstructures, with varying ratios of different micron sized channels. In the initial preparations, the wood pieces were boiled in 1M ammonia solution for 5 hours to remove the resin and any impurities. The boiled samples were then transferred to a box furnace for dehydration at 120^{o}C for 3 hours, after which they were carbonized by heating under N_2 at 800^{o}C for 2 hours.

Scanning electron microscopy (SEM) measurements were carried out using an FEI Quanta 600F SEM. Bulk samples were cut in half along the axis in order to examine cross-sections; axial images were taken from the top surface of bulk samples. Images were taken at varying magnifications in both the axial and radial directions in order to effectively compare the ratio of different pore sizes in each type of wood.

The internal surface area of the samples was measured from N_2 absorption/desorption at 77K via the Brunauer–Emmett–Teller (BET) method using a Gemini V Analyzer. Electrochemical and specific capacitance measurements of the supercapacitor electrodes were conducted in a three electrode system with the carbonized wood as the working electrode, platinum foil as the counter electrode, and Ag/AgCl as the reference electrode. The cyclic voltammetry (CV), galvanostatic charge-discharge, and electrochemical impedance spectroscopy (EIS) were tested using a Gamry Reference 600. The CV response of the electrodes was measured at scan rates varying from 2 mV/s to 200 mV/s. Galvanostatic charge-discharge testing was carried out at varying current densities between 0 and -1.0 V in a 2M KOH aqueous electrolyte

solution. Electrochemical impedance spectroscopy measurements were carried out over the frequency range from 200 kHz to 0.1 Hz.

4.4 Results and discussion

4.4.1 Morphological studies

The SEM images of the carbonized woods, in both the axial and radial directions, are shown in Figure 4.1. From these images, it is clear that the carbonization process preserved the three-dimensional, multichannel structures. The radial SEM images, as seen in Figure 4.1 (a,c,e), show that interconnected parallel channels exist for all the samples. The axial SEM images, Figure 4.1 (b,d,f), showed that the pore diameters range from about five micrometers to several hundred micrometers, depending on the type of wood used.

Beech wood has a large variety of pore sizes, with approximately 13% of the pores ranging from 50 to 100 μm in diameter with the rest of the pores in the range of 5 to 8 μm, as seen in Figure 4.1 b. Pine wood has a very uniform microstructure, with approximately 97% of the pores in the 10 μm range and only 3% of pores with ~80 μm diameters, as seen in Figure 4.1 d. The sandalwood has a porous structure with approximately 46% of the pore diameters in the 40 μm range with the remainder in the 5 μm range, as seen in Figure 4.1 f. Table 4-1 summarizes the specific surface area of the carbonized wood electrodes. Pine wood has the highest specific surface area of 76 m^2/g compared to 44 m^2/g and 38 m^2/g for the beech wood and sandalwood, respectively.

4.4.2 Electrochemical impedance spectroscopy

Electrochemical impedance spectroscopy (EIS) was used to examine the electrical properties of the carbonized wood. The impedance was measured over a frequency range from 200 kHz to 0.1 Hz. Figure 4-2a shows the Nyquist plots for the different electrodes. The imaginary component (Z') shows the capacitive properties whereas the real component (Z) shows the ohmic behavior of the samples. All the impedance spectra showed similar behavior, with an arc at the high frequency range and a linear response at lower frequencies. In the low frequency range, a completely vertical straight line indicates typical EDL capacitive behavior, in which the capacitance is almost independent of the applied AC frequency. In this range, the sandalwood sample approached a vertical limit, indicating the nearly ideal EDL behavior of the capacitance.

In general, the effectiveness of EDL formation in supercapacitors is strongly dependent on the equivalent series resistance (ESR) which is the total electrical resistance of the electrodes, the electrode/electrolyte interfaces, and the electrolyte. The ESR was obtained from the x-intercept of the Nyquist plots [18]. The magnitude of the ESR was measured as 4.6, 5.9, and 5.3 ohms for the beech, pine, and sandalwood, respectively.

4.4.3 Cyclic voltammetry

Figure 4.2 (b,c,d) shows cyclic voltammograms of the carbonized wood electrodes for various scan rates in the range of 2 mV/s to 200 mV/s. None of these curves show any signature of a redox reaction, suggesting the origin of the capacitance is the typical EDL formation. Furthermore, the lack of any reaction peak supports the claim that the arc seen in the EIS measurements (Figure 4.2a) is not caused by a reactive species. For

the beech wood and sandalwood, the CV curves with a scan rate of 2 mV/s show a nearly constant current within the voltage range measured, indicating that both of these samples exhibit ideal EDL capacitive behavior. In contrast, for the same scan rate, the CV curve for pine wood exhibits a distorted shape.

At high scan rates, the shape distortion was observed for all three wood samples, mainly due to the significant contribution of the ESR. In general, at low scan rates, the current, I, is small enough such that the I×ESR losses are negligible. However, as the scan rate is increased, I increases, and as such, the I×ESR losses become significant and result in the shape distortion. This distortion seen in the CV curves has also been observed in other porous electrode materials [18-21].

4.4.4 Galvanostatic charge-discharge

Galvanostatic charge-discharge measurements were performed in 2M KOH solution over a voltage range between -1 to 0 V with current densities of 200, 500, 1000, 2000, and 4000 mA/g. The charge-discharge cycle duration was found to decrease with increasing current density, as seen in Figure 4.3. The nearly linear voltage vs. time profile and the symmetric charge-discharge curves are indicative that reasonably high quality capacitive behavior has been achieved by the carbonized wood electrodes.

The specific capacitance, C_s, of the samples was calculated according to the following equation:

$$C_s = \frac{I}{(\Delta V/\Delta t)m} \tag{4.1}$$

where I is the constant discharge current, Δt is the discharge time, m is the mass of the material, and ΔV is the potential drop during discharge.

The specific capacitance values as a function of current density are shown in Figure 4.4. In addition to the obtained experimental results, various reported values for common electrodes are included [10, 14, 22-26]. It is clear that the specific capacitance decreases with increasing discharge current density. The calculated specific capacitance at 200 mA/g for the beech and pine wood are 282 and 328 F/g, respectively, values which are approximately 50% larger than those for graphene-based electrodes [10, 26]. At the same discharge current, the sandalwood was found to have a specific capacitance of 237 F/g which is 10% higher than the graphene-based electrodes [10, 26]. The higher specific capacitances of the beech and pine wood under low current densities can be explained by their high specific surface areas suggesting the total surface area, measured by BET (Table 4.1), contributes to the specific capacitance. When the current density is low, all of the surface area in the structure is accessible to the electrolyte ions.

The energy density and power density of supercapacitors can be calculated according to the following equations:

$$E = \frac{1}{2}CV^2 \tag{4.2}$$

$$P = \frac{E}{t} \tag{4.3}$$

where E is the energy density, C is the specific capacitance, V is the potential window, P is the power density and t is the discharge time.

The high energy densities, as seen in Figure 4.4, were obtained at a current density of 200 mA/g for the beech, pine and sandalwood, respectively, which are nearly equal to the energy density of lead acid batteries [2, 27]. The energy density decreases dramatically when the current density is increased from 200 mA/g to 500 mA/g, dropping by 27% and 39% for the beech and pine wood, respectively. Impressively, the sandalwood only suffered a 7% energy loss under the same conditions. With a high current density of 4000 mA/g, both the beech and pine wood have a very low energy density (specific capacitance) of 5.6 Wh/kg (40 F/g) and 6.1 Wh/kg (44 F/g) compared to 14.5 Wh/kg (104 F/g) for the sandalwood. It is clear that the sandalwood retains energy more effectively than the beech or pine wood as a function of increasing charge-discharge current density.

The high current density does not provide enough time for electrolyte ions to propagate into the channels and contact all surface areas. Therefore, only the larger micropores are able to store the charge, making the capacitance highly dependent on the number of large micropores in the electrode [28]. The larger capacitance for the sandalwood at the high current density of 4000 mA/g is attributed to its proportionally larger number of micropores in its structure.

Ragone plots are used to illustrate supercapacitor energy density as a function of power density. Figure 4.5a illustrates the overall Ragone plots of the three carbonized wood electrodes. The sandalwood sample exhibits the best performance, with a high energy density of 32.9 Wh/kg and a power density of 114 W/kg (at a low current density of 200 mA/g), and a high power density of 2001 W/kg with an energy density of 14.5 Wh/kg (at a high current density of 4000 mA/g). For comparison, at low current densities (200 mA/g), sandalwood's energy density is similar to conventional lead acid

batteries (32.9 Wh/kg vs. 40Wh/kg) and at high current densities (4000 mA/g), its power density is an order of magnitude higher (2001 W/kg vs. 180 W/kg) than lead acid batteries [2].

4.4.5 Cycle life

Cycle lifetime is a crucial parameter when considering supercapacitors for practical applications. The long-term stability of all the systems investigated in this study was evaluated by repeating galvanostatic charge-discharge tests for 2000 cycles. These tests were performed between -1 and 0V at the scan rate of 4000 mA/g. The energy density retention as a function of cycle number is shown in Figure 4.5b. After 2000 cycles, the energy densities only decreased by 0.3% of their initial values for all samples, thereby demonstrating that the carbonized wood-based electrodes have excellent cycle stability and a high reversibility in the repetitive charge-discharge cycling.

4.5 Conclusion

Three different carbonized woods, all with different pore size distributions, were used as electrode materials for supercapacitors. Unlike other carbon material electrodes, wood does not require special treatments or extra binding procedures during the electrode synthesis to be usable. Each of the wood electrodes has been shown to have a high specific capacitance, high energy density, ideal capacitor behavior, and excellent electrochemical stability (less than 0.3% capacitance loss after 2000 cycles). Both the beech and pine wood electrodes showed high energy densities of 39.2 and 45.6 Wh/kg, respectively, at a current density of 200 mA/g. However, when the current density was increased to 4000 mA/g, their energy densities dropped to about 14% of their values at

200 mA/g. The carbonized sandalwood sample showed slightly lower energy density (32.9 Wh/kg) at 200 mA/g, but it retained 44% of its energy density when the current density was increased to 4000 mA/g. Additionally, all three types of wood exhibited a power density of ~2000 Wh/kg at this high current density. At the highest discharge current density of 4000 mA/g, the sandalwood electrode's performance is comparable to lead acid batteries and has the added benefit of being much more environmentally friendly than lead acid batteries, too. The reason behind the sandalwood's excellent energy density retention at high discharge current densities is believed to be its unique microstructure. The exceptional performance of the wood-based supercapacitors detailed in this paper opens the possibility to engineer supercapacitor electrodes based on natural woods for a variety of applications.

4.6 References

[1] Liu X. M., Huang Z. d., Oh S. w., Zhang B., Ma P. C., Yuen M. M. F., Kim J. K., Carbon nanotube (CNT)-based composites as electrode material for rechargeable Li-ion batteries: A review, Compos. Sci. Technol. 2012;72:121-144.

[2] Verma P., Maire P., Novák P., A review of the features and analyses of the solid electrolyte interphase in Li-ion batteries, Electrochim. Acta 2010;55:6332-6341.

[3] SuongáOu F., Synthesis of hybrid nanowire arrays and their application as high power supercapacitor electrodes, Chem. Commun. 2008;20:2373-2375.

[4] Balducci A., Dugas R., Taberna P. L., Simon P., Plee D., Mastragostino M., Passerini S., High temperature carbon–carbon supercapacitor using ionic liquid as electrolyte, J. Power Sources 2007;165:922-927.

[5] Yan J., Wei T., Shao B., Ma F., Fan Z., Zhang M., Zheng C., Shang Y., Qian W., Wei F., Electrochemical properties of graphene nanosheet/carbon black composites as electrodes for supercapacitors, Carbon 2010;48:1731-1737.

[6] Wu F. C., Tseng R. L., Hu C. C., Wang C. C., Effects of pore structure and electrolyte on the capacitive characteristics of steam-and KOH-activated carbons for supercapacitors, J. Power Sources 2005;144:302-309.

[7] Snook G. A., Kao P., Best A. S., Conducting-polymer-based supercapacitor devices and electrodes, J. Power Sources 2011;196:1-12.

[8] An K. H., Jeon K. K., Heo J. K., Lim S. C., Bae D. J., Lee Y. H., High-capacitance supercapacitor using a nanocomposite electrode of single-walled carbon nanotube and polypyrrole, J. Electrochem. Soc. 2002;149:A1058-A1062.

[9] Fuertes A., Lota G., Centeno T., Frackowiak E., Templated mesoporous carbons for supercapacitor application, Electrochim. Acta 2005;50:2799-2805.

[10] Wang Y., Shi Z., Huang Y., Ma Y., Wang C., Chen M., Chen Y., Supercapacitor devices based on graphene materials, The Journal of Physical Chemistry C 2009;113:13103-13107.

[11] Li D., Mueller M. B., Gilje S., Kaner R. B., Wallace G. G., Processable aqueous dispersions of graphene nanosheets, Nature nanotechnology 2008;3:101-105.

[12] Stankovich S., Dikin D. A., Dommett G. H., Kohlhaas K. M., Zimney E. J., Stach E. A., Piner R. D., Nguyen S. T., Ruoff R. S., Graphene-based composite materials, Nature 2006;442:282-286.

[13] Yang H., Li F., Shan C., Han D., Zhang Q., Niu L., Ivaska A., Covalent functionalization of chemically converted graphene sheets via silane and its reinforcement, J. Mater. Chem. 2009;19:4632-4638.

[14] Cheng Q., Tang J., Ma J., Zhang H., Shinya N., Qin L. C., Graphene and carbon nanotube composite electrodes for supercapacitors with ultra-high energy density, PCCP 2011;13:17615-17624.

[15] Fujino T., Calderon-Moreno J. M., Swamy S., Hirose T., Yoshimura M., Phase and structural change of carbonized wood materials by hydrothermal treatment, Solid State Ionics 2002;151:197-203.

[16] Kurosaki F., Ishimaru K., Hata T., Bronsveld P., Kobayashi E., Imamura Y., Microstructure of wood charcoal prepared by flash heating, Carbon 2003;41:3057-3062.

[17] Huang J., Sumpter B. G., Meunier V., A universal model for nanoporous carbon supercapacitors applicable to diverse pore regimes, carbon materials, and electrolytes, Chemistry-A European Journal 2008;14:6614-6626.

[18] Liu C., Yu Z., Neff D., Zhamu A., Jang B. Z., Graphene-based supercapacitor with an ultrahigh energy density, Nano Lett. 2010;10:4863-4868.

[19] Pech D., Brunet M., Durou H., Huang P., Mochalin V., Gogotsi Y., Taberna P. L., Simon P., Ultrahigh-power micrometre-sized supercapacitors based on onion-like carbon, Nature nanotechnology 2010;5:651-654.

[20] Stoller M. D., Park S., Zhu Y., An J., Ruoff R. S., Graphene-based ultracapacitors, Nano Lett. 2008;8:3498-3502.

[21] Chen X. Y., Chen C., Zhang Z. J., Xie D. H., Deng X., Liu J. W., Nitrogen-doped porous carbon for supercapacitor with long-term electrochemical stability, J. Power Sources 2012;230.

[22] Garcia-Gomez A., Miles P., Centeno T., Rojo J., Uniaxially oriented carbon monoliths as supercapacitor electrodes, Electrochim. Acta 2010;55:8539-8544.

[23] Bichat M., Raymundo-Piñero E., Béguin F., High voltage supercapacitor built with seaweed carbons in neutral aqueous electrolyte, Carbon 2010;48:4351-4361.

[24] Yu C., Masarapu C., Rong J., Wei B., Jiang H., Stretchable Supercapacitors Based on Buckled Single-Walled Carbon-Nanotube Macrofilms, Adv. Mater. 2009;21:4793-4797.

[25] Lin L.-Y., Yeh M. H., Tsai J.-T., Huang Y. H., Sun C. L., Ho K. C., A novel core–shell multi-walled carbon nanotube@ graphene oxide nanoribbon heterostructure as a potential supercapacitor material, J. Mater. Chem. A 2013;1:11237-11245.

[26] Guo C. X., Li C. M., A self-assembled hierarchical nanostructure comprising carbon spheres and graphene nanosheets for enhanced supercapacitor performance, Energy & Environmental Science 2011;4:4504-4507.

[27] Zhu Y., Murali S., Stoller M. D., Ganesh K., Cai W., Ferreira P. J., Pirkle A., Wallace R. M., Cychosz K. A., Thommes M., Carbon-based supercapacitors produced by activation of graphene, Science 2011;332:1537-1541.

[28] Portet C., Taberna P. L., Simon P., Flahaut E., Laberty-Robert C., High power density electrodes for carbon supercapacitor applications, Electrochim. Acta 2005;50:4174-4181.

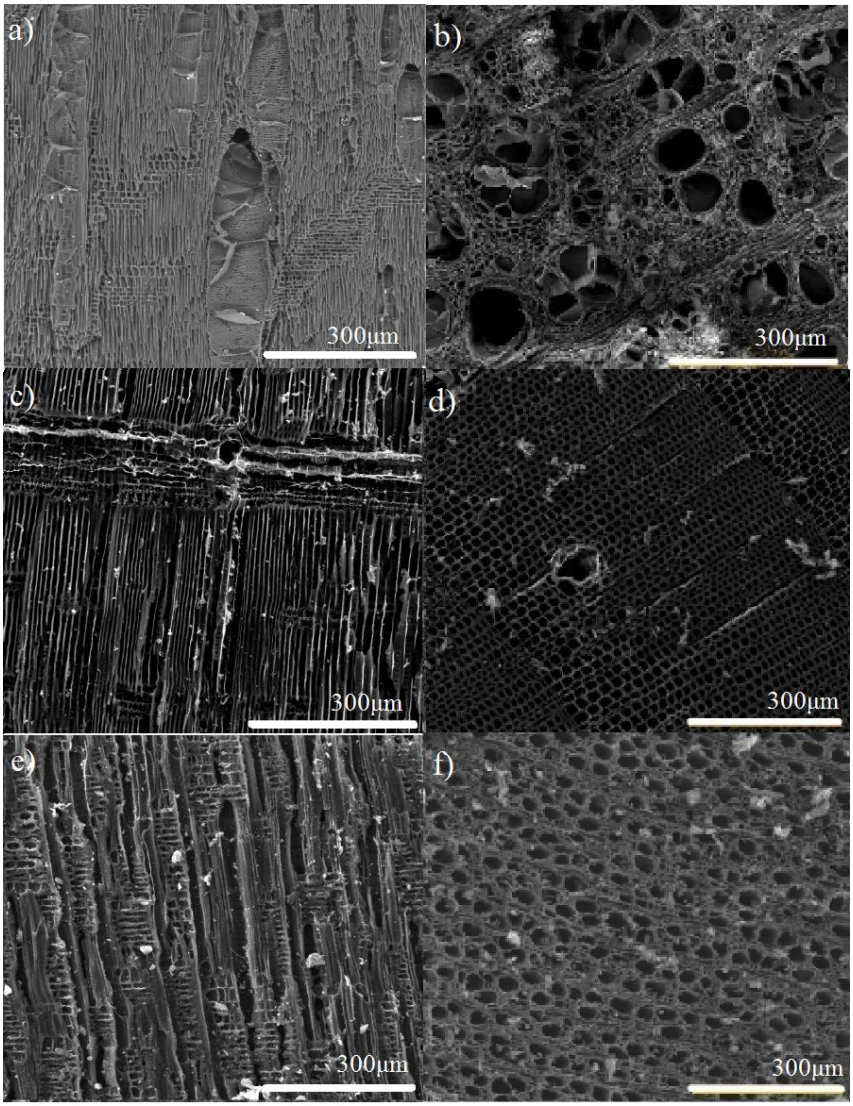

Figure 4.1. SEM images for a) beech wood in radial direction, b) beech wood in axial direction, c) pine wood in radial direction, d) pine wood in axial direction, e) sandalwood in radial direction, f) sandalwood in axial direction. Images show the woods' interconnected channels were preserved during carbonization.

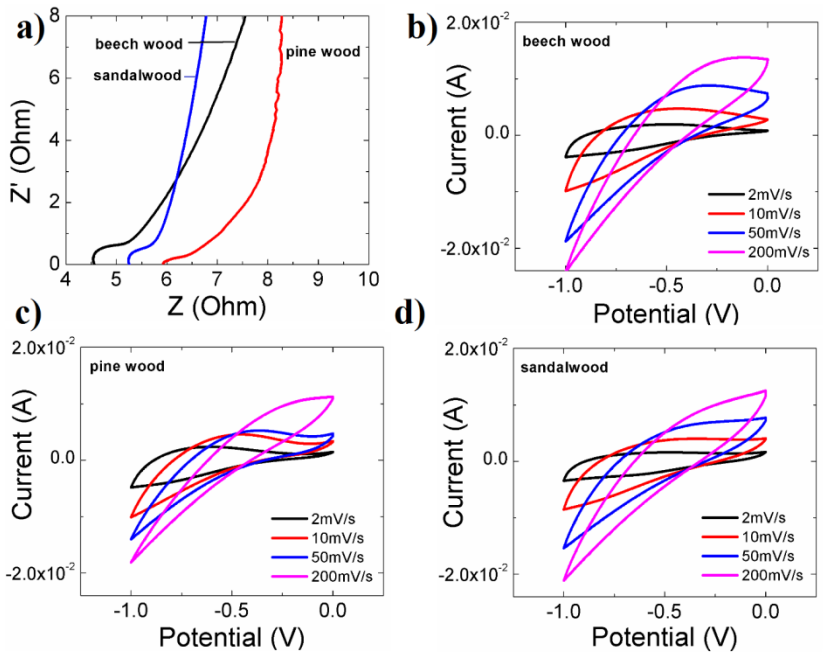

Figure 4.2. Electrochemical measurements in a) Nyquist plots for the beech, pine, and sandalwood from EIS measurements taken from 200 kHz to 0.1 Hz. CV spectra for b) beech, c) pine, and d) sandalwood at various scan rates.

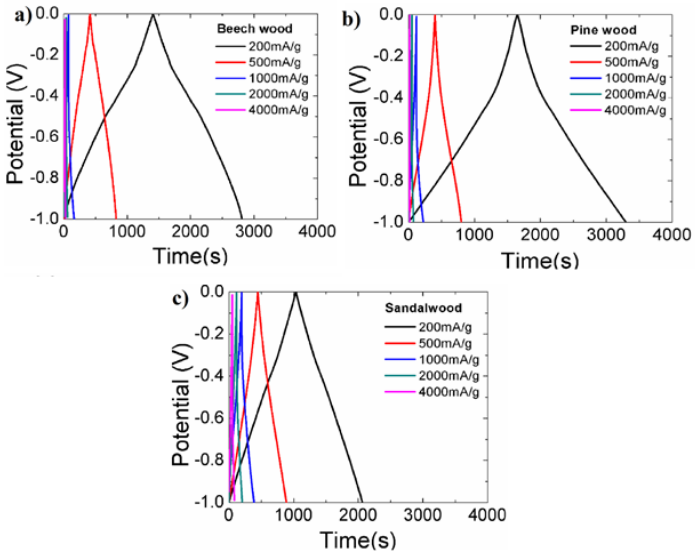

Figure 4.3. Galvanostatic charge-discharge plots at various current densities for a) beech, b) pine, and c) sandalwood electrodes.

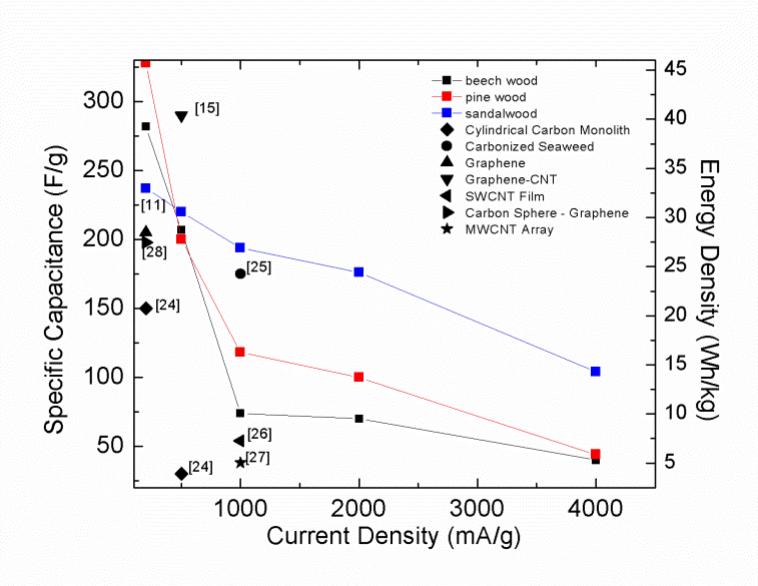

Figure 4.4. Current density (mA/g) vs. specific capacitance (F/g, left) and energy density (Wh/kg, right) for the wood electrodes. Also included are data points from the literature of other carbon-based electrodes.

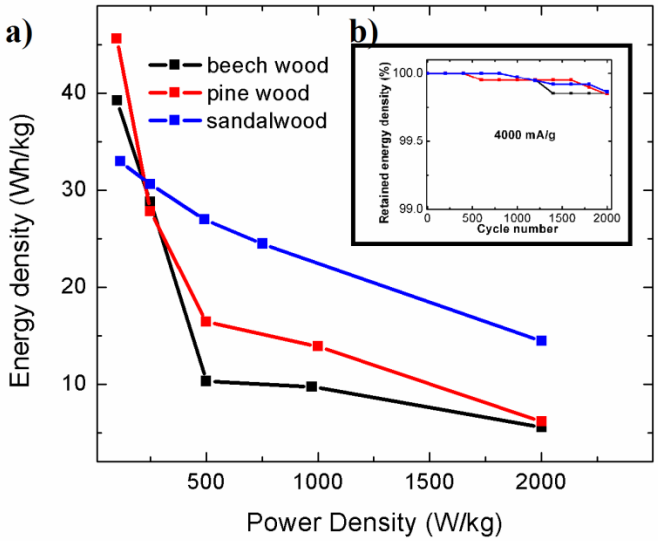

Figure 4.5. Performance measurements in a) Ragone plots of energy density vs. power density for the three types of wood electrodes. b) Cycle lifetime measurements of the three types of wood electrodes. Galvanostatic charge-discharge cycles were conducted at 4000 mA/g for each of the samples. Samples showed 99.7% capacitance retention after 2000 cycles.

Table 4.1 Specific surface areas calculated from N_2 adsorption/desorption

Samples	BET specific surface area (m^2/g)
Beech wood	44
Pine wood	76
Sandalwood	38

CHAPTER 5

Cu COMPOSITE ELECTRODES FOR PSEUDOCAPACITORS [4]

5.1 Abstract

Copper nanoparticle-loaded carbonized wood electrodes were synthesized and characterized for use as supercapacitor electrodes. The electrodes were fabricated by carbonizing $Cu(NO_3)_2$-soaked wood samples at 800°C under an N_2 atmosphere. Final copper nanoparticle content was controlled by varying the concentration of the $Cu(NO_3)_2$ solution. Subsequent X-ray diffraction and scanning electron microscopy measurements confirmed that cubic copper was formed and that the copper nanoparticles were anchored uniformly both on the surface as well as deep within the pores of the wood electrode. Cyclic voltammetry measurements showed that all of the electrodes have typical pseudo-capacitive behavior, as indicated by the presence of redox reaction peaks. Charge-discharge testing also confirmed the pseudo-capacitive nature of the electrodes. The reversible oxidation of Cu into Cu_2O and CuO was verified by performing X-ray photoelectron spectroscopy at different stages of the charge-discharge cycle.

[4] This chapter is based on the paper entitled "Cu nanoparticle loaded carbonized wood for supercapacitor electrode application," submitted to the Journal of Power Sources (2014).

5.2 Introduction

The development of renewable and sustainable energy has been of great interest because of increasing concerns regarding not only the depletion of fossil fuels, but also their potential adverse effects on the environment. However, for these technologies to be feasible, reliable energy storage devices are required. Supercapacitors are among the most promising new energy storage devices due to their high specific power densities that are comparable to secondary batteries, fast charge-discharge rates similar to those of traditional electric double-layer (EDL) capacitors, and large cyclabilities [1]. Supercapacitors have two charge storage mechanisms: nonfaradaic EDL capacitance and faradaic pseudo-capacitance. The EDL capacitance is a result of the accumulation of charge at the electrode/electrolyte interface, whereas the pseudo-capacitance arises from the relatively fast redox reactions that take place between the electroactive material within the electrode and the electrolyte.

Despite their potential, the lack of a suitable electrode material has hindered the development of supercapacitors. Current research on electrode materials for supercapacitors has been primarily on either metal oxides or conducting polymers. Although for ruthenium oxide, specific capacitances have been reported in excess of 768 F/g, its use in large-scale applications has been limited by its high cost and toxicity [2, 3]. For other, less toxic metal oxides, including NiO [4-7], CuO [8-10], and MnO_2 [11-14], their performance is only marginally better than traditional EDL capacitors [15], as they are limited by their low electrical conductivities [11, 16]. Because of their low electrical conductivities, the electrochemical performances usually suffered from the low specific capacitance at the high discharging rates and poor stability [4, 16]. As an alternative to metal oxides, conducting polymers are also commonly studied for use

in supercapacitors, including polypyrrole [17-19], polyaniline [20-23], and derivatives of polythiophene [24]. Even though these conducting polymers possess high electrical conductivities, they usually undergo structural degradation within 1,000 cycles [20, 24, 25]. Because of the shortcomings of both metal oxides and conducting polymers, alternative supercapacitor materials need to be explored.

Currently, much of the research on supercapacitor electrodes is focused on lowering the fabrication costs, increasing the energy density, and utilizing environmentally friendly materials. One such material that has potential is copper. Copper is not only one of the most abundant elements on Earth, it is also easy to recycle and is relatively inexpensive. Another very common material that has potential is carbonized wood. In a recent study, wood was found to be desirable as a supercapacitor electrode because of its unique hierarchical structure that consists of interconnected nano and micropores [26]. In this study, Cu nanoparticles were directly grown in carbonized wood samples to obtain binder-free, conducting supercapacitor electrodes. Our study has shown that the use of optimized Cu nanoparticle loading in wood supercapacitors significantly improves the electrochemical performance as compared to CuO electrodes in aqueous electrolyte.

5.3 Experimental procedure

The wood was cut to form disks approximately 20 mm in diameter and 5 mm thick. These pieces were initially boiled in a 1 M ammonia solution for 5 hours to remove the resin and any additional impurities present within the wood. The boiled samples were then transferred to a box furnace for dehydration at 120^{o}C for 3 hours. The Cu nanoparticles were deposited within the wood by placing the dehydrated wood samples

in either a 0.5 M, 1 M, or 2 M $Cu(NO_3)_2$ solution for 4 hours at 90^oC. Next, the samples were removed from the solution and allowed to dry in the air overnight. Finally, the samples were heated under N_2 at 800^oC for 2 hours, which carbonized the wood and reduced the $Cu(NO_3)_2$ into Cu nanoparticles.

X-ray diffraction experiments were carried out with a Philips X'PERT X-ray Diffractometer using Cu Kα radiation. The measurements were performed from $2\theta=10^o$ to 90^o with a step size of 0.04^o. Analysis of powder diffraction patterns was carried out using the Rietveld analysis technique. Scanning electron microscopy (SEM) measurements were carried out using an FEI Quanta 600 FEG SEM. Bulk samples were cut in half along the axis in order to examine their cross-sections. Images were taken at varying magnifications on the cut surface to verify the distribution of Cu nanoparticles in the samples. In order to characterize the redox reactions of the Cu/C electrodes, X-ray photoelectron spectroscopy (XPS) was performed using a Kratos Axis Ultra DLD with a magnesium source during different steps of discharging. The component peaks were fitted with a nonlinear, least square algorithm using Casa XPS software.

Electrochemical and capacitance measurements were performed in a three electrode system consisting of the Cu/C sample as the working electrode, platinum foil as the counter electrode, and Ag/AgCl as the reference electrode. The cyclic voltammetry (CV), galvanostatic charge-discharge, and electrochemical impedance spectroscopy (EIS) experiments were performed using a Reference 600 from Gamry Instruments. The CV response of the electrodes was measured at scan rates varying from 2 mV/s to 200 mV/s. Galvanostatic charge-discharge testing was carried out at varying potentials between 0 and -1.0 V in a 2 M KOH aqueous electrolyte solution. The EIS measurements were carried out over the frequency range from 1 MHz to 0.1 Hz.

5.4 Results and discussion

5.4.1 Characterization of the Cu/C electrodes

In order to determine the amount of Cu within each sample, the samples were cut in half and then each half was weighed (W1). One of the two halves of each sample was then placed in a tube furnace, which was heated to 800^{o}C in atmosphere for 3 hours in order to form CuO and burn off all of the carbon. The residual powder was then weighed (W2). The Cu content in the samples was determined using equation 5.1:

$$Cu\ \% = \frac{79.9 \times W2}{W1} \tag{5.1}$$

The amount of Cu embedded in the wood was determined to be 7 wt% (Cu7), 21 wt% (Cu21), and 37 wt% (Cu37) for the 0.5 M, 1 M, and 2 M $Cu(NO_3)_2$ solutions, respectively. The crystalline structure and morphology of the as-prepared Cu samples are shown in Figures 5.1 and 5.2. As seen in Figure 5.1, for all the samples, three characteristic peaks at 2θ = 43.3^{o}, 50.43^{o}, and 74.1^{o} were observed which can be indexed to match pure Cu peaks (JCPDS card No. 004-0836). No other characteristic peaks were observed, indicating that all the samples contain only pure cubic copper.

Figure 5.2 shows the SEM images of the as-prepared samples in the axial and radial directions. Figures 5.2a, b, and c are the axial surfaces of Cu7, Cu21, and Cu37 samples, respectively, which show that the Cu particles are deposited throughout the sample surface and deeply within the micropores. Figures 5.2d, e, and f show the radial surface of samples; it can be seen that the Cu nanoparticles have an average diameter of 95 nm for Cu7 sample which increases to 150 nm and 241 nm when the Cu content was

increased to 21 wt% and 37 wt%, respectively. For the Cu21 and Cu37 samples, some aggregation of the Cu nanoparticles was also observed (see Figures 5.2 b and c).

5.4.2 EIS and electrical conductivity measurements

To prove that the copper formed is actually improving the electrode properties, EIS and electrical measurements of Cu7, Cu21, and Cu37 were performed. The electrochemical impedance was measured over a frequency range from 1 MHz to 0.1 Hz at a sinusoidal potential of 5mV. Figure 5.3a shows the Nyquist plots for different electrodes. All the impedance spectra consist of a pressed semicircle at the high frequency range and a straight line in the low frequency region. An equivalent circuit used to fit the impendence curve is given in inset of Figure 5.3a, which consists of a combinational resistance (R_e) of the electrolyte interface, intrinsic resistance of the electrode, and contact resistance between the Cu nanoparticles and the carbonized wood electrode. The determined R_e values are almost the same for all the impedance spectra. The major difference of the impedance spectra is the diameter of the pressed semicircle which corresponds to the charge transfer resistance (R_{ct}) from the Faradic reactions and the double layer capacitance (C_{dl}). The straight line in low frequency region is the Warburg diffusion (Z_w) which is the ion diffusion process in the electrolyte. C_L is the limit capacitance [27]. The determined R_{ct} values for Cu7, Cu21, and Cu37 were 0.89, 0.53, and 0.46 Ohms, respectively. Another experiment performed to investigate the electrical characteristics of the electrode was the electrical resistivity measurement. Electrical resistivity was measured as a function of temperature over the range of 30 - 300 K (see Figure 5.3b). It was observed that the electrical resistivity decreased with increasing Cu content as seen in Figure 5.3b inset.

5.4.3 Cyclic voltammetry

Figure 5.4 shows the CV measurements of the electrodes for different scan rates in a 2 M KOH solution. In the polarization process with 1 mV s-1 from -1 V to 0 V for Cu7 sample (Figure 5.4a), two peaks were observed at -0.39 V and -0.11 V that were attributed to the oxidation of the Cu^0 nanoparticles to Cu^{2+}. Likewise, in the reduction process from 0 V to -1 V, two peaks were also observed at -0.42 V and -0.82 V, which are attributed to the transformation of Cu^{2+} to Cu^0 in the electrode. The pairs of redox peaks indicate that the Faradaic redox reactions of the Cu nanoparticles are reversible. It is observed that the pseudo-capacitive behavior of the Cu/C electrodes is strongly dependent on the scan rate in the CV experiments. When the scan rate increases from 1 mV/s to 10 mV/s, the oxidation peaks have a positive shift in potential, while the reduction peaks undergo a negative potential shift (indicated by the arrows), as seen in Figures 5.4 a, b, and c. This is because when the scan rate is low, the ions from the electrolyte are able to diffuse and gain access to almost all available electrode pores. This leads to a more complete insertion/extraction of the ions and an enhanced redox process.

For higher scan rates, the peak shift is due to the slow reaction rate as the electrolyte ions do not have enough time to fully react with the Cu nanoparticles. When the Cu content is increased from 7 wt% to 21 wt% and then to 37 wt%, the paired redox peaks merge into a single oxidation and a single reduction peak, as seen in Figure 5.4d. The reduction in the number of peaks with increased Cu content in the electrode can be understood by the different surface morphologies of samples. The redox reactions are mainly controlled by surface reactions of electrode. For the Cu7 sample, the reactive Cu nanoparticles are small and evenly distributed, which leads to there being more reactive

sites, thereby allowing for the completion of the redox reactions during the CV scan. In comparison, both the Cu21 and Cu37 have larger particles which clog some of the micropores, resulting in less reactive sites for the redox reactions to take place during the CV scan.

5.4.4 Galvanostatic charge-discharge

Figure 5.5 shows the charge-discharge curves of Cu7, Cu21, and Cu37 electrodes at different current densities. It is clear that the duration of the discharge decreases rapidly with increasing current density. In both the charging and discharging curves, there are two clear changes in the slope of the potential, indicating the generation of charge via the reaction of electrolyte ions with Cu nanoparticles. It can also be seen that this change in slope occurs very consistently at A1, A2, A3, and A4 for each of the electrode samples at every discharge current density tested. The deviation of these charge-discharge curves from a straight line accompanied with the nonrectangle CV curves (Figure 5.4) gives strong evidence that the Cu/C electrode behavior is pseudo-capacitive.

5.4.5 XPS analysis

The redox reactions of the Cu nanoparticles in KOH are expected to involve transitions between the Cu^0, Cu^{1+}, and Cu^{2+} species according to the following reactions:

$$2CuO + H_2O + e^- \xrightarrow[Charge]{} Cu_2O + 2OH^- \quad (5.2)$$

$$Cu_2O + H_2O + e^- \xrightarrow[Charge]{} 2Cu + 2OH^- \quad (5.3)$$

The first peak (A3) which appears during the charging process, as seen in Figure 5.5, can be attributed to the reduction of CuO to Cu_2O (Equation (5.2)). The second peak (A4) is indicative of the further reduction of Cu_2O to Cu (Equation. (5.3)). The potential peaks of A1 and A2 can be ascribed to the reverse, i.e., oxidation reactions, of A4 and A3, respectively.

These predicted redox reactions were further proved by performing XPS measurements to investigate the surface electronic states of the Cu/C electrodes. Two samples, S1 and S2, were created from a sample of Cu7 by performing a partial charge-discharge cycle at 200 mA/g, as shown in Figure 5.6a. The discharging was stopped during the first cycle, when Cu_2O (S1) and CuO (S2) were expected to have been formed. The XPS spectrum for S1 is shown in Figure 5.6b. The formation of Cu^{1+} was identified by the spectral lines Cu $2p_{1/2}$ and $2p_{3/2}$ with binding energies of 952.5 eV and 932.7 eV, which are characteristic of Cu^{1+}. Unfortunately, it is difficult to distinguish between the Cu^0 and Cu^{1+} from XPS alone, due to their nearly identical binding energies (the ~0.3 eV difference is below the resolution of the tool) [28]. However, with the evidence of the sudden change in potential at -0.5 V (Figure 5.5) alongside the XPS data (Figure 5.6), it can be concluded that Cu^{1+} was formed from the oxidation of Cu^0 to Cu_2O. The XPS data for S2 are presented in Figure 5.6c. The Cu $2p_{1/2}$ and $2p_{3/2}$ peaks were found at 955.5 eV and 935.7 eV, respectively, which indicates the formation of CuO. Peaks signifying the presence of $Cu^{1+/0}$ are also present, which are ~3 eV lower than the Cu^{2+}, suggesting that at least some of the sample had not fully oxidized into

Cu^{2+}. This result indicates that the oxidation process from -1 V to 0 V transformed some of the Cu^0 into CuO. It is likely that only the very topmost surface layer of the Cu nanoparticles was oxidized into CuO, leaving the core Cu unoxidized.

5.4.6 Specific capacitance, energy density, and power density

The specific capacitance of the systems was calculated using the following equation

$$C_s = \frac{I}{\frac{\Delta V}{\Delta t} m} \tag{5.4}$$

where I is the constant discharge current, Δt is the discharge time, m is the mass of the composite, and ΔV is the potential drop during discharge. The specific capacitance values of the Cu/C electrodes are plotted as a function of discharge current density in Figure 5.7. In addition to the obtained experimental results, reported values for few common electrodes are also listed [2, 5, 14, 29-34]. The Cu7 sample shows higher specific capacitance than the Cu21 and Cu37 at all current densities. The specific capacitance decreases rapidly with increasing discharge current densities in all samples. This can be explained as the diffusion of electrolyte ions into the pores of Cu/C electrodes decreases with increasing current density, and is limited to the outer surface of the electrode when the discharge current is relatively high. At low current densities, all of the reactive sites of the Cu nanoparticles can be fully accessed by the electrolyte ions and contribute to achieve high specific capacitance. The specific capacitance at 1000 mA/g for the Cu7 is 465 F/g, which is better than every CuO nanoparticle embedded on the current collector in aqueous KOH electrolyte reported in the literature

[31-34]. In addition, the calculated specific capacitance for Cu7 is 888 F/g at 200 mA/g. The enhanced performance of Cu7 as compared to other samples can be explained by the uniform distribution of small Cu nanoparticles. The nanoparticles serve as effective reactive sites and, when the Cu content in the electrode is increased from 7% to 21% and then to 37%, the size of Cu nanoparticles increases and can clog some micropores, thereby reducing the overall surface area, as seen in Figures 5.2a, b, and c. The reduced surface area, especially for Cu37, leads to a reduction of the specific capacitance at higher current densities (above 1000 mA/g). However, it is critical for supercapacitors to have large capacitance values at high discharge current densities in order to make them suitable for fast charge-discharge applications. The large capacitance of 88 F/g at the very high current density of 4000 mA/g for Cu7 shows that the novel Cu/C electrode is able to undergo rapid redox reactions at high current densities.

The energy density (E) and power density (P) of a supercapacitor determine how much and how fast its energy can be delivered. These quantities can be calculated according to the following equations:

$$E = \frac{1}{2} C V^2 \tag{5.5}$$

$$P = \frac{E}{t} \tag{5.6}$$

where E is the energy density, C is the specific capacitance, V is the potential window, P is the power density, and t is the discharge time. From Figure 5.8, the energy densities for Cu7 are always higher than the Cu21 and Cu37, even though the Cu7 has lower power density under the same conditions. For example, at the current density of 200

mA/g, the energy density of Cu7 is 123 Wh/kg, which is much higher than 45 Wh/kg and 21 Wh/kg for Cu21 and Cu37, respectively. The power density of Cu7 is 96 W/kg, which is similar to 80 W/kg and 99 W/kg for Cu21 and Cu37, respectively. These results suggest that Cu7 is, among all the samples studied, the ideal for large energy storage and fast charge-discharge applications.

5.4.7 Cycle life test

The cycle life test of Cu/C electrodes was performed by repeated charging and discharging of the supercapacitors at 1000 mA/g for 2000 cycles. The specific capacitances of the Cu21 and Cu37 decreased very fast during the first 300 cycles and slowly declined thereafter, as seen in Figure 5.9. The similar results were found for the conducting polymer/actived carbon electrodes, in which the active materials in the electrodes could be degraded during charge-discharge cycles [17, 20, 23, 35]. In contrast, the Cu7 exhibits excellent stability with only 5% specific capacitance decreased in the first 500 cycles and then the specific capacitance value remained almost constant. The excellent stability of Cu7 indicates that the Cu nanoparticles embedded in the carbonized wood can be used as a supercapacitor.

5.5 Conclusion

Three different concentrations of Cu nanoparticles were embedded in carbonized wood samples and tested for their potential as supercapacitor electrode materials. The advantages of using Cu nanoparticles, as opposed to other metal oxides for electrode materials, are that they require no extra current collector binding procedures and that Cu nanoparticles naturally fill the various multichannel micropores within the wood. Cyclic

voltammetry and galvanostatic charge-discharge measurements were employed to investigate the electrochemical behavior of the electrodes. All the samples showed redox current peaks in the CV scans and nonlinear charge-discharge curves in the galvanostatic measurements. These are both characteristic of pseudo-capacitive behavior. The high specific capacitance values of 888 and 324 F/g were achieved at a current density of 200 mA/g for Cu7 and Cu21 samples, respectively. The values of specific capacitance for Cu7 are larger than those usually reported for other metal oxide electrodes (MnO_2 and CuO), which highlights the pseudo-capacitive effect that Cu nanoparticles have on the electrode. The Cu7 also exhibits a higher energy density of 123 Wh/kg (at 200mA/g) and power density of 1761 W/kg (at 4000 mA/g) compared to those for Cu21 and Cu37 samples. It was found that having a small amount of Cu nanoparticles (7 wt%) performs the best, as these nanoparticles are evenly distributed throughout the wood microstructure and cannot clog the micropores in the wood. These results suggest that there is a threshold concentration for Cu in carbonized wood of approximately 7 wt%. The excellent performance obtained for Cu7 sample in these experiments opens the possibility to engineer supercapacitor electrodes based on metal and natural wood composites.

5.6 References

[1] Wang Y., Shi Z., Huang Y., Ma Y., Wang C., Chen M., Chen Y., Supercapacitor devices based on graphene materials, The Journal of Physical Chemistry C 2009;113:13103-13107.

[2] Zheng J. P. a. C., P. J. and Jow,T. R., Hydrous ruthenium oxide as an electrode material for electrochemical capacitors, Electrochemical Society 1995;142:2699-2703.

[3] Miller J. R., Simon P., Electrochemical Capacitors for Energy Management, Science 2008;321:651-652.

[4] Lee J. W., Ahn T., Kim J. H., Ko J. M., Kim J.-D., Nanosheets based mesoporous NiO microspherical structures via facile and template-free method for high performance supercapacitors, Electrochimica Acta 2011;56:4849-4857.

[5] Xiong S., Yuan C., Zhang X., Qian Y., Mesoporous NiO with various hierarchical nanostructures by quasi-nanotubes/nanowires/nanorods self-assembly: controllable preparation and application in supercapacitors, CrystEngComm 2011;13:626-632.

[6] Xia X., Tu J., Mai Y., Chen R., Wang X., Gu C., Zhao X., Graphene sheet/porous NiO hybrid film for supercapacitor applications, Chemistry-A European Journal 2011;17:10898-10905.

[7] Zhu J., Jiang J., Liu J., Ding R., Ding H., Feng Y., Wei G., Huang X., Direct synthesis of porous NiO nanowall arrays on conductive substrates for supercapacitor application, Journal of Solid State Chemistry 2011;184:578-583.

[8] Zhang X., Shi W., Zhu J., Kharistal D. J., Zhao W., Lalia B. S., Hng H. H., Yan Q., High-Power and High-Energy-Density Flexible Pseudocapacitor Electrodes Made from Porous CuO Nanobelts and Single-Walled Carbon Nanotubes, ACS Nano 2011;5:2013-2019.

[9] Dubal D., Dhawale D., Salunkhe R., Jamdade V., Lokhande C., Fabrication of copper oxide multilayer nanosheets for supercapacitor application, Journal of Alloys and Compounds 2010;492:26-30.

[10] Li Y., Chang S., Liu X., Huang J., Yin J., Wang G., Cao D., Nanostructured CuO directly grown on copper foam and their supercapacitance performance, Electrochimica Acta 2012.

[11] Yu G., Hu L., Liu N., Wang H., Vosgueritchian M., Yang Y., Cui Y., Bao Z., Enhancing the Supercapacitor Performance of Graphene/MnO2 Nanostructured Electrodes by Conductive Wrapping, Nano Letters 2011;11:4438-4442.

[12] Fischer A. E., Pettigrew K. A., Rolison D. R., Stroud R. M., Long J. W., Incorporation of Homogeneous, Nanoscale MnO2 within Ultraporous Carbon

Structures via Self-Limiting Electroless Deposition: Implications for Electrochemical Capacitors, Nano Letters 2007;7:281-286.

[13] Yan J., Fan Z., Wei T., Qian W., Zhang M., Wei F., Fast and reversible surface redox reaction of graphene–MnO2 composites as supercapacitor electrodes, Carbon 2010;48:3825-3833.

[14] Xia H., Feng J., Wang H., Lai M. O., Lu L., MnO2 nanotube and nanowire arrays by electrochemical deposition for supercapacitors, Journal of Power Sources 2010;195:4410-4413.

[15] Liu C., Yu Z., Neff D., Zhamu A., Jang B. Z., Graphene-Based Supercapacitor with an Ultrahigh Energy Density, Nano Letters 2010;10:4863-4868.

[16] Cao X., Shi Y., Shi W., Lu G., Huang X., Yan Q., Zhang Q., Zhang H., Preparation of Novel 3D Graphene Networks for Supercapacitor Applications, Small 2011;7:3163-3168.

[17] Zhang D., Zhang X., Chen Y., Yu P., Wang C., Ma Y., Enhanced capacitance and rate capability of graphene/polypyrrole composite as electrode material for supercapacitors, Journal of Power Sources 2011;196:5990-5996.

[18] Biswas S., Drzal L. T., Multilayered Nanoarchitecture of Graphene Nanosheets and Polypyrrole Nanowires for High Performance Supercapacitor Electrodes, Chemistry of Materials 2010;22:5667-5671.

[19] Davoglio R. A., Biaggio S. R., Bocchi N., Rocha-Filho R. C., Flexible and high surface area composites of carbon fiber, polypyrrole, and poly(DMcT) for supercapacitor electrodes, Electrochimica Acta 2013;93:93-100.

[20] Sivakkumar S. R., MacFarlane D. R., Forsyth M., Kim D.-W., Ionic Liquid-Based Rechargeable Lithium Metal-Polymer Cells Assembled with Polyaniline/Carbon Nanotube Composite Cathode, Journal of The Electrochemical Society 2007;154:A834-A838.

[21] Wang K., Meng Q., Zhang Y., Wei Z., Miao M., High-Performance Two-Ply Yarn Supercapacitors Based on Carbon Nanotubes and Polyaniline Nanowire Arrays, Advanced Materials 2013.

[22] Yan Y., Cheng Q., Zhu Z., Pavlinek V., Saha P., Li C., Controlled synthesis of hierarchical polyaniline nanowires/ordered bimodal mesoporous carbon nanocomposites with high surface area for supercapacitor electrodes, Journal of Power Sources 2013;240:544-550.

[23] Wang Q., Yan J., Fan Z., Wei T., Zhang M., Jing X., Mesoporous polyaniline film on ultra-thin graphene sheets for high performance supercapacitors, Journal of Power Sources 2014;247:197-203.

[24] Snook G. A., Kao P., Best A. S., Conducting-polymer-based supercapacitor devices and electrodes, Journal of Power Sources 2011;196:1-12.

[25] Sivakkumar S. R., Kim D.-W., Polyaniline/Carbon Nanotube Composite Cathode for Rechargeable Lithium Polymer Batteries Assembled with Gel Polymer Electrolyte, Journal of The Electrochemical Society 2007;154:A134-A139.

[26] Teng S., Siegel G., Wang W., Tiwari A., Carbonized Wood for Supercapacitor Electrodes, Solid State Letters 2014;3:M25-M28.

[27] Fan Z., Yan J., Wei T., Zhi L., Ning G., Li T., Wei F., Asymmetric supercapacitors based on graphene/MnO2 and activated carbon nanofiber electrodes with high power and energy density, Advanced Functional Materials 2011;21:2366-2375.

[28] Li Q., Li K., Sun C., Li Y., An investigation of Cu2+ and Fe2+ ions as active materials for electrochemical redox supercapacitors, Journal of Electroanalytical Chemistry 2007;611:43-50.

[29] Wang H.-W., Hu Z.-A., Chang Y.-Q., Chen Y.-L., Lei Z.-Q., Zhang Z.-Y., Yang Y.-Y., Facile solvothermal synthesis of a graphene nanosheet–bismuth oxide composite and its electrochemical characteristics, Electrochimica Acta 2010;55:8974-8980.

[30] Purushothaman K. K., Manohara Babu I., Sethuraman B., Muralidharan G., Nanosheet-Assembled NiO Microstructures for High-Performance Supercapacitors, ACS applied materials & interfaces 2013;5:10767-10773.

[31] Yu L., Jin Y., Li L., Ma J., Wang G., Geng B., Zhang X., 3D porous gear-like copper oxide and their high electrochemical performance as supercapacitors, CrystEngComm 2013;15:7657-7662.

[32] Huang J., Wu H., Cao D., Wang G., Influence of Ag doped CuO nanosheet arrays on electrochemical behaviors for supercapacitors, Electrochimica Acta 2012;75:208-212.

[33] Liu Y., Huang H., Peng X., Highly enhanced capacitance of CuO nanosheets by formation of CuO/SWCNT networks through electrostatic interaction, Electrochimica Acta 2013;104:289-294.

[34] Kim D.-W., Rhee K.-Y., Park S.-J., Synthesis of activated carbon nanotube/copper oxide composites and their electrochemical performance, Journal of Alloys and Compounds 2012;530:6-10.

[35] Laforgue A., Simon P., Fauvarque J., Mastragostino M., Soavi F., Sarrau J., Lailler P., Conte M., Rossi E., Saguatti S., Activated carbon/conducting polymer hybrid supercapacitors, Journal of the Electrochemical Society 2003;150:A645-A651.

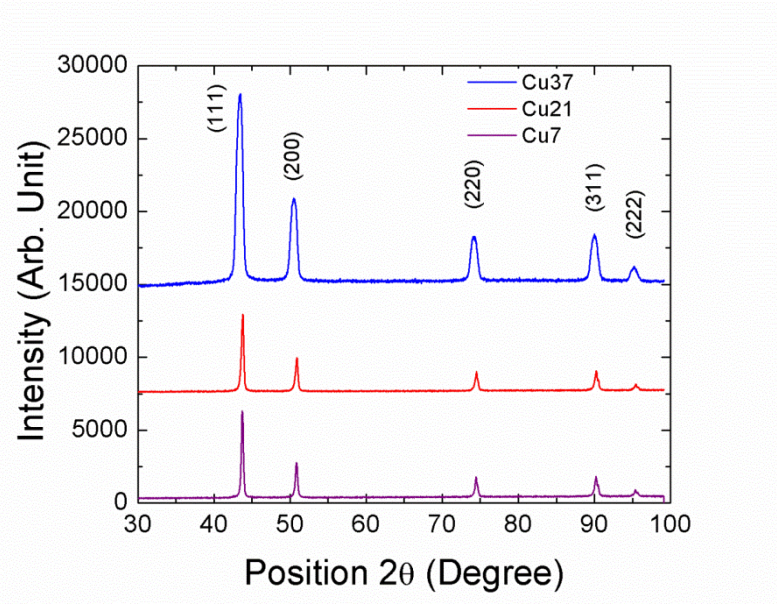

Figure 5.1. XRD spectra of Cu nanoparticle embedded carbonized wood electrodes.

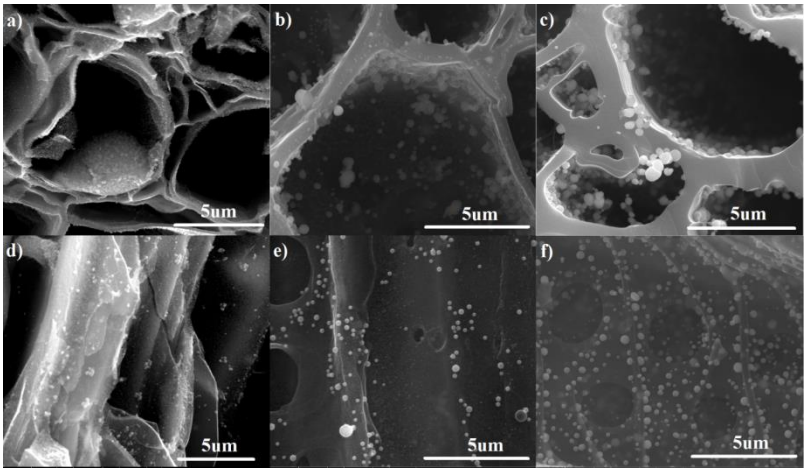

Figure 5.2. Axial SEM images for a) Cu7 sample, b) Cu21 sample, c) Cu37 sample, radial SEM images for d) Cu7 sample, e) Cu21 sample, f) Cu37 sample.

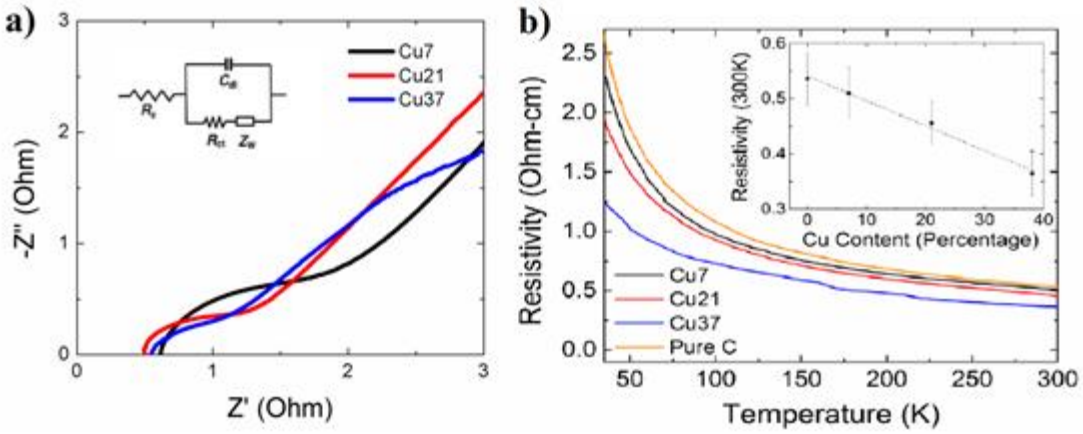

Figure 5.3. Electrical measurements in a) Nyquist plots for the various samples from 200 kHz to 0.1 Hz, inset is the electrical equivalent circuit used for fitting impedance spectra b) relationship between resistivity and temperature for samples.

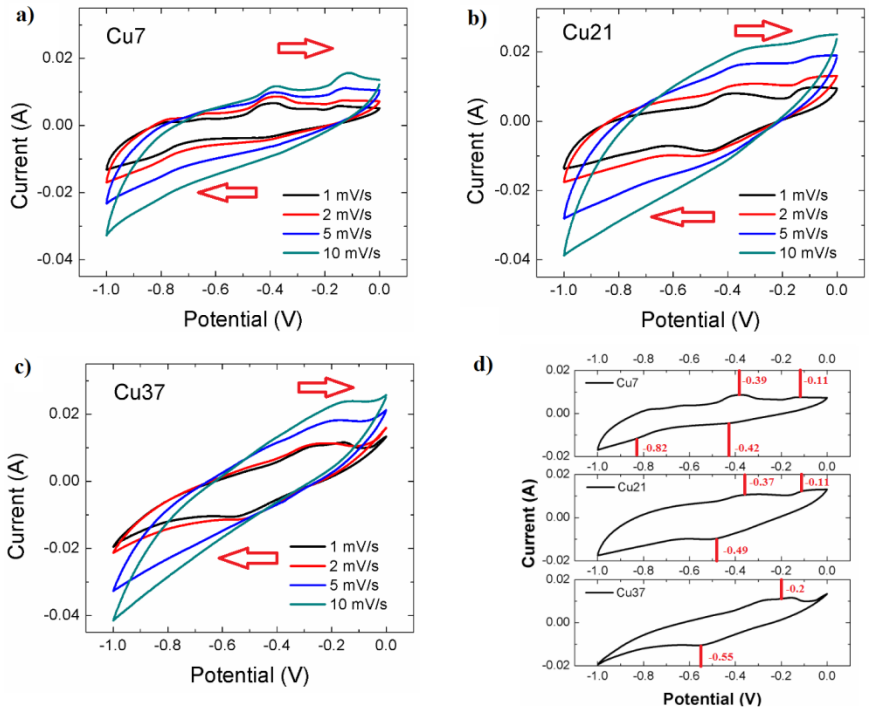

Figure 5.4. CV spectra for: a) Cu7 sample, b) Cu21 sample, c) Cu37 sample at various scan rates, d) current peaks for different samples at 1mV/s.

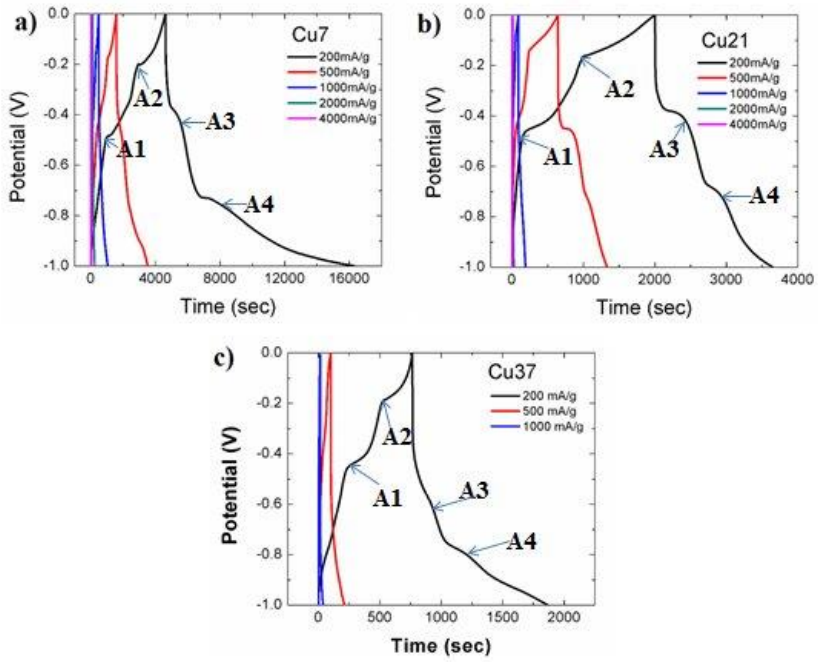

Figure 5.5. Charge-discharge plots at various current densities for: a) Cu7 sample, b) Cu21 sample, c) Cu37 sample.

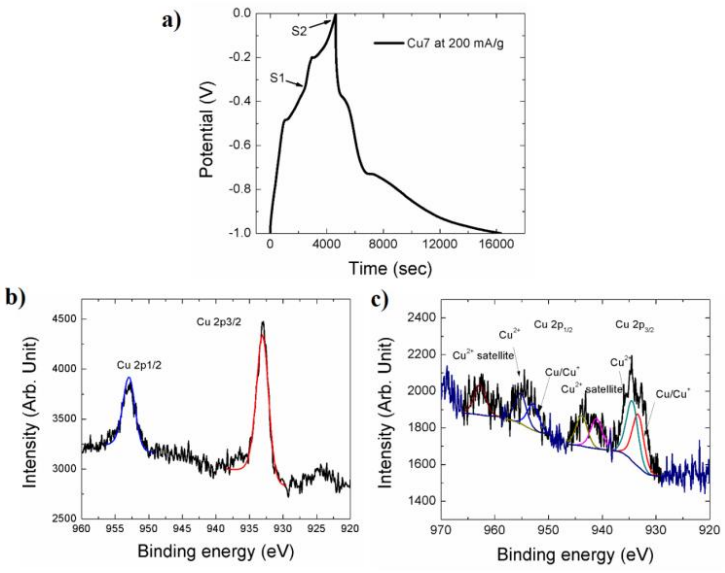

Figure 5.6. XPS samples from a) S1 and S2; XPS data for b) S1 sample c) S2 sample.

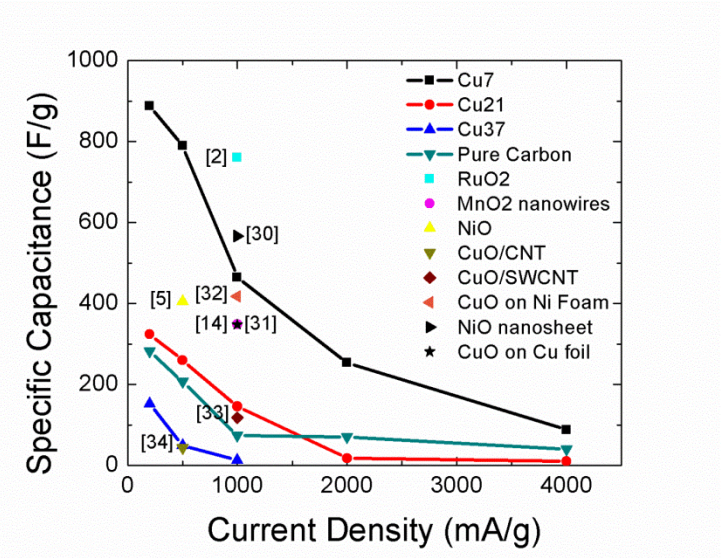

Figure 5.7. Relationships between the specific capacitance and energy density with current density for various electrodes.

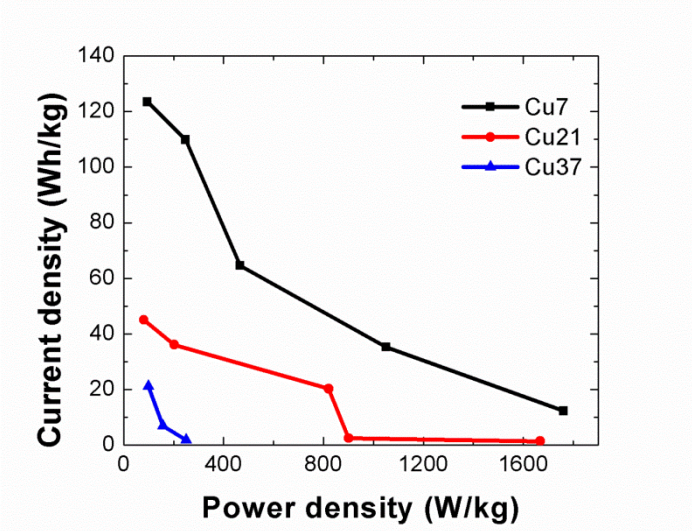

Figure 5.8. Relationships between the power and energy density with current density for various electrodes.

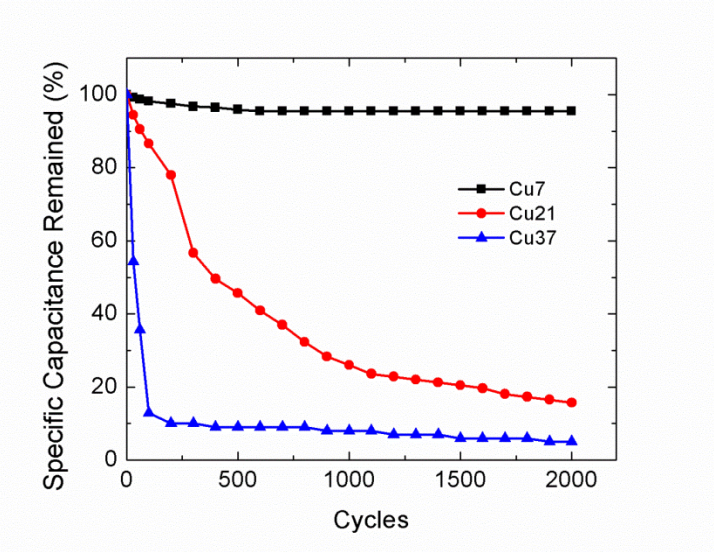

Figure 5.9. Cycle performance of samples under a current density of 1000 mA/g.

CHAPTER 6

CONCLUSION AND FUTURE RESEARCH

In this chapter, the unsolved problems reported in the previous chapters are summarized and analyzed. Suggestions on how to solve these problems are made. Recommendations on how to further improve the performance of solid state Li ion batteries and supercapacitors are detailed.

6.1 Laser annealing of LLZO

Current synthesis of cubic LLZO always requires sinterring at very high temperatures (above 1200^{o}C) for a long period of time (more than 36 hours). The high processing temperature and long processing time cause lithium deficiencies and also limits its applications. Much research has been done on doping LLZO with extrinsic dopants such as Al or Ga to lower the sintering temperature required to achieve cubic phase. However, it has also been reported that a secondary phase was precipitated at grain boundaries which can hinder the ion transport in the material. In the present study, we have used a pulsed laser annealing process to convert tetragonal LLZO to cubic LLZO at room temperature without any extrinsic dopants. The room temperature ionic conductivity for the laser annealed cubic LLZO yields a three orders of magnitude improvement over the tetragonal LLZO. However, future work is required to

determine the exact threshold energy required for the phase transformation from the tetragonal to cubic LLZO, as well as the effect of laser annealing on garnet phase stability.

6.2 Low temperature molten salt synthesis of LLNO

Cubic LLNO solid state electrolyte was successfully synthesized at 900^{o}C. In order for the garnet cubic LLNO to obtain high ionic conductivity, further sintering is required to cause grain growth. The Li ion conductivity was found to increase with increasing sintering. A high ionic conductivity of $2.5x10^{-5}$ S/cm was achieved, which is similar to the highest value previously reported for LLNO electrolytes.

The kinetic of using molten salt synthesis method was originated from the 705^{o}C eutectic temperature of Li_2O and Li_2CO_3. Future work should focus on using LiOH and Li_2CO_3 mixture to further reduce the cubic LLNO synthesis temperature, ae LiOH has an even lower melting temperature of only 450^{o}C.

6.3 Wood electrodes for supercapacitors

Carbonized woods with different pore size distributions were used as electrode materials for supercapacitors. These supercapacitors made from wood electrodes have been shown to have a high specific capacitance, high energy density, ideal capacitor behavior, and excellent electrochemical stability. This study has outlined a general and rational strategy to fabricate open up new paths.

The study also presents a substantial progress towards producing high performance supercapacitor by utilizing hierarchically structured electrodes. Future work on the basis of the synthesis of carbonized wood should open the possibility for continuous research

on hierarchical electrodes. These advances may extend the frontier of supercapacitor research and wood electrodes.

6.4 Cu composite electrodes for pseudo-supercapacitors

Cu nanoparticles were embedded in carbonized wood samples and tested for their potential as supercapacitor electrode materials. The advantages of using Cu nanoparticles, as opposed to other metal oxides for electrode materials, are that they require no extra current collector binding procedures. It has been proven that composite electrodes with a proper amount of Cu significantly improve the specific capacitance by a factor of three. Future research on pseudo-supercapacitors should be directed towards the development of nanomaterials with high specific surface area, high charge capacity, and minimum ESR. In addition, one-step synthesis without an additional activation process to obtain high density composite materials would be beneficial for the compact design of high power energy sources.

This dissertation examined some very attractive materials for energy storage devices, namely Li ion batteries and supercapacitors. For the Li ion battery research, the novel laser annealing method and molten salt synthesis methods have been employed to successfully fabricate high quality garnet cubic solid state electrolytes. For the supercapacitor research, Copper wood nanocomposite electrodes with high surface area, interconnected pores, and high electrical conductivity have been shown to improve energy density of supercapacitors without sacrificing the high rate capacity and long cycle life.